Experiments and Numerical Simulations of the Flow Within a Model of a Hydraulic Turbine Surge Chamber

Alexandre Massé

Department of Mechanical Engineering

McGill University, Montreal

A thesis submitted to McGill University in partial fulfilment of

the requirements of the degree of

Master of Engineering

Abstract

Surge chambers are sometimes included in the hydraulic circuits of hydroelectric power plants as a means of absorbing pressure waves formed by the opening/closing of a turbine. Surge chambers, however, result in additional power loss and therefore reduce the efficiency of the plant. This work aims to 1) investigate the physical phenomena and flow within a surge chamber under normal operation (*i.e.* no opening/closing of a turbine), and 2) obtain experimental data for the validation of numerical simulations of this complex flow.

Experiments and numerical simulations have been conducted for a simplified model of a surge chamber operated under multiple configurations at a constant input flow rate. This 3-D, unsteady, incompressible, swirling, two-phase flow has been experimentally characterized by global values, such as head losses, and local values, such as free-surface profiles, free-surface oscillations, reduced pressure profiles and velocity fields. The same quantities were also obtained numerically using the "rasInterFoam" solver of the open source code "OpenFOAM-1.5," for incompressible two-phase flows. This solver implements a one-fluid, volume-of-fluid (VOF) method with an interface-capturing scheme.

Overall agreement between the experimental and numerical quantities is good, although there are local discrepancies. The periodic oscillations of the flow observed in the experiments and the numerical simulations of the simplified model (operated under constant input flow rate) were associated with the phenomena of i) oscillating mass, and ii) self-induced sloshing.

Résumé

Des chambres d'équilibre sont parfois intégrées aux circuits hydrauliques des centrales hydroélectriques afin d'absorber les ondes de pression se formant lors de l'ouverture/fermeture d'une turbine. Celles-ci affectent l'efficacité des centrales, en augmentant les pertes d'énergie. Ce projet de maîtrise vise à 1) étudier les phénomènes physiques ainsi que l'écoulement à l'intérieur d'une chambre d'équilibre sous opération normale (*i.e.* aucune ouverture/fermeture de turbine), et à 2) obtenir des données expérimentales visant à valider les simulations numériques de cet écoulement complexe.

Les mesures expérimentales et les simulations numériques ont été effectuées sur un modèle simplifié d'une chambre d'équilibre. Ce dernier a été opéré sous de multiples configurations à débit d'entrée constant. L'écoulement tridimensionnel, instationnaire, incompressible, tourbillonnant et biphasique a été caractérisé expérimentalement par des quantités globales, telles que des pertes de charges, ainsi que par des quantités locales, telles que des profils et des périodes d'oscillations de surface libre, des profils de pression réduite et des champs de vitesses. Les mêmes quantités ont aussi été obtenues par calculs numériques en utilisant l'exécutable "rasInterFoam" du code à source ouverte "OpenFOAM-1.5", limité aux écoulements incompressibles et biphasiques. Ce dernier traite l'écoulement comme étant un mélange localement homogène composé de deux phases en utilisant une méthode "volume-of-fluid" (VOF) et un schéma de capture d'interface.

Globalement, les résultats numériques concordent avec les mesures expérimentales, malgré quelques variations locales. Les oscillations périodiques de l'écoulement survenant à un débit d'entrée constant, qui ont été observées tant sur le banc d'essai que dans les simulations numériques, sont associées aux phénomènes i) d'oscillation de masse et de ii) ballottement auto-induit.

Acknowledgments

I would like to express my sincere gratitude to my supervisor, Professor Laurent Mydlarski, for his continuous support and guidance, and especially for his important contribution in the redaction of this thesis. I also wish to acknowledge my co-supervisor, Dr. Maryse Page, for our fruitful discussions, her valuable comments and special help with the OpenFOAM code.

I am also in debt to NSERC for their financial support and to the two industrial partners involved in the project: Hydro-Québec for having proposed and funded the project, and Groupe Conseil LaSalle for having shared their experimental facilities. Numerous people in industry have contributed to the success of this project. However, a special mention must be given to Anne-Marie Giroux and Jean-Philippe Saucet, who together made this study possible.

Finally, I am thankful to my love Myriam, who is always my greatest source of encouragement.

Table of Contents

List of Figures

List of Tables

1. Introduction

1.1. Background and Motivation

Surge chambers are sometimes included in the hydraulic circuits of hydroelectric power plants as a means of absorbing pressure waves formed during the opening/closing of a turbine. Hydraulic turbine surge chambers reduce undesirable "water hammer" effects, but at the price of adding extra power losses under normal operation (no opening/closing).

A recent study of the surge chamber of the Robert-Bourassa hydroelectric power plant (Québec's largest hydroelectric power plant) was conducted at the "Institut de recherche d'Hydro-Québec" (IREQ) (Houde 2007). Its objectives were to establish a guide for the plant operators to assist them in their choice of which turbine to shutdown or turn on to minimize the losses in the surge chamber. Leading to satisfactory practical engineering results, this study also raised numerous questions, notably on observed unsteady phenomena, the correct way to evaluate the global power losses, and the use of the open source code "OpenFOAM" in simulating such a flow. The current project aims to address those questions by experimental measurements on a simplified model of a surge chamber and by numerical simulations using the "rasInterFoam" solver of OpenFOAM-1.5.

Despite the simple geometry of the model test bed under study (two circular input pipes connected to a rectangular tank with one circular output pipe aligned with one of the inputs, see Figure 3.1), this 3D, unsteady, incompressible, swirling, two-phase flow is rich in interesting physical phenomena worthy of study. The nature of the flow also presents important numerical challenges (detached two-phase flow with regions of air entrainment into water), resulting in a good test case for OpenFOAM, which is always in need of further validation with experimental measurements for its diffusion within the CFD community.

The remainder of the chapter is structured as follows: Section 1.2 states the objectives of this project. Then, Section 1.3 reviews the literature pertaining to the numerical methods used in solving two-phase flows. Finally, Section 1.4 outlines the content of Chapters 2 to 6.

1.2. Objectives

The objectives of this research can be grouped into two principal categories:

1- *Understanding and characterizing the unsteady phenomena occurring in the simplified model of a surge chamber under normal operation (no opening/closing).*

   Some unsteady behaviours of the flow in the simplified model of a surge chamber, when the latter was operated under constant input flow rate, were observed in the previous study conducted at IREQ (Houde 2007; Houde *et al.* 2007). In this study, it was noted that i) for the case of the *offset pipe* under operation, the head losses oscillated periodically in the numerical simulations, and that ii) for the case of the *aligned input pipe* under operation, the free-surface in both the experiments and the numerical simulations exhibited sustained oscillations in its 1st sloshing mode. Although the free-surface oscillations were associated with the phenomenon of "self-induced sloshing," the origin(s) of other unsteadinesses in the flow of the simplified model of a surge chamber remained unclear. This project will pursue the analysis further, trying to characterize the different unsteady phenomena in the flow, and to more thoroughly understand their origin(s).

2- *Validating the use of the rasInterFoam solver of OpenFOAM-1.5 to numerically simulate the flow in hydraulic turbine surge chambers.*

   The simplified model of a hydraulic turbine surge chamber was designed to provide a type of flow similar to ones inside actual surge chambers. The validation of the rasInterFoam solver in simulating such a flow was done on this simplified model. In this project, the principal flow structures will be identified, using both local and global quantities for their characterizations. Experiments will be performed on the test bed to measure the quantities and to provide benchmark data for the simulations. Numerical simulations will be run to estimate the level of confidence in the rasInterFoam solver, keeping in mind that both CFD simulations and experimental measurements have their own limitations.

1.3. Literature Review

1.3.1. Numerical Methodologies for Two-Phase Flows

A variety of two-phase flow problems lead to many different numerical models, each of them attempting to accurately simulate the underlying physical phenomena. To classify the different numerical models for two-phase flows, it is convenient to distinguish the two phases of the flow as one "particle phase" and one "continuous phase." The former is the dispersed phase that may consist of bubbles, particles, or droplets, while the latter is the fluid surrounding the particle phase.

The continuous phase is often solved in an Eulerian reference frame. Two-phase flow numerical methods can then be classified by the procedure employed to solve the particle phase. The particle phase solution procedure can be subdivided according to two classifications. The first classification relates to the reference frame used for the particle phase representation, either Lagrangian or Eulerian. The second classification relates to the treatment of the surface forces on the particle phase. Surface forces can be treated as "point-force" or "resolved-surface." The two classifications yield four categories for the particle phase approach: "Lagrangian frame with point-force treatment," "Lagrangian frame with resolved-surface treatment," "Eulerian frame with mixed-fluid treatment," and "Eulerian frame with point-force treatment" (Crowe *et al.* 2006; Prosperetti *et al.* 2007). A brief description of the above four categories follows.

Lagrangian Approaches: Point-Force and Resolved-Surface

Methods employing a Lagrangian frame of reference for the particle phase are referred to as Euler-Lagrange methods when the continuous phase is solved on an Eulerian grid. In these methods, every particle is tracked in the flow domain by solving the momentum equation expressed in the Lagrangian formulation:

$$m_{particle}\frac{d\vec{V}_{particle}}{dt} = \vec{F}_{body} + \vec{F}_{surf} + \vec{F}_{coll}. \qquad \text{[Eqn. 1.1]}$$

In Eqn. 1.1, the LHS is the particle mass multiplied by its acceleration while the RHS represents the body forces (gravity), the fluid dynamic surface forces acting on the particle, and the particle-particle or particle-wall collision forces.

The principal difference between point-force and resolved-surface methods is how the surface forces are calculated. In point-force methods (Figure 1.1a), surface forces such as lift, drag, added-mass and stress gradients are found from empirical and theoretical treatment of the particle/continuous phase relative velocity. The key assumption in these methods is to consider the surrounding phase as a hypothetical continuous flow having properties defined at the particles' centroids. As the flow becomes more dense in particles, this assumption fails. In resolved-surface methods (Figure 1.1b), surface forces are obtained by integrating the fully resolved continuous phase pressure and shear stresses over the particle surface. This will result in more realistic surface forces, but at

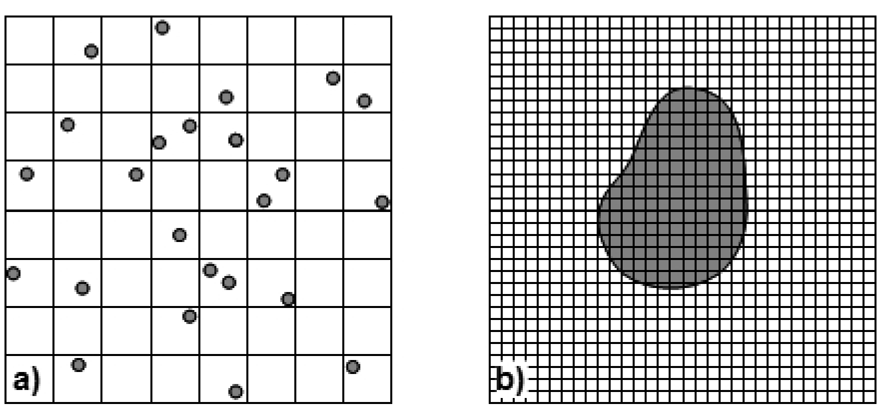

***Figure 1.1**: Representation of (a) point-force and (b) resolved-surface treatment for Euler-Lagrange methods.*

the price of a high grid resolution over the particle. This method is thus restricted for few particles in the flow domain. On the other hand, point-force methods must have grid cells that are larger than the particles.

Eulerian Approaches

Methods employing an Eulerian frame of reference for the particle phase are separated into the mixed-fluid ("one-fluid") and the point-force ("two-fluid") approaches. The key assumption for these approaches is to treat the particle phase as a continuum. The particle phase continuum assumption (Drew *et al.* 1998) requires a large amount of particles in each cell, and a cell length much larger than the average particle spacing. This assumption imposes a limit on the grid refinement. On the other hand, solving the particle phase on an Eulerian grid allows the use of consistent numerical schemes for both phases — an advantage for their two-way coupling.

In the one-fluid approach, the two phases are assumed to be in kinetic and thermal equilibrium within each cell, *i.e.* the phases' relative velocities and temperatures are assumed to be small compared to the variations occuring in the fluid domain. The two phases are treated as a homogenous mixture within each cell. Fluid properties change from cell to cell depending on the phase concentration, and only one set of momentum equations needs to be solved for the entire flow domain. This approach is the one used in this project and will be further discussed in Chapter 4.

In two-fluid approaches, the two phases are treated as two separate continua, interpenetrating each other with each continuum having its own set of momentum equations. Extra terms in the momentum equations account for the momentum transfer between the two phases. In contrast to the one-fluid approach, the relative phase velocities and temperatures are required, as they are used to determine the coupling forces between each phase using a point-force approach.

1.3.2. Numerical Methodologies for Resolving the Interface

The preceding section was a review of the numerical methods for solving two-phase flows. The current section presents some of the existing methodologies for resolving the interface separating two immiscible fluids. Free-surface numerical methodologies can fall into two categories: surface methods or volume methods (Gopala *et al.* 2008).

Surface Methods

In surface methods, the interface is marked or tracked explicitly. For moving grids (Figure 1.2a), some nodes are associated with the interface and move with it. For fixed grids, the interface can be tracked on an Eulerian grid by a set of interconnected massless particles advected by the local velocity in a Lagrangian manner. This method is referred to as the front-tracking method (Figure 1.2b) (Unverdi *et al.* 1992). Alternatively, the interface can be tracked by the level set method in which a zero level set is associated with the interface. A distance function from the interface is advected with the local fluid velocity defining a new interface (Osher *et al.* 1988). Surface methods have the advantage of maintaining the exact position of the interface, but require special treatment for its breakup and coalescence.

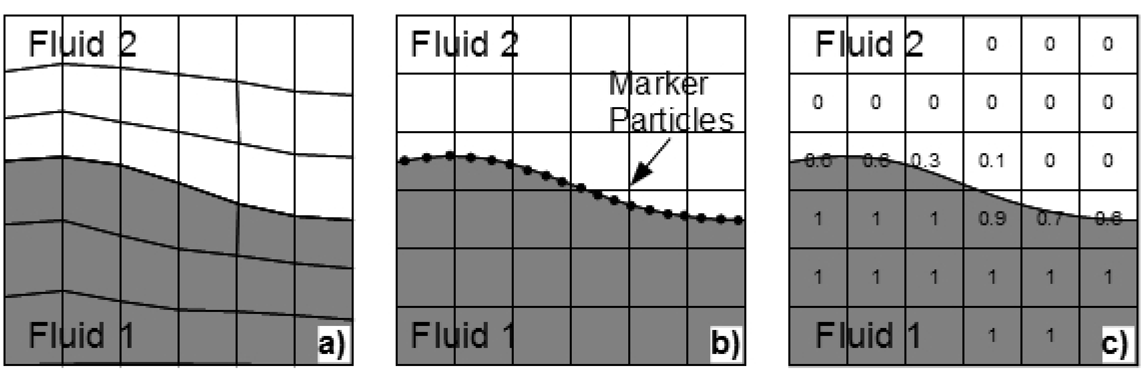

Figure 1.2: *Free-surface methodologies: (a) moving grid, (b) front-tracking method and (c) volume of fluid method.*

Volume Methods

In volume methods, the two phases are marked by massless particles or by an indicator function. The exact position of the interface is not known explicitly but must be reconstructed from the markers. Among many methods, the marker and cell (MAC) method of Harlow *et al.* (1965) uses massless particles advected in a Lagrangian manner to identify each phase. The interface is reconstructed by the density of the marker particles in each cell.

The volume of fluid (VOF) method (Figure 1.2c), another volume method, uses a phase volume fraction between 0 and 1 to distinguish between the two different fluids. The volume fraction is a scalar that is advected by the flow and is used to determine the location of the interface. The introduction of the volume fraction field results in the need for an extra transport (advection-only) equation to be solved. A major challenge in VOF methods is to advect the interface without diffusing, dispersing, or wrinkling it. Many advection schemes have been developed over the years. They can be divided into two categories: "interface-reconstruction" and "interface-capturing" (Darwish 2006). In interface-reconstruction schemes, the interface is explicitly reconstructed at each time step and volume fraction fluxes computed from the reconstructed interface. Examples of those schemes are the Simple Line Interface Calculation (SLIC) (Noh *et al.* 1976) and the Piecewise-Linear Interface Calculation (PLIC). In the interface-capturing technique, volume fraction fluxes are computed without reconstruction of the interface. A compressive scheme is often used to sharpen the interface. Examples of those schemes include Total Variation Diminishing (TVD) methods, Flux Corrected Transport (FCT) schemes and techniques using the Normalized Variable Diagram (NVD) (Leonard 1991).

In this study, the "rasInterFoam" solver of OpenFOAM-1.5 was employed. The algorithm implemented in this code is a one-fluid, VOF method with an interface-capturing scheme. The description of the algorithm is presented in Chapter 4.

1.4. Thesis Outline

The remainder of the thesis is organized as follows. In Chapter 2, the major flow structures are first presented to introduce the reader to the problem and its complexities. Then, two unsteady phenomena associated with the flow in the surge chamber model are described: i) the oscillating mass, and ii) the self-induced sloshing phenomena. The chapter ends with a discussion of different methods to estimate the head losses in the surge chamber.

Chapter 3 presents the experimental method used herein. The apparatus and the three different measurement devices employed on the test bed are first described. Then, the test cases under study and the measurements performed for each of them are discussed.

The numerical method employed in the rasInterFoam solver of OpenFOAM-1.5 is described in detail in Chapter 4. The description includes a brief discussion of the volume-of-fluid (VOF) method, a short derivation of the governing equations that are solved, the special solution procedure for solving the volume fraction transport equation, the implementation of the pressure-implicit split-operator (PISO) method for coupling the velocities and pressure, and a brief summary of the algorithm. Finally, the different numerical simulations that were run in this study are presented at the end of the chapter.

The results from the experiments and the numerical simulations are presented and compared in Chapter 5. The results include the dominant frequencies of the periodic oscillations of the flow, and time-averaged quantities such as the average velocities, the reduced pressure profiles at the downstream wall of the chamber, the free-surface profiles and the global head losses. The origin(s) of the unsteady behaviour of the flow is (are) investigated by using the theory of the two phenomena described in Chapter 2. Finally, a sensitivity analysis of few simulation parameters is presented, for the case of the offset pipe under operation.

Lastly, the main findings with respect to the project's objectives are summarized, and suggestions for future research are given in Chapter 6.

2. Physical Background

The flow in the simplified surge chamber model is not a commonly studied flow. Its major structures, and the phenomena underlying its periodic fluctuations, are therefore not *a priori* obvious. In the interest of appreciating the complexities of this flow and justifying the choices that were made relative to its experimental and numerical analysis, the physics behind the phenomena observed in this study are presented in the current chapter. The major flow structures are first outlined in Section 2.1, for one of the configurations of the chamber that was studied. A simplified analysis demonstrating the "oscillating mass" phenomenon is then presented in Section 2.2. Sections 2.3 and 2.4 introduce the subject of natural oscillation of the free-surface in a rectangular tank and that of "self-induced sloshing," respectively. Finally, Section 2.5 ends the chapter with a discussion on the estimation of the head losses in the surge chamber model.

2.1. Overview of Some Structures in the Flow

The simplified surge chamber model consists of a rectangular tank having two circular input pipes connected to one of its walls, and one circular output pipe connected to the opposite wall. One of the two input pipes is horizontally aligned with the output. The bottoms of each of the three pipes are flush with the floor of the chamber (refer to Figure 3.1). The two input pipes each have a valve controlling the flow rates and allowing three different permutations of input pipes under operation. The configuration in which the one operating input pipe was offset from the output pipe is selected here to introduce the reader to the topology of the flow in the simplified model of a surge chamber. In this configuration, the jet coming from the input pipe impinges on the downstream wall of the surge chamber and is deflected (see Figure 2.1). The part of the flow deflected upward impinges on the free-surface creating a bump. It then folds on itself to feed the principal vortex, which occupies a large volume of the chamber. The two ends of the principal vortex are located on i) the side wall closest to the inlet pipe, and ii) the downstream wall (close to the output pipe). A secondary vortex of smaller importance is also observed under the jet. The flow in the corner of the chamber that is facing the output pipe is almost stagnant with low velocities. The free-surface surrounding the bump is smooth and well-defined, except for the region near the upstream wall and along the side wall closest to the output pipe. The flow in this region is directed upstream following the principal vortex and the free-surface folds on itself upon impingement of the flow on the upstream wall. Entrainment of air bubbles in the flow can occur in this region depending on the flow rate. Finally, the flow enters the output pipe with a swirling motion and cannot follow the sharp angle between the downstream wall and the output pipe, creating a recirculation zone.

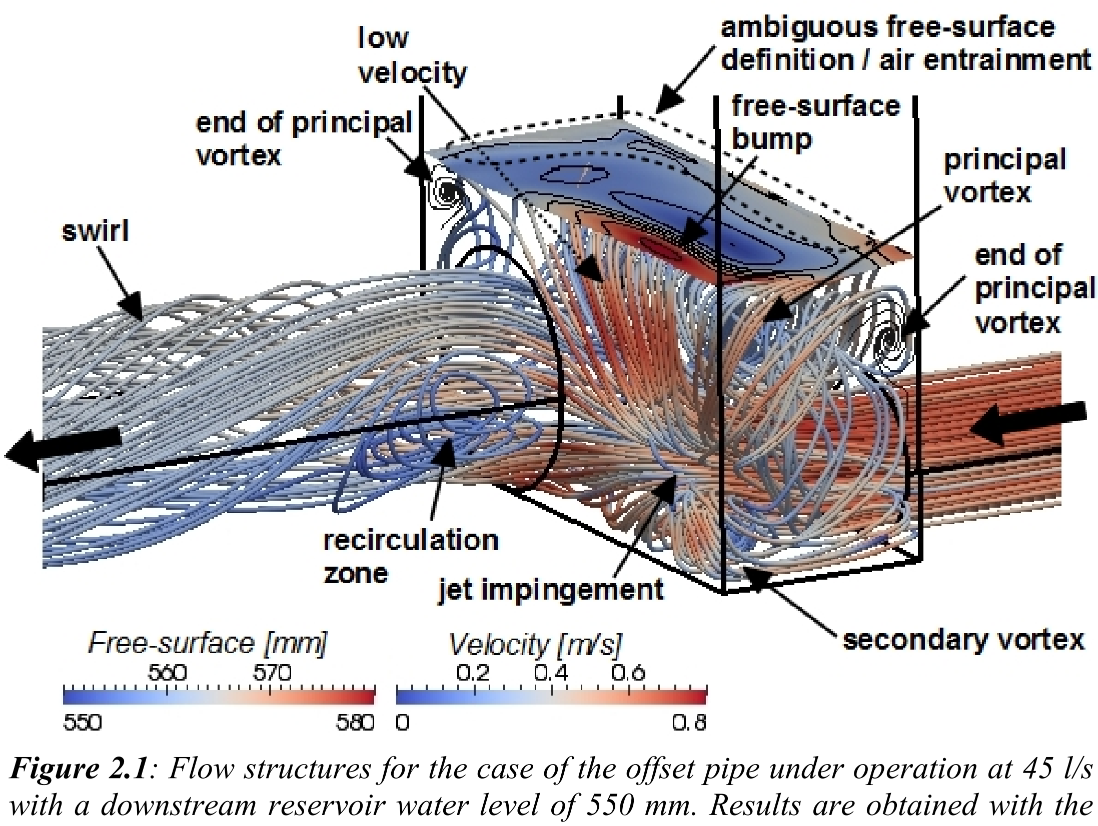

Figure 2.1*: Flow structures for the case of the offset pipe under operation at 45 l/s with a downstream reservoir water level of 550 mm. Results are obtained with the rasInterFoam solver of OpenFOAM-1.5.*

2.2. Oscillating Mass Phenomenon

A hydraulic circuit of a simplified surge chamber is presented in Figure 2.2. The circuit can represent both the laboratory test bed and power plant installations. Upstream and downstream of the surge chamber are two constant height reservoirs. The upstream and downstream reservoirs represent the dam and the river, respectively. The penstock (which carries water to the turbine) and the tail water tunnel (which discharges water to the river) are simplified by horizontal pipe segments of lengths L_1 and L_2, and diameters D_1 and D_2, respectively. The turbine is modelled by a valve which can control the flow rate. The height differences between the surge chamber and the two reservoirs are ΔH_1 and ΔH_2.

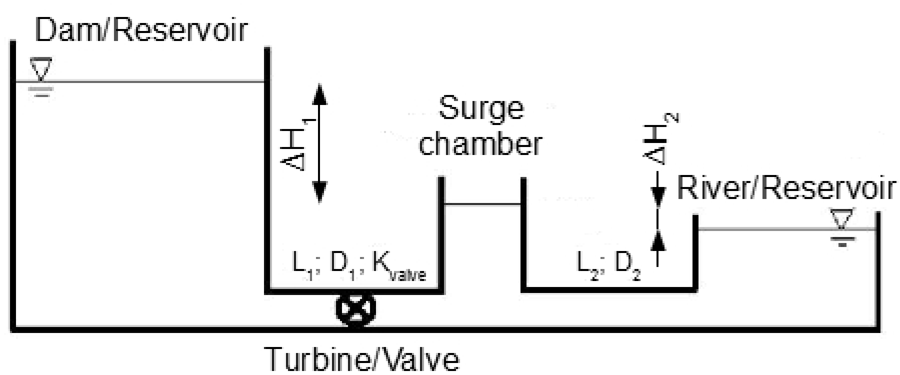

***Figure 2.2**: Schematic of the hydraulic circuit of a simplified model of a surge chamber.*

In addition to the above geometric simplifications, the pipe inlet and outlet losses are neglected, the flow is assumed to be fully-developed in both pipes, and any flow topology in the surge chamber is neglected. In what follows, the equations governing the instantaneous surge chamber free-surface level and its input/output flow rates will first be derived. The latter will then be solved for the case of non-equilibrium initial conditions. It will be shown that the flow in the surge chamber will oscillate at a fixed frequency upon reaching steady state, and that this frequency of oscillations is dependent on the circuit geometry.

By applying Newton's second law to the control volumes enclosing the fluid inside the pipes 1 and 2, we obtain the following two equations:

$$\Delta P_1 * A_1 - F_{frict,1} - F_{valve} = \rho A_1 L_1 \frac{dV_1}{dt} \qquad \textit{[Eqn. 2.1]}$$

$$\Delta P_2 * A_2 - F_{frict,2} = \rho A_2 L_2 \frac{dV_2}{dt}. \qquad \textit{[Eqn. 2.2]}$$

In the above equations, ρ is the water density, A_i and $V_i(t)$ are the cross-section area and velocity, $\Delta P_i(t)$ is the instantaneous axial hydrostatic pressure difference between the inlet and the outlet of pipe "i," and $F(t)$ represents the force exerted by the wall friction or by the valve on the control volumes. A third equation can be obtained by applying the continuity equation on a control volume surrounding the surge chamber:

$$Q_1 - Q_2 = A_{sc} * \frac{d\Delta H_2}{dt}. \qquad \textit{[Eqn. 2.3]}$$

Here, $Q_i(t)$ is the instantaneous flow rate in pipe "i," and A_{sc} is the (horizontal) cross-section area of the surge chamber. Eqns. 2.1, 2.2 and 2.3 form a system of three coupled differential equations that can be solved numerically. A 4th-order Runge-Kutta method was chosen to solve the system for the time-dependent volume flow rates in pipes 1 and 2 ($Q_1(t)$ and $Q_2(t)$, respectively), and for the surge chamber instantaneous water height. The period of oscillation of the flow upon reaching steady state can be determined by solving the case of a suddenly opened valve at time t = 0. The initial conditions are given by zero input and output flow rates ($Q_1(0) = Q_2(0) = 0$), and by equating the surge chamber water level to that within the downstream reservoir.

The solution will show that the head difference, ΔH_1, will accelerate the mass of fluid in pipe 1 until it reaches a steady value. Because ΔH_1 is large compared to the surge chamber height fluctuations, the input flow rate to the surge chamber will practically be constant. As the surge chamber receives water from the upstream reservoir, its level increases above the downstream reservoir height and the flow accelerates in pipe 2. The water level in the surge chamber continues to increase until it reaches for the first time the value corresponding to steady state. At this moment, the flow rate in pipe 2 has not yet reached steady state because of the inertia of the fluid mass. Hence, the input flow rate is larger than the output flow rate and the level in the surge chamber continues to increase beyond the steady state level, while the flow in pipe 2 continues to accelerate. When the output flow rate reaches the input flow rate, the level of the surge chamber is at a maximum. The output flow rate increases further under the action of a water level higher than the steady state value. This leads to a decrease in water level and a subsequent decrease in output flow rate. The water level will attain a minimum when the output flow rate will be equal to the input flow rate. The output flow rate will continue to decrease further, the water level will start to increase again and the overshoot/undershoot cycles will repeat themselves until the friction on the pipe walls has dissipated all the energy that is associated to those oscillations.

The oscillations will have a specific period, determined by the geometry of the surge chamber and that of the output pipe. This period can be derived analytically as (Vournas *et al.* 1995):

$$P_{oscil\_mass} = 4\sqrt{\frac{\pi L_2 A_{sc}}{g D_2^2}} \ . \qquad \textit{[Eqn. 2.4]}$$

Applying Eqn. 2.4 to the test bed under study yields an "oscillating mass" period of P_{oscil_mass}=6.70 s (0.149 Hz). We will see later in this study that both the experiments and the numerical simulations reveal some periodic oscillations of the flow at a similar frequency to that associated with the "oscillating mass" phenomenon, when the model is operated under a constant input flow rate.

2.3. Linear Natural Sloshing

In addition to the "oscillating mass" phenomenon that characterized some of the unsteady behaviours of the flow in the surge chamber model, sloshing of the free-surface at the chamber's natural frequency was also observed in some test cases. A brief derivation of the linear natural sloshing frequencies in a 2D rectangular container is described below (Henderson 1966; Ibrahim 2005; Faltinsen *et al.* 2009).

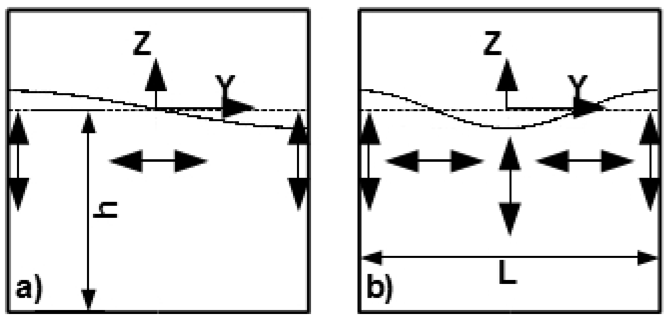

Figure 2.3*: (a) First and (b) second natural sloshing modes in a 2D rectangular tank.*

Consider Figure 2.3, which represents the first (a) and second (b) natural sloshing modes in a 2D rectangular tank of length L. The origin of the Cartesian coordinate axis is located in the middle of the tank at the mean water depth h. Let the instantaneous elevation of the free-surface from the mean water depth at any y location be defined by $\eta(y,t)$.

In the derivation of the natural sloshing frequencies, an incompressible, inviscid and irrotational flow is assumed. For such a flow, a velocity potential, $\phi(\mathrm{x,y,t})$, can be defined (irrotational flow) and combined with the continuity equation (incompressible flow) to yield the Laplace equation:

$$\frac{\partial^2 \phi}{\partial^2 y} + \frac{\partial^2 \phi}{\partial^2 z} = 0 . \qquad \textit{[Eqn. 2.5]}$$

The null normal velocities at the two vertical walls and at the bottom wall yield the boundary conditions $\left.\frac{\partial \phi}{\partial y}\right|_{y=\pm L/2}=0$ and $\left.\frac{\partial \phi}{\partial z}\right|_{z=-h}=0$, respectively. Solving the Laplace equation with those boundary conditions by separation of variables yields the following expression for the velocity potential:

$$\phi(y,z,t)=\sum_{n=1}^{\infty}\left[\alpha_n(t)\cos\left(n\pi\frac{y}{L}\right)+\beta_n(t)\sin\left(n\pi\frac{y}{L}\right)\right]\cosh\left[n\pi\frac{1}{L}(z+h)\right].\textit{[Eqn. 2.6]}$$

In the above equation, n is the mode number, and $\alpha_n(t)$ and $\beta_n(t)$ are time-dependent coefficients to be determined from the kinematic and the dynamic boundary conditions at the free-surface. The kinematic boundary condition states that the vertical velocity of a particle on the free-surface is equal to the vertical velocity of the free-surface itself, *i.e.* $-\left.\frac{\partial \phi}{\partial z}\right|_{free-surf}=\frac{\partial \eta}{\partial t}$. The dynamic boundary condition is deduced from the momentum equation written without viscosity (inviscid flow) and expressed in a conservative form. Upon integration of the latter and assuming small displacements, we obtain $\left.\frac{\partial \phi}{\partial t}\right|_{free-surf}-g\eta=0$. This dynamic equation can be differentiated once with respect to time and combined with the kinematic equation to obtain $\left.\frac{\partial^2 \phi}{\partial t^2}\right|_{free-surf}+g\left.\frac{\partial \phi}{\partial z}\right|_{free-surf}=0$.

Expressing the $\alpha_n(t)$ and $\beta_n(t)$ coefficients as harmonics and substituting the previous solution for ϕ in the last equation yields the final expression for the free-surface elevation:

$$\eta(y,t)=\frac{1}{g}\sum_{n=1}^{\infty}\left[\bar{\alpha}_n\cos\left(n\pi\frac{y}{L}\right)+\bar{\beta}_n\sin\left(n\pi\frac{y}{L}\right)\right]\omega_n\cos(\omega_n t)\cosh\left[n\pi\frac{h}{L}\right],\textit{ [Eqn. 2.7]}$$

where the modal angular frequency is expressed by :

$$\omega_n = \sqrt{gn\pi \frac{1}{L} \tanh\left(n\pi \frac{h}{L} \right)}. \qquad \textit{[Eqn. 2.8]}$$

The first two modes are represented in Figure 2.3. The nodes have purely horizontal motions while the loops have purely vertical motions. According to Eqn. 2.8, the first sloshing mode in the simplified surge chamber model, assuming a mean free-surface height of 550 mm, has a period of $P_{sloshing}$ =1.25 s (0.80 Hz).

2.4. Self-Induced Sloshing

"Self-induced sloshing" is part of the group of phenomena called "self-induced free-surface oscillations." It is defined by Saeki *et al.* (2001) as "the natural oscillation of fluid in a tank excited by the flow in the absence of other external forces." Self-induced sloshing was discovered by Okamoto *et al.* (1991), by studying a horizontally injected plane jet in a rectangular tank. Saeki *et al.* (2001) later proposed a growth mechanism for self-induced sloshing based on a feedback loop between the jet fluctuations and the sloshing motion. Some other types of self-induced free-surface oscillations include "jet-flutter" and "self-induced U-tube oscillations." Jet-flutter is the oscillation of a swell formed at the impingement point of an upward jet directed on a free-surface. Self-induced U-tube oscillations are the coupled fluctuations of the two free-surfaces of a U-shaped double-tank system that are sustained by a flow inside the tanks. In the current project, the self-induced sloshing phenomenon has been observed and quantified in both the experiments and the numerical simulations. This section summarizes the theory related to this phenomenon.

Consider the diagram shown in Figure 2.4 of the experimental setup of Chua *et al.* (2006a), which was used to study self-induced U-tube oscillations. The flow enters at the bottom of the rectangular test tank, as a plane wall-jet, and exits through the rectangular opening on the downstream wall, to a downstream tank. The two tanks form a U-tube system which has its own natural frequency of oscillation, determined by its geometry.

During operation of the test bed, two different kinds of feedback mechanisms can exist depending on the flow conditions: fluid-dynamic (direct) feedback and fluid-resonant (indirect) feedback.

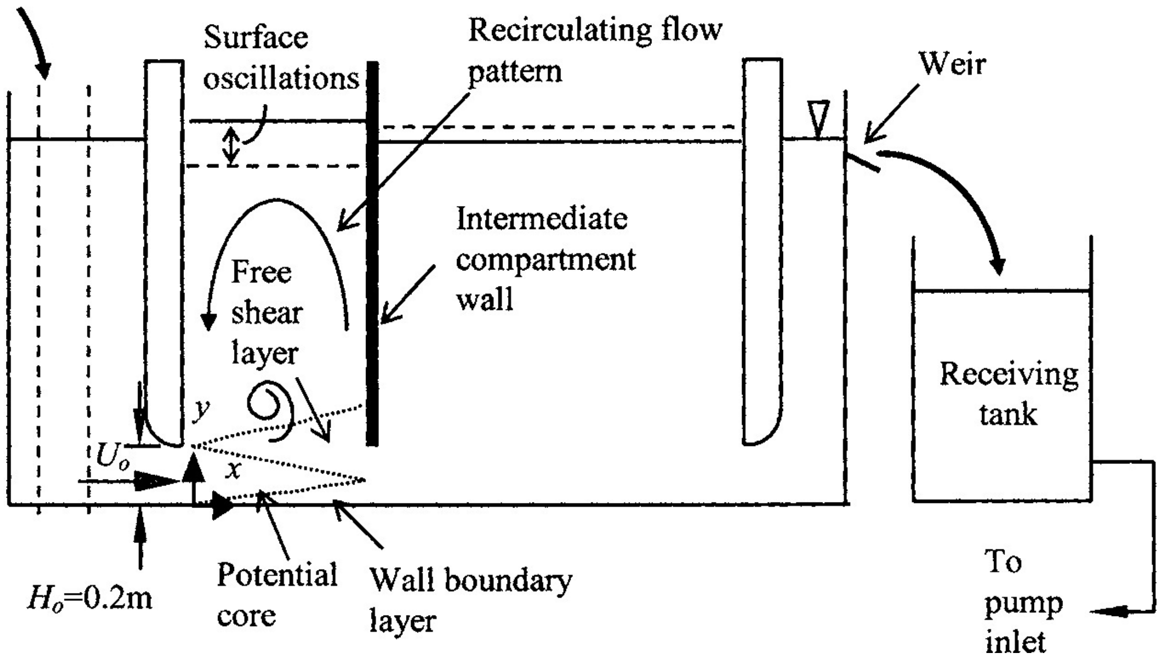

***Figure 2.4**: Schematic diagram of the experimental setup of Chua et al. (2006a) (taken from (Chua et al. 2006a)).*

2.4.1. Fluid-Dynamic (Direct) Feedback

The presence of the downstream wall in Figure 2.4 provides an impingement point for the shear layer. The flow in the shear layer will be reorganized into large coherent vortex structures as follows. Small disturbances at the jet shear layer region near the inlet can lead to the formation of vortices. Those vortices are advected by the mean flow and eventually impinge on the downstream wall. Pressure fluctuations created by the impingement will be fed back upstream, creating larger disturbances. The larger disturbances will amplify vortex formation. The cycles repeat, thus amplifying the vortices associated with the same dominant frequency. This process is called fluid-dynamic feedback and leads to a redistribution of the turbulent kinetic energy to a dominant frequency. Fluid-dynamic feedback was studied by Chua *et al.* (1999) by placing a lid on the free-surface of the test tank of Figure 2.4. Among their results, they found that for a fixed geometry and oscillation mode, the dominant frequency varies linearly with the mean inlet velocity.

2.4.2. Fluid-Resonant (Indirect) Feedback

Fluid-resonant feedback can occur when a resonator is present in the fluid system. In the experiments of Chua *et al.* (2006a), the U-tube tank system plays the role of the resonator. When the jet shear layer oscillating frequency becomes close to the natural frequency of the resonator upon variation of the flow rate, the indirect feedback mode becomes effective. The free-surfaces and the jet oscillations are "locked in" at the natural frequency of the U-tube system and the resonance mode becomes the controlling mechanism of the shear layer oscillations. Even though the jet dominant frequency is observed to normally increase with flow rate, the resonance mode will be dominant for a range of flow rates, locking in the jet oscillations until the resonance cannot be sustained by further increase in flow rate. The jet oscillations will then return to the direct feedback mode.

2.4.3. Self-Induced Sloshing in the Surge Chamber

Chua *et al.* (2008) also studied the fluid-resonant feedback mechanism by replacing the U-tube resonator with an internal density interface. In the current surge chamber experiments, the resonator role is fulfilled by the free-surface of the surge chamber model, which oscillates at a natural frequency of 0.80 Hz (Section 2.3). The downstream wall provides an impingement point for the jet shear layer, enhancing the fluid-dynamic feedback phenomenon. The best test case to observe self-induced sloshing in the current experiments is the case in which the aligned inlet pipe P1 is turned on while the offset inlet pipe P2 is turned off. This case has been chosen to investigate this unsteady phenomenon. The oscillations of the free-surface were quantified in both the experiments and the numerical simulations for multiple flow rates.

2.5. Head Losses Estimations

The exact determination of head losses in the surge chamber model is a problem involving spatial and temporal integrations of the velocity and reduced pressure at some cross-sections in the input and output pipes. The reduced pressure, p_d, is defined as a combination of the static pressure, p_{static}, and the hydrostatic pressure, $\rho\vec{g}\cdot\vec{x}$, where ρ is the fluid density and $\vec{g}\cdot\vec{x}$ is the projection of the position vector, $\vec{x}$, on the gravity vector, $\vec{g}$.

$$p_d = p_{static} - \rho\vec{g}\cdot\vec{x} \qquad \textit{[Eqn. 2.9]}$$

For problems in which gravitational effects are important, it is convenient to work with the reduced pressure instead of the static pressure, since reduced pressures at different elevations physically correspond to energy differences.

Writing the first law of thermodynamics for the control volume shown in Figure 2.5, time averaging the expression and removing the vanishing terms results in an expression for the average power loss in the surge chamber:

$$\overline{Power}_{loss} = g\left[\left(\overline{\dot{m}}_1\overline{H}_{tot,1} + \overline{\dot{m}}_2\overline{H}_{tot,2} - \overline{\dot{m}}_3\overline{H}_{tot,3}\right) + \left(\overline{\tilde{\dot{m}}_1\tilde{H}_{tot,1}} + \overline{\tilde{\dot{m}}_2\tilde{H}_{tot,2}} - \overline{\tilde{\dot{m}}_3\tilde{H}_{tot,3}}\right)\right]. \textit{[Eqn. 2.10]}$$

In the above equation, $\dot{m}_i$ is the instantaneous mass flow rate at section i. $H_{tot,i}$ is the instantaneous sum of the dynamic and reduced pressure heads at section i, averaged by the mass flow rates. The "overbar" symbol denotes time averages while "tilde" represents time fluctuations.

The first term in parenthesis of Eqn. 2.10 represents the mean contribution to the average power loss, while the second term is a correlation between time-fluctuating quantities (mass flow rates and total heads). In the numerical simulations, every term in Eqn. 2.10

can be computed during post-processing and the power loss can be determined without any simplification of the latter. However, the terms in Eqn. 2.10 are extremely difficult to measure. In the experiments, the unsteady correlation term will be neglected, and the time-averaged total head will be estimated assuming a uniform velocity profile and using a circumferential average of reduced pressure at the pipes cross-sections. The above simplifications will be discussed further in Section 5.6.

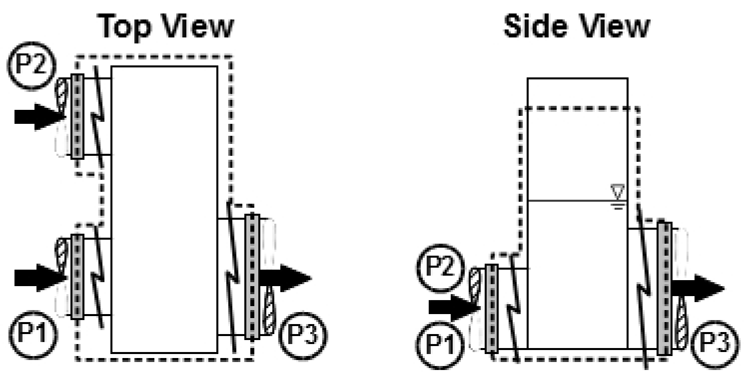

Figure 2.5*: Schematic of the control volume for the estimation of the head losses in the simplified model of a surge chamber.*

3. Experimental Method

The experiments were conducted at the Groupe Conseil LaSalle hydraulics laboratory, LaSalle (QC). The data acquired there include flow rates, reduced pressures, velocities and free-surface heights. The present chapter first describes the apparatus in which the measurements were recorded (Section 3.1). The theory behind the measurement devices used herein is then described in Sections 3.2 (Acoustic Doppler Velocimeter), 3.3 (capacitive water level probes) and 3.4 (reduced pressure measurements). Finally, a detailed description of each type of measurement is presented in Section 3.5, along with the test cases under study.

3.1. Apparatus

The apparatus consists of an upstream reservoir fed by a pump, the model of a surge chamber, and a downstream reservoir (see Figure 3.1). The first version of the apparatus that was designed showed non-negligible long term (~1 hr) fluctuations of the water levels in both the upstream and downstream reservoirs, corrupting most of the mean value measurements recorded in the surge chamber. The spatial variations in time-averaged reduced pressures and free-surface heights that were measured in the chamber through preliminary tests were found to be small (30 mm). Therefore, a considerable amount of work was required to stabilize the water levels to an acceptable limit of within 1 mm in the downstream reservoir. The apparatus described in this section, and shown in Figure 3.1, is the final version in which the measurements herein were recorded.

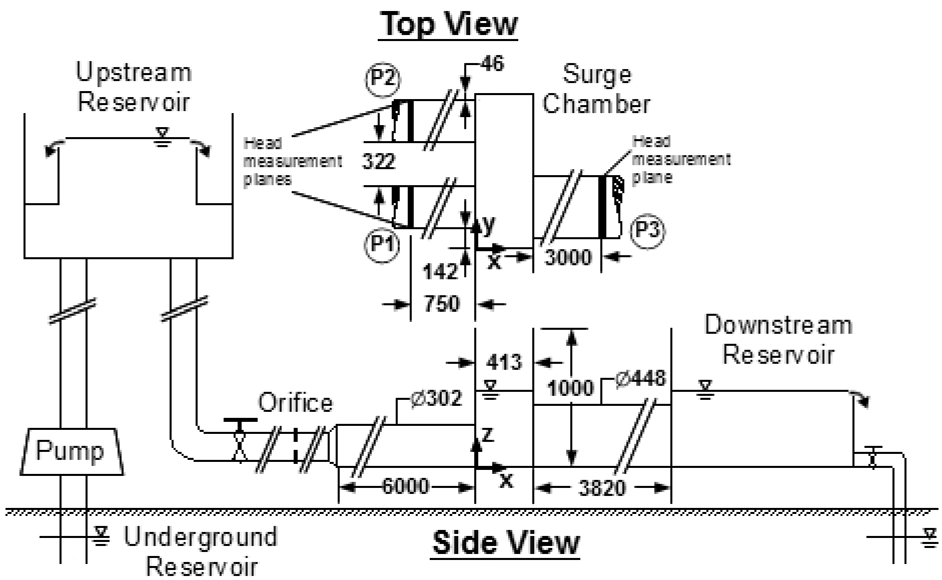

Figure 3.1: *Schematic of the apparatus and dimensions of the surge chamber model (units: mm).*

3.1.1. Upstream Reservoir

The upstream reservoir is fed by pumping water from an underground reservoir. The pump is operated with a constant input power. Because the underground reservoir is used by all models running in the laboratory, its water level may be prone to large variations during a measurement period, which can affect the level of the upstream reservoir. To minimize the effect of the variations of the underground reservoir water level on the apparatus, an enhanced perimeter weir was installed in the upstream reservoir, reducing the fluctuations of its water level by a factor of 2 compared to the previous setup. The head of the upstream reservoir is used to feed the (one or two) input pipes of the surge chamber.

3.1.2. Surge Chamber Model

The surge chamber model consists of a rectangular tank fed by two circular input pipes and drained by a unique output pipe. The first input pipe, referred to as P1, is horizontally aligned with the output pipe P3, while the second input pipe P2 is offset from P3 by approximately two pipe diameters. The bottoms of each of the three pipes are flush with the floor of the chamber. The dimensions of the surge chamber model are given in Figure 3.1.

For each input pipe, the flow rate is controlled by a valve and measured via an orifice plate meter. The flow rates in P1 and P2 can individually go up to 70 l/s when only one pipe is under operation, and up to 50 l/s each (100 l/s in total) when both are used. The typical flow rates used in this study are approximately 45 l/s, yielding a Reynolds number (VD/ν) on the order of magnitude of 10^5 for the input pipes, and a representative surge chamber Froude number ($V/\sqrt{gh}$) smaller than unity. The two input pipes have 20D of straight pipe length upstream of the chamber, while the output pipe P3 is 8.5D long.

3.1.3. Downstream Reservoir

The downstream (settling) reservoir receives the flow from the output pipe P3 and its level determines that in the surge chamber. Because the losses in P3 are small, the instabilities of the water level in the downstream reservoir have a large impact on the surge chamber water level. The fluctuations of the level of the downstream reservoir were reduced to less than 1 mm by adding a long perimeter weir. The weir height is adjustable and fine tuning of the water level of the downstream reservoir was achieved by adding a pipe-valve assembly as an extra output.

3.2. Acoustic Doppler Velocimeter

The velocity measurements were recorded using a Nortek (Vectrino) acoustic Doppler velocimeter (ADV), at a sampling rate of 25 Hz, giving the instantaneous three-dimensional velocities in a remote sampling volume located 5 cm below the head of the probe (Figure 3.2). The head of the ADV consists of a central transmitter producing short acoustic pulses and four receivers surrounding the transmitter. The receivers are inclined at 60° from the transmitter axis to acquire the echos from the particles located in the sampling volume defined by the intersections of the transmitter/receivers axes. The velocities are found by sending two short acoustic pulses separated by a small time lag, and measuring the phase shift between the signals backscattered by the particles in the sampling volume. Each analysis of a pulse-pair produces a velocity, but for noise reduction, an instantaneous velocity measurement output by the ADV is the result of the average of the maximum number of pulse-pairs velocities possible to collect during one sampling period (the inverse of the sampling frequency). The velocities are measured along the bistatic axes, the axes half-way between the transmitter axis and the receivers axes (Figure 3.2), and transformed back to Cartesian coordinates knowing the probe head geometry.

In what follows, the acoustic backscatter theory underlying the operating principle of the ADV will be first explained. This will set the stage for a discussion of sources of noise in ADV measurements, and for a presentation of the post-processing techniques used herein to treat the raw ADV data. The present section on acoustic Doppler velocimetry will conclude with a discussion of the ADV parameters that were selected for the velocity measurements in the surge chamber model.

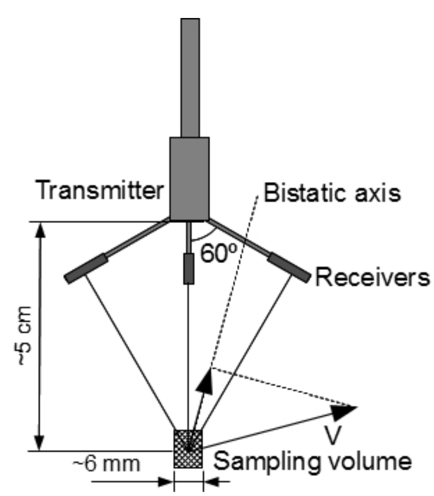

***Figure 3.2**: Schematic of the ADV head.*

3.2.1. Acoustic Backscatter Theory for Pulse-To-Pulse Coherent Doppler Sonar

Pulse-to-pulse coherent Doppler sonar systems rely on the phase change between the received echoes of a pulse-pair to determine the spatially-averaged velocity vector of the particles in the sampling volume. The objective of this section is to show how the received echoes and the particles' velocity vector can be related. This will be achieved by first deriving the expression for the phase difference between the received echoes of a pulse-pair backscattered by a *single* particle in the sampling volume (Bonnefous *et al.* 1986). Then, a similar phase difference expression will be obtained by considering the echoes from *many* particles in the sampling volume. The resulting expression will include one coherent and one incoherent contribution to the phase shift. From that result, the requirements for obtaining high-quality ADV data will become clear. The following approach for deriving the ADV phase shift expression follows that presented by Zedel (2008).

For simplicity and clarity of this discussion, it will be first assumed that the ADV is composed of a single receiver with a single particle in the sampling volume. The instantaneous distance between the transmitter and the particle, and that between the particle and the receiver will be defined to be $D_t(t)$ and $D_r(t)$, respectively. These distances can be expanded through a Taylor series as:

$$D_t(t) = D_{t0} + \frac{dD_t}{dt}t + H.O.T. = D_{t0} + V_t t + H.O.T.\,, \qquad \textit{[Eqn. 3.1]}$$

$$D_r(t) = D_{r0} + \frac{dD_r}{dt}t + H.O.T. = D_{r0} + V_r t + H.O.T.\,. \qquad \textit{[Eqn. 3.2]}$$

In the above equations, D_{t0} and D_{r0} are the transmitter-particle and particle-receiver initial distances, respectively, at $t = 0$. V_t and V_r are the particle velocities along the transmitter-particle and particle-receiver axes, respectively.

In Doppler systems, an acoustic pulse is a pressure pulse defined by an amplitude, $A[\mathbf{X}(t)]$, and a carrier frequency, ω. $\mathbf{X}(t)$ is the position vector, introduced to note that the amplitude of the sinusoidal pulse has a spatial dependency. The transmitted signal can then by written in complex form as:

$$S(t) = A[\mathbf{X}(t)]e^{it\omega}. \qquad \textit{[Eqn. 3.3]}$$

Because a single particle was assumed in the sampling volume, the echoed signal recorded by the receiver will be a copy of the transmitted pulse delayed by the time required for the pulse to travel through the transmitter-particle-receiver path, ΔT_{pulse1}, given by:

$$\Delta T_{pulse1} = \frac{D_t(t) + D_r(t)}{C}. \qquad \textit{[Eqn. 3.4]}$$

Here, C is the speed of sound in the specific fluid (water). Substituting Eqn. 3.1 and Eqn. 3.2 into the above equation (Eqn. 3.4) yields

$$\Delta T_{pulse1} = \frac{D_{t0} + V_t t + D_{r0} + V_r t}{C}, \qquad \textit{[Eqn. 3.5]}$$

neglecting the higher order terms. The second pulse is transmitted a short time τ after the first pulse. Its time delay, ΔT_{pulse2}, will be given by:

$$\Delta T_{pulse2} = \frac{D_{t0} + V_t t + V_t \tau + D_{r0} + V_r t + V_r \tau}{C}. \qquad \textit{[Eqn. 3.6]}$$

Introducing the time delays into Eqn. 3.3 gives the received signals expressions for the two pulses, $S_1(t)$ and $S_2(t)$:

$$S_1(t) = A[\mathbf{X}(t - \Delta T_{pulse1})]e^{i(t - \Delta T_{pulse1})\omega} = A[\mathbf{X}(\alpha t + \kappa)]e^{i(\alpha t + \kappa)\omega}, \qquad \textit{[Eqn. 3.7]}$$

$$S_2(t) = A\left[\mathbf{X}\left(t - \Delta T_{pulse2}\right)\right]e^{i\left(t-\Delta T_{pulse2}\right)\omega}$$
$$= A\left[\mathbf{X}\left(\alpha t + \kappa + \frac{V_t + V_r}{C}\tau\right)\right]e^{i\left(\alpha t+\kappa+\frac{V_t+V_r}{C}\tau\right)\omega}. \qquad \textit{[Eqn. 3.8]}$$

In Eqn. 3.7 and Eqn. 3.8, two new terms have been introduced, α and κ. The first term, $\alpha = 1 - \left[\frac{V_t + V_r}{C}\right]$, is a time dilatation/contraction, *i.e.* a frequency change due to the Doppler effect. The second term, $\kappa = \left[\frac{D_{t0} + D_{r0}}{C}\right]$, is a time delay offset determined by the initial position of the particle. The phase shift between the two received pulses, ϕ, can now be written for the case of a unique particle in the sampling volume. This is achieved by taking the argument of the first pulse multiplied by the conjugate of the second pulse:

$$\phi = \arg\left[S_1(t) \times S_2^*(t)\right] = -\frac{\left(V_t + V_r\right)\tau\omega}{C}. \qquad \textit{[Eqn. 3.9]}$$

In the above equation, the time lag and the carrier frequency are set by the ADV, and the speed of sound is known from the temperature and the salinity of the water. The phase shift is measured by cross-correlating the two received signals, giving the $\left(V_t + V_r\right)$ velocity term, which can be related to the velocity along the bistatic axis of Figure 3.2.

For a single particle in the sampling volume, the bistatic velocity accuracy can be determined by the ability of the Doppler system to measure the phase shift between the two received pulses. However, actual returned acoustic signals contain echoes from many particles in the sampling volume. This can cause additional errors in the measurements if the particles in the sampling volume don't have a uniform velocity, *i.e.* if they are non-correlated. Therefore, the phase shift expression for the case of multiple particles in the sampling volume will be derived in what follows.

The signal acquired by the receiver is obtained by summing the individual contributions of every particle in the sampling volume.

$$S_1(t)=\sum_{i=1}^{N}\left\{A\left[\mathbf{X}_i(\alpha_i t+\kappa_i)\right]e^{i(\alpha_i t+\kappa_i)\omega}\right\} \qquad \textit{[Eqn. 3.10]}$$

$$S_2(t)=\sum_{i=1}^{N}\left\{A\left[\mathbf{X}_i\left(\alpha_i t+\kappa_i+\frac{V_{ti}+V_{ri}}{C}\tau\right)\right]e^{i\left(\alpha_i t+\kappa_i+\frac{V_{ti}+V_{ri}}{C}\tau\right)\omega}\right\} \qquad \textit{[Eqn. 3.11]}$$

V_{ti}, V_{ri} and $\mathbf{X}_i$ are defined as the instantaneous transmitter-particle velocity, particle-receiver velocity and position of the "i th" particle in the sampling volume, respectively. N is the total number of particles in the sampling volume. Assuming that the particles' velocities at a given instant in time are functions of their spatial positions, it is possible to decompose them into a sampling volume spatial average term, $V(t)$, and a spatial fluctuation around the average, V', which gives $V_{ti}=V_t(t)+V_{ti}'$ and $V_{ri}=V_r(t)+V_{ri}'$. Substituting the latter into the received signals equations, Eqn. 3.10 and Eqn. 3.11, results in the following expressions:

$$S_1(t)=\sum_{i=1}^{N}\left\{A_i'(t)e^{i[\alpha_i t+\kappa_i]\omega}\right\}, \qquad \textit{[Eqn. 3.12]}$$

$$S_2(t)=\sum_{i=1}^{N}\left\{\left[A_i'(t)+\delta A_i(t)\right]e^{i[\alpha_i t+\kappa_i]\omega}e^{i\psi_i}\right\}e^{i\left[\frac{V_t(t)+V_r(t)}{C}\right]\tau\omega}. \qquad \textit{[Eqn. 3.13]}$$

In the above equations, the $A_i'(t)=A\{\mathbf{X}_i[\alpha_i t+\kappa_i]\}$ term is the amplitude of the signal backscattered by particle "i" and $\delta A_i(t)$ represents any amplitude difference between the returned signals for a given particle. The term $e^{i\psi_i}$ is a phase shift introduced by the spatial fluctuations of particles' velocities in the sampling volume, where $\psi_i=\left[\frac{V_{ti}'+V_{ri}'}{C}\right]\tau\omega$. This phase shift is assumed to be small, so it is possible to write

$e^{i\psi_i} \approx 1 + i\psi_i$. Substituting the latter in the equation of the second pulse, Eqn. 3.13, expanding the result and grouping the terms affected by spatial fluctuations together yields:

$$S_2(t) = S_1(t)e^{i\left[\frac{V_t(t)+V_r(t)}{C}\right]\tau\omega} + B(t)e^{i\gamma(t)}. \qquad \textit{[Eqn. 3.14]}$$

The first term on the RHS is the first pulse signal that is phase shifted by the spatial average velocity of the particles in the sampling volume. This term is called the coherent contribution to the echoed signal and needs to be as large as possible for high quality velocity measurements. The second term on the RHS is the incoherent contribution. It is caused by spatial fluctuations of velocities between the particles in the sampling volume and degrades the velocity measurements. It is defined as

$$B(t)e^{i\gamma(t)} = \sum_{i=1}^{N}\left\{\left[\delta A_i(t) + i\psi_i A_i^{'}(t) + i\psi_i \delta A_i(t)\right]e^{i[\alpha_i t+\kappa_i]\omega}\right\}e^{i\left[\frac{V_t(t)+V_r(t)}{C}\right]\tau\omega}, \qquad \textit{[Eqn. 3.15]}$$

where $\delta A_i(t)$ and ψ_i are fluctuation variables that need to be as low as possible. It is now convenient to construct a correlation coefficient between the received signals of the two pulses. Since a single ADV output velocity measurement is found from averaging as many pulse-pairs results possible to collect during a sampling time interval, the correlation is given by the average of those pulse-pairs correlations:

$$\begin{aligned} R^2(t) &= avg\left\{\frac{S_1(t)\times S_2^*(t)}{|S_1(t)|\times|S_2^*(t)|}\right\} \\ &= avg\left\{\frac{|S_1(t)|^2 e^{-i\left[\frac{V_t(t)+V_r(t)}{C}\right]\tau\omega} + S_1(t)\times B(t)e^{-i\gamma(t)}}{|S_1(t)|\times\left|S_1(t)e^{-i\left[\frac{V_t(t)+V_r(t)}{C}\right]\tau\omega} + B(t)e^{-i\gamma(t)}\right|}\right\}. \end{aligned} \qquad \textit{[Eqn. 3.16]}$$

The phase of the correlation $R^2(t)$ gives the bistatic velocity while its magnitude provides quantitative information about the quality of the measurement. If the incoherent motions of the particles in the sampling volume are absent, $B(t) = 0$ and the phase of $R^2(t)$, φ, is given by

$$\varphi = -\left[\frac{V_t(t) + V_r(t)}{C}\right]\tau\omega, \qquad \textit{[Eqn. 3.17]}$$

as is the case for a single particle in the sampling volume. The correlation magnitude is then equal to 1 and the velocity measurement is of high quality. On the other hand, as the incoherent motions of the particles in the sampling volume become important, $B(t)$ increases and the phase of the correlation diverges from $-\left[\frac{V_t(t) + V_r(t)}{C}\right]\tau\omega$. The velocity measurement is then biased by the fluctuations of the particles' velocities and the magnitude of the correlation decreases indicating that the measurement is of lower quality. A phasor diagram of the first and second pulse signal is presented in Figure 3.3. The second pulse signal, $S_2(t)$, is decomposed in its coherent, $S_1(t)e^{-i\phi(t)}$, and incoherent, $Be^{i\gamma(t)}$, contribution. The random incoherent phasor, $Be^{i\gamma(t)}$, can point in any direction and biases the estimate of the phase between $S_1(t)$ and $S_2(t)$.

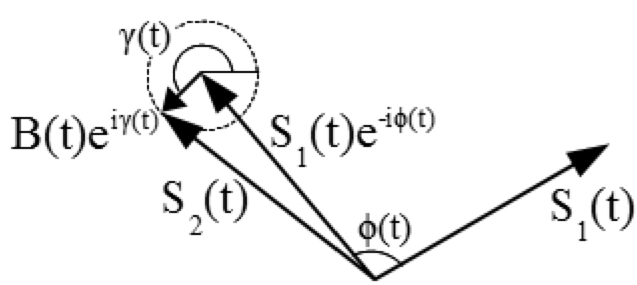

***Figure 3.3**: Phasor diagram of $S_1(t)$ and $S_2(t)$ (= $S_1(t)e^{-i\phi(t)} + B(t)e^{i\gamma(t)}$).*

3.2.2. Sources of Noise

The noise in ADV velocity measurements can come from many sources. Voulgaris *et al.* (1998) decomposed the total velocity variance along the bistatic axis, σ_t^2, as the sum of the variances due to the *sampling error* (σ_m^2), the *Doppler noise* (σ_D^2) and the noise from the *mean velocity gradient in the sampling volume* (σ_u^2):

$$\sigma_t^2 = \sigma_m^2 + \sigma_D^2 + \sigma_u^2 . \qquad \textit{[Eqn. 3.18]}$$

The accuracy of the ADV is ultimately bounded by the ability of the system electronics to resolve the phase shift, *i.e.* by the sampling error. The sampling error has been studied by Zedel *et al.* (1996), who found that σ_m^2 is proportional to the inverse of the time lag between the two consecutive pulses ($\sigma_m^2 \propto \tau^{-1}$). An increase in τ will decrease the sampling error. However, it will also tend to increase the Doppler noise by decorrelating the acoustic signals. Furthermore, a higher time lag between pulses decreases the velocity range which increases the probability of velocity ambiguity. Velocity ambiguity occurs when the phase shift of a pulse-pair signal goes beyond the [-π π] range, which produces an erroneous velocity measurement. The time lag must then be chosen as large as possible, while considering at the same time the velocity range and the Doppler noise limitations.

While the sampling error is related to the hardware accuracy, the Doppler noise and the mean velocity gradient errors are flow dependent. The Doppler noise is the result of three different contributions that tend to decorrelate the signals, *i.e.* to increase the fluctuation term $B(t)$ of Eqn. 3.16 and Figure 3.3. The three contributions to the Doppler noise are called the *finite residence time*, the *sample volume turbulence* and the *beam divergence* (Cabrera *et al.* 1987). The finite residence time contribution is caused by particles leaving the sampling volume and new ones entering with random phases between successive pulses. For the contribution due to sample volume turbulence, eddies of spatial scales on the same order, or smaller than, the sampling volume cause the particles to have a distribution in velocity within the sampling volume. Similarly, the beam divergence contribution is due to the size of the sampling volume. Particles from different locations in the sampling volume will have slightly different bistatic axes, causing an erroneous velocity distribution. Finally, if the velocity gradient of the mean flow is such that it produces a significant velocity difference across the sampling volume, the measured phase differences will not be exact, biasing the velocity measurements (Lhermitte *et al.* 1994).

3.2.3. Post-Processing Technique

The ADV data should generally not be used without proper post-processing techniques. Typical ADV data post-processing include the following two steps: deletion of low correlation and low signal-to-noise ratio (SNR) samples, and the use of a despiking algorithm. In this study, data samples having correlation amplitudes lower then 70% and SNR lower than 15 dB were removed from the set, according to the manufacturer's specifications. Then, spikes caused by high turbulence intensity, velocity ambiguity or air bubbles in the flow were removed from the data sets. Many despiking algorithms are available, *e.g.* the minimum/maximum threshold filter, the acceleration thresholding method, the wavelet thresholding method and the velocity correlation filter. The despiking algorithm used in this study is the 3D phase space threshold method, originally proposed by Goring *et al.* (2002) and later modified by Wahl (2003).

The phase-space method (as modified by Wahl) is based on the principle that differentiating a signal enhances its high-frequency components and that the good data will lie within a cluster in a phase-space plot, while points suspected to be spikes will lie outside the cluster. An example of a phase-space plot for the u velocity component is shown in Figure 3.4, where every sample of the set is represented by a dot in the 3D $u-\Delta u-\Delta^2 u$ Cartesian coordinate system with axes corresponding to the velocity magnitude, and its first and second derivatives, respectively. The velocity derivatives are computed from the two following equations:

$$\Delta u_i = \left(u_{i+1} - u_{i-1}\right)/2\,, \qquad \text{[Eqn. 3.19]}$$

$$\Delta^2 u_i = \left(\Delta u_{i+1} - \Delta u_{i-1}\right)/2\,. \qquad \text{[Eqn. 3.20]}$$

In the original phase-space of Goring *et al.* (2002), the means of u, Δu and $\Delta^2 u$ were removed from the data set before constructing the phase-space plot. Wahl uses the medians of u, Δu and $\Delta^2 u$ instead of the means for a more robust estimator of location.

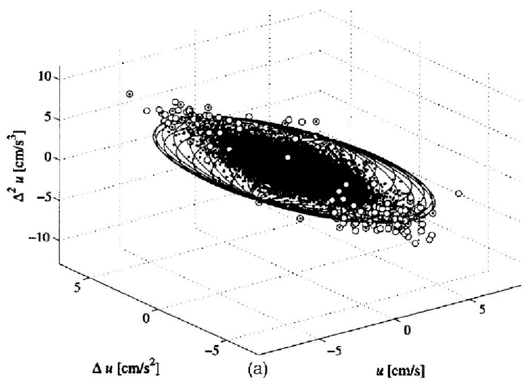

***Figure 3.4**: Example of a phase-space plot for the "u" velocity component (taken from (Mori et al. 2007)).*

The next step in the phase-space despiking algorithm is to construct an ellipsoid around the data that will discriminate good and bad samples. A sample lying outside the ellipsoid will be rejected. Chauvenet's criterion is used to define the rejection probability. The rejection probability is multiplied by a scale estimator to determine the exclusion thresholds, *i.e.* the principal axes of the ellipsoid in the phase-space plot. Instead of using the standard deviations of the u, Δu and $\Delta^2 u$ variables in the computation of the ellipsoid axes lengths, Wahl uses the median of the absolute deviations (MAD) from the sample median. This scale estimator is more robust than the standard deviation and allows the despiking algorithm to be non-iterative since the MAD will not vary much after removal of the spikes. A non-iterative despiking algorithm also has the advantage that no data reconstruction is required if one's interest is on the mean value of the time-series. The orientation of the ellipsoid is found from the u, Δu and $\Delta^2 u$ variables as in Goring *et al.* (2002).

The data set is also plotted in different phase-space plots for the other two velocity components. When a sample is removed from any velocity component, it is also removed from the other velocity components. The factors producing spikes generally affect a single beam velocity, but since the latter is used to compute all three Cartesian velocity components, all of them are affected and should be removed. After removal of the spikes, no replacement was done in this study since the interest is on the mean velocity values, for which computations do not require time-series sampled at a constant time interval.

3.2.4. Parameters of the ADV

The main difficulty in measuring the velocity field of the surge chamber model with the ADV was to obtain data of high quality (*i.e.* large correlation magnitudes). Decorrelation of the signal was believed to be due to the large mean velocity gradients, the high turbulence intensity and the presence of small air bubbles in the flow under specific conditions of operation. The user-defined parameters of the ADV were then set to achieve good correlation amplitudes (above 70%) for most of the samples. The SNR was not a limiting factor in this study. The water at the Groupe Conseil LaSalle facilities is naturally rich in particles and choosing the highest available power level for operating the ADV yielded sufficiently high SNR for most of the samples.

The water temperature was measured in the downstream tank with a thermometer (to an accuracy of ±0.1 ºC) prior to each ADV measurement period. The speed of sound was set accordingly to Wong *et al.* (1995) from this temperature reading and setting the salinity of the water to zero. An increase of the velocity range resulted in large improvements in the correlation magnitudes. A large velocity range means a smaller time lag between two successive pulses, which tends to decrease the noise. The velocity range was then set to its highest value, 400 cm/s, keeping in mind that sampling errors were increased by using such a high range. The sampling frequency was also set to its highest available value, 25

Hz. With a high sampling frequency setting, each individual velocity measurement is composed of a fewer number of pulse-pair velocities. In that way, aliased pulse-pair velocities can be easily detected and removed at the post-processing stage (Section 3.2.3), since they contaminate an individual velocity measurement made of fewer otherwise good pulse-pair velocities. The noise increase in individual velocity measurements associated with a high sampling frequency is not an issue in this study since the interest is on the mean velocities. The last two ADV parameters set by the user, the pulse length and the vertical height of the sampling volume, had smaller effects on the quality of the data. The pulse length was chosen to be large (2.4 mm) for a good SNR and the sampling volume height to be small for a good spatial accuracy (3.1 mm). Further details on the ADV velocity measurements will be discussed in Section 3.5.

3.3. Capacitive Water Level Probe

Capacitive water level probes were used in this study to measure the instantaneous water level at different locations in the surge chamber. The outputs from those probes were used to find the time-averaged water heights, and the frequencies and amplitudes of the free-surface oscillations. The present section concentrates on the basic operating principles of such probes. Details on the measurements will be given in Section 3.5.

The capacitive water level probe relates the water level to a voltage. As shown in Figure 3.5, the probe is composed of a sensing element and signal conditioning electronics. The sensing element consists of a thin insulated copper wire wrapped around a stainless steel rod. When partially immersed in water, this assembly produces a capacitor in which its capacitance is proportional to the length of the wire that is submerged. Since water is conductive, it is at the same potential as the stainless steel rod. The water and the copper are the two electrodes of the capacitor, while the insulation around the copper wire plays the role of the dielectric material. The value of the capacitance formed in this way is practically equal to the capacitance between the electrodes below the liquid-air interface. This capacitance, C, can be estimated by (Reverter *et al.* 2007):

$$C = 2\frac{2\pi\varepsilon_0\varepsilon_r}{\ln(d_2/d_1)}h. \qquad [Eqn.\ 3.21]$$

In the above, $\varepsilon_0\varepsilon_r$ is the electric permittivity of the wire insulation, h is the water level, and d_1 and d_1 are the internal and external diameters of the insulation, repectively. The factor of two takes into account that the wire is wrapped around the rod, which doubles the capacitance.

The signal conditioning electronics consist of an oscillator, a capacitance-to-voltage converter, amplifiers and filters. The output voltage from the converter, V_{out}, is given by

$$V_{out} = f_{in}V_{in}RC, \qquad [Eqn.\ 3.22]$$

where V_{in} is the supplied input voltage, f_{in} is the generated frequency input, and R and C are the external resistance and capacitance, respectively. f_{in}, V_{in} and R are held constant such that V_{out} is linearly related to C, or to the water height, h, by the use of Eqn. 3.21.

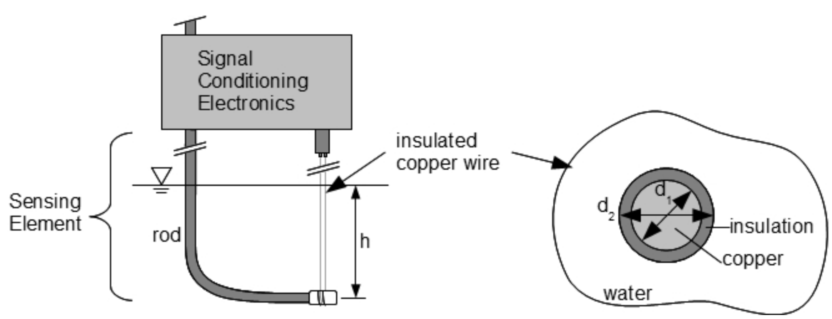

***Figure 3.5**: Schematic of the capacitive water level probe.*

In this study, the capacitive water level probes were statically calibrated in a quiescent water tank at the temperature of the test bed by mounting them on a fixed ±0.1 mm precision vernier scale. Ten points were taken for each calibration using a 10 mm increment in water depth between each point. The heights were related to voltages by a least-square linear fit. The coefficients of determinations for all calibrations were above 0.9999. The probe output voltages varied from 0 to 7.5 volts. The maximum instantaneous water depth difference, *i.e.* the minimum wire length required before saturation, is 100 mm. The ratio of exterior to interior diameters of the insulation changes the ratio of water depth to output voltage, h/V_{out}. The chosen wire insulation characteristics should yield a value of h/V_{out} as low as possible to reduce the discretization errors, but not too low to allow a working range of 100 mm before reaching saturation. A 22 gauge copper wire was used in this study giving a value of h/V_{out} of 13 mm/V, respecting the above requirements.

The output voltages from the capacitive water level probes were send to a 16-bit A/D card of 100 kHz maximum sampling rate. The acquisition was controlled by the TracerDAQ Pro software of Measurement Computing.

3.4. Pressure Measurements

The pressure measurements in this study were limited to time-averaged values of reduced pressure recorded at different locations along the pipe and the chamber walls. Mean reduced pressure measurements were obtained by linking a 1/64" diameter hole drilled on the test bed wall to a cylindrical container of large cross-sectional area through a flexible plastic tube. The water level inside the cylindrical container was measured using a rod with a sharp point at its end that was mounted on a fixed ±0.1 mm precision vernier scale. The measurements were taken by manually lowering the rod until the sharp point broke the free-surface. Each vernier offset was previously determined by taking the floor of the chamber as the reference. Short term fluctuations are damped by the large cross-sectional area of the cylindrical containers. Long term instabilities were accounted for by repeating the measurements until the convergence of the average of readings was reached (see Section 3.5).

3.5. Description of the Measurements

The experimental characterization of the flow in the surge chamber model is not straightforward since it is not a conventionally studied flow. Preliminary numerical simulations and measurements were performed at an early stage, to target key quantities that would fulfill the project objectives: understanding and characterizing the unsteady phenomena, and validating the rasInterFoam solver with the experimental measurements. Efforts were made to characterize the major features of the flow. Measurements include averaged head losses, free-surface profiles, velocities and downstream wall reduced pressure profiles, and unsteady variations of the free-surface heights.

Four test cases were studied. In the first case (Case #1), pipe P1 was closed while P2 was adjusted to an input flow rate of 45 l/s. The level of the downstream reservoir was set to 550 mm, which corresponded to the lowest level of operation that was tested. Case #2 is a variant of the first case, with the input flow rate through P2 increased to 55 l/s. This case was chosen since a higher flow rate leads to the entrainment of air bubbles into the flow at the free-surface. A mixture of air bubbles and water in some regions of the flow represents an additional challenge for the numerical simulations. In Case #3, the downstream reservoir level remained at 550 mm, but the flow rates of both input pipes P1 and P2 were adjusted to 45 l/s each (for a total flow rate in P3 of 90 l/s). The fourth and last case under study (Case #4) had pipe P1 under operation (and P2 closed) with a downstream reservoir level of 550 mm. In this configuration, sloshing at the surge chamber's natural frequency had previously been reported by Houde *et al.* (2007). The analysis will be furthered in this study by investigating the effects of the flow rate on the oscillations of the free-surface.

In addition to the above cases, the effects on the surge chamber losses of the input flow rate and the downstream reservoir height will be characterized for the three possible permutations of input pipes operation: P1, P2, P1 & P2. Table 3.1 below summarizes the measurements.

	Input Pipes	Flow Rates [l/s]	Water Levels [mm]	Measurements
Case #1	P2	45	550	Free-surface profiles Velocity field Pressure profiles Free-surface oscillations Losses
Case #2	P2	55	550	
Case #3	P1 & P2	45 & 45 (90)	550	
Case #4	P1	variable	550	Free-surface oscillations
Losses	3 permutations	variable	variable	Losses

***Table 3.1**: Summary of the measurements.*

In Table 3.1, each case is described by three parameters: the input pipes under operation, the input flow rates and the water levels in the downstream reservoir. The five types of measurements under the "Measurements" column require further explanations. In what follows, each of them will be described by the manner in which data were collected, and how they were processed.

3.5.1. Free-Surface Profiles

Five capacitive water level probes were fixed on a support beam aligned with the chamber's y-axis. As shown in Figure 3.6, the five probes were located at y distances of 250, 500, 800, 950 and 1075 mm, and moved between eight different x-positions for a total of 40 measurement locations inside the chamber. For each of the eight sets of x-positions, the output signals from the five probes were acquired for a period of five minutes at a sampling rate of 25 Hz. The sampling period was sufficiently long for the mean to converge within an acceptable uncertainty. However, due to long term fluctuations still present in the test bed, the process was repeated ten times. Therefore, ten different means were obtained for each of the 40 measurement points. Thompson's criterion for rejecting outlying data points was used to average the ten means and to compute the standard deviations of the sets (Wheeler *et al.* 2004). The modified

Thompson technique eliminates values that have low probability of occurrence by comparing the data point having the largest deviation from the mean to the standard deviation of the set multiplied by a predetermined factor. The latter decreases in value with decreasing sample size. The process is iterative, eliminating one data point at a time. Large standard deviations characterized regions that were more affected by the long-term instabilities (order ~1 hr) of the flow in the surge chamber.

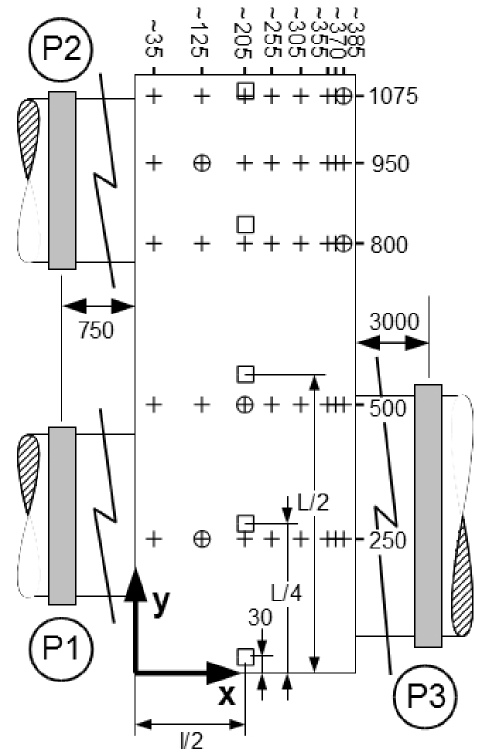

Figure 3.6*: Top view of the measurement locations for the mean free-surface profiles (40 "+" symbols), the free-surface oscillations of Cases #1 to #3 (5 "○" symbols), the free-surface oscillations of Case #4 (5 "□" symbols) and the losses (grey rings around each pipe). (L = 1114, l = 413, units: mm)*

3.5.2. Velocity Fields

The 3-D mean velocity measurements were performed at 14 points inside the chamber (see Figure 5.1 for their locations). For the reasons discussed in Section 3.2.4, a 25 Hz sampling frequency was chosen, and a sampling period of five minutes was judged sufficient for a short term convergence of mean velocities. Furthermore, ten mean measurements were performed for each of the 14 points and Thompson's criterion was again used to obtain the average and standard deviation of each of the 14 data sets.

The principal criterion for selecting the 14 measurement locations was that a location should show an important feature of the flow and be situated in a region of low velocity gradients. Measuring velocities in high velocity gradients regions is undesirable because the magnitudes of correlations of the ADV measurements are lower. Furthermore, a measurement point located in a region of high velocity gradients might be difficult to compare with the numerical results. The flow structure represented by the measurement might be simulated correctly, but a slight translation of the latter in the simulations can lead to large discrepancies between the experimental and numerical results. Preliminary numerical solutions were used to target the 14 locations fulfilling the above mentioned criterion. The velocity field of the time-averaged solutions was inspected in the selection of the important flow structures. Points on those structures were located in regions where velocity gradients were low, and chosen by visualization of a custom created field. The latter represented the normalized fluctuation of the velocity magnitude inside the ADV sampling volume, $\left\| \vec{\nabla} U \right\| \times \frac{D}{U}$, where D is the diameter of the ADV sampling volume and U is the velocity magnitude.

3.5.3. Pressure Profiles

The reduced pressure on the downstream wall of the surge chamber was measured along a horizontal and a vertical axis passing through the axis of pipe P2, as shown in Figure 3.7. Each of the horizontal and vertical reduced pressure profiles at the chamber's downstream wall consisted of measurements at ten different locations. Each reduced pressure point was read ten times with a five minutes interval between each reading. For consistency between the measurements and the numerical simulations, the downstream reservoir height was also measured simultaneously for each reading and the pressures were adjusted to a reservoir level of 550 mm. Again, averages and standard deviations were computed for each set of ten readings, but without using Thompson's criterion.

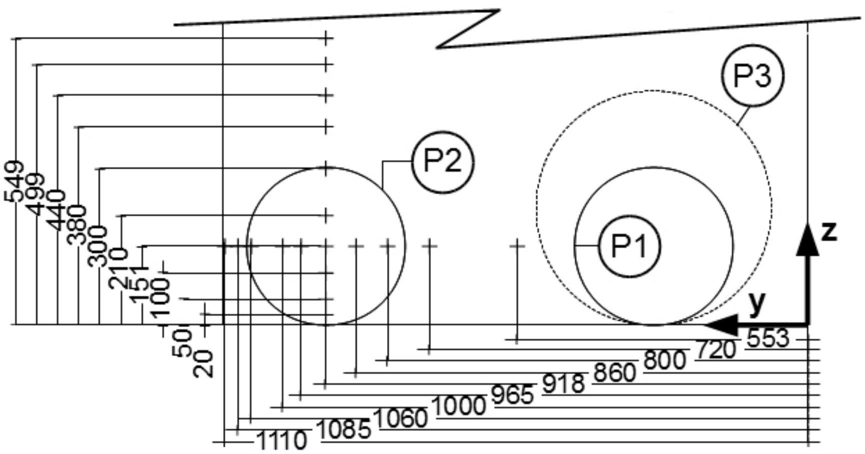

Figure 3.7*: Locations of the reduced pressure taps at the downstream wall of the surge chamber model (looking downstream). (units: mm)*

3.5.4. Free-Surface Oscillations

Cases #1 to #3

For the first three cases, five of the 40 free-surface locations were selected for unsteady free-surface measurements (see Figure 3.6). Time-series were acquired at 25 Hz over an 8 hour period, then analyzed in the frequency domain. Preliminary tests revealed no wave energy associated with frequencies beyond 5 Hz, justifying the choice of a sampling frequency of 25 Hz. Those tests also exhibited a high level of noise in the energy spectra. To reduce this noise, a combination of two different methods was used: averaging of the spectra, and the addition of spectral content from adjacent frequency bins. The content of each three adjacent frequency bins was combined and the 8 hour time-series signals were split into smaller time-series using rectangular windows. An overlapping factor of 0.5 between the windows was selected such that each smaller time-series contained half of the previous and half of the next time-series. The window length was determined from the required frequency resolution. A resolution level of 3% of the lowest frequency of interest (0.15 Hz) was judged sufficient. The resulting length of the window satisfying the above post-treatment parameters is 666 sec, yielding the ability to average 85 spectra within the 8 hour time-series. The noise reduction factor of the final averaged energy spectrum can be computed as $\left(9 \times nb_{combined\_bins} \times nb_{averaged\_spectra} / 11\right)^{0.5}$, giving 14 (Press *et al.* 2002). This factor was found sufficient for identifying potential spikes in the averaged energy spectrum that can occur at some frequencies.

Case #4

The measurement of the free-surface oscillations for the 4th case is slightly different than for the previous cases. The unsteady phenomenon to capture in this case is the natural oscillation of the free-surface in the y-z plane. To this end, the five capacitive level probes were aligned along the y-axis in the mid-plane of the surge chamber (see Figure 3.6), to measure the amplitudes and frequencies of the oscillations. The flow rates were increased from 35 to 68 l/s and each acquisition lasted a minimum of 1 hr, sampling at a rate of 50 Hz.

The time-series were again transformed in the frequency domain. The smallest frequency of interest in this case is 0.80 Hz, which is much larger than that of the first three cases (0.15 Hz). There is also much less noise in the spectra for Case #4. These two factors reduce the length of the window to be used and the length of the time-series to be acquired. The noise was reduced by averaging the spectra only. A rectangular window of length of 128 s was selected, yielding a resolution of 1% of 0.80 Hz in the spectra. Again, the overlap factor was chosen to be 0.5. The frequency of the oscillations was determined by direct inspection of the location of the spike in the final averaged power spectrum. The determination of the amplitude of the oscillations required additional steps. Because of the finite nature of the time-series, the final averaged spectrum is discretized at a fixed frequency interval. If the frequency of the real sinusoid doesn't fall directly on one of the frequency intervals (which is likely to happen), its energy leaks into the adjacent frequency bins, although the total amount of energy remains conserved (provided a rectangular window was used). To find the amplitude of the real sinusoid, its total energy had to first be computed by combining the energies of the bins adjacent to the location of the spike. Then, the amplitude of the real sinusoid was determined, noting that its energy corresponds to the rms of the sinusoid (Press *et al.* 2002).

3.5.5. Losses

As stated in Section 2.5, the losses in the surge chamber model are estimated by measuring the flow rates in pipes P1 and P2, and the circumferential averaged reduced pressure at some cross-sections in pipes P1, P2 and P3. As illustrated in Figure 3.6 by the grey rectangles, the measurement sections of the input pipes P1 and P2 were positioned 750 mm upstream of the chamber, while that of the output pipe P3 was positioned 3000 mm downstream of the chamber. They were selected with the aid of the preliminary numerical simulations results, trying to locate them far enough from the chamber such that the flow was relatively fully-developed.

The flow rates were measured by means of orifice plates installed inside the two inlet pipes. The kinetic energy heads associated with P1, P2 and P3 are found by assuming uniform cross-sectional velocity profiles at the measurement locations. The circumferentially-averaged reduced pressures are obtained directly at the pipes measurement sections. At each section, the circumferential average is estimated by measuring the pressure of a cavity surrounding 48 pressure taps equally-spaced around the pipe perimeter. The reduced pressures of the three cavities did not fluctuate significatively over long periods of time and no more than five measurements, with a five minutes interval between each of them, were required before observing a convergence of the averages of the readings.

4. Numerical Method

OpenFOAM (Open Field Operation and Manipulation) is a free, open source C++ toolbox produced by OpenCFD Ltd for the development of numerical solvers for continuum mechanics problems, including Computational Fluid Dynamics (CFD). The top-level syntax of the code is close to conventional mathematical notation for an efficient representation of coupled sets of partial differential equations (PDEs) and tensors (Weller *et al.* 1998). OpenFOAM comes with numerous C++ classes allowing problems to be discretized following different techniques such as finite volume, finite element and Lagrangian particle tracking. It also comes with many standard solvers, each of them employing a discretization technique to resolve a specific set of PDEs describing the physics of the problem (OpenCFD Ltd, 2010).

In this study, the "rasInterFoam" standard solver of OpenFOAM-1.5 was used for the numerical analysis of the flow in the surge chamber model. The algorithm implemented in this solver employs the one-fluid approach described in Section 1.3.1. It is based on the volume-of-fluid (VOF) method, combined with an interface-capturing technique for treating the free-surface (Section 1.3.2). This chapter aims to present the main characteristics of the algorithm and the numerical parameters employed in this study. The VOF method is first described in Section 4.1. The governing equations are briefly derived and summarized in Section 4.2. A description of the special numerical treatment of the phase volume fraction transport equation is outlined in Section 4.3, and the implementation of the PISO algorithm for pressure-velocity coupling in the rasInterfoam solver is discussed in Section 4.4. The entire rasInterFoam solver algorithm is summarized in Section 4.5. Finally, the numerical parameters and simplifications employed in this study are presented in Section 4.6.

4.1. VOF Method

The basis of the VOF method is to treat the two fluids as a single locally homogeneous mixture in which the volume fraction of one fluid, γ, changes in space and time (see Figure 1.2(c). In the current case of a water/air two-phase flow, the γ field is defined for each cell as

$$\gamma = \frac{V_w}{V_w + V_a}, \qquad \text{[Eqn. 4.1]}$$

where V_w and V_a are the water and air volume occupying the cell, respectively. The value of γ can be used to derive the mixture's density and viscosity at the cell centres:

$$\rho_{mix} = \gamma\rho_w + (1-\gamma)\rho_a, \qquad \text{[Eqn. 4.2]}$$

$$\mu_{eff,mix} = (\mu_{mol} + \mu_{turb})_{mix} = \gamma\mu_{mol,w} + (1-\gamma)\mu_{mol,a} + \mu_{turb,mix}. \qquad \text{[Eqn. 4.3]}$$

In the above equations, the subscripts "w", "a" and "mix" represent the water phase, the air phase and the water/air fluid mixture, respectively. The density is represented by ρ and the dynamic viscosity by μ. The subscript "mol" and "$turb$" associated with μ are for molecular and turbulent viscosity, respectively, while "eff" stands for the effective (combined molecular and turbulent) viscosity.

The volume fraction field also gives information on the interface position. In regions of pure water, γ is equal to 1, while in regions of pure air, γ equals 0. The interface is located somewhere in cells where $0 < \gamma < 1$. Since an interface-capturing technique is used in the "rasInterFoam" algorithm, the free-surface does not need to be reconstructed at each time step. Instead, the volume fraction transport equation is solved using a compressive scheme developed by Henry Weller (discussed in Section 4.3).

4.2. Governing Equations

The governing equations for the water/air mixture (that need to be solved simultaneously) are the continuity, the momentum and the γ transport equations. The general principle in their derivation is to combine the governing equations of the two individual phases by defining new thermophysical properties and velocities for the mixture. A brief derivation of the governing equations for a mixture composed of water and air will be outlined below. The derivation is limited to incompressible and immiscible flows. The viscosity of both phases is assumed constant, and heat and mass transfer between the two phases is neglected. The effects of surface tension are included.

4.2.1. Conservation of Mass

The continuity equations for the water and the air phases are:

$$\frac{\partial \alpha_w \rho_w}{\partial t} + \vec{\nabla} \cdot \left(\alpha_w \rho_w \vec{u}_w \right) = 0 , \qquad \textit{[Eqn. 4.4]}$$

$$\frac{\partial \alpha_a \rho_a}{\partial t} + \vec{\nabla} \cdot \left(\alpha_a \rho_a \vec{u}_a \right) = 0 . \qquad \textit{[Eqn. 4.5]}$$

Here, α represents the phase volume fraction such that $\alpha_w = \gamma$ and $\alpha_a = 1 - \gamma$. $\vec{u}$ is the phase velocity for water ("w") or air ("a"). Adding the above two equations together yields

$$\frac{\partial \left(\gamma \rho_w + (1-\gamma) \rho_a \right)}{\partial t} + \vec{\nabla} \cdot \left(\gamma \rho_w \vec{u}_w + (1-\gamma) \rho_a \vec{u}_a \right) = 0 , \qquad \textit{[Eqn. 4.6]}$$

which can be rewritten as

$$\frac{\partial \rho_{mix}}{\partial t} + \vec{\nabla} \cdot \left(\rho_{mix} \vec{V}_{mix} \right) = 0 , \qquad \textit{[Eqn. 4.7]}$$

using the mixture density expression (Eqn. 4.2) and by defining a water/air mixture "mass velocity":

$$\vec{V}_{mix} = \frac{\gamma \rho_w \vec{u}_w + (1-\gamma)\rho_a \vec{u}_a}{\rho_{mix}} . \qquad \textit{[Eqn. 4.8]}$$

The mixture mass velocity of Eqn. 4.8 represents the mass flux per unit area of the mixture divided by it density. Another velocity, called the mixture "volumetric velocity," will arise later in this chapter. To avoid future confusion, it's definition is given now as:

$$\vec{u}_{mix} = \gamma \vec{u}_w + (1-\gamma)\vec{u}_a . \qquad \textit{[Eqn. 4.9]}$$

It should be noted here that since the water and air phases are incompressible, the mixture volumetric velocity field is solenoidal:

$$\vec{\nabla} \cdot \vec{u}_{mix} = 0 . \qquad \textit{[Eqn. 4.10]}$$

However, the mass mixture velocity field is not solenoidal.

4.2.2. Conservation of Momentum

The momentum equations for the water and air phases are given by (Ishii *et al.* 2006):

$$\begin{aligned} &\frac{\partial \alpha_w \rho_w \vec{u}_w}{\partial t} + \vec{\nabla} \cdot \left(\alpha_w \rho_w \vec{u}_w \vec{u}_w\right) - \vec{\nabla} \cdot \left(\alpha_w \left(\vec{\vec{\Re}}_w^{mol} + \vec{\vec{\Re}}_w^{turb}\right)\right) = \\ &-\vec{\nabla}\left(\alpha_w p_w\right) + \alpha_w \rho_w \vec{g} + \vec{\mathrm{M}}_w \end{aligned} , \qquad \textit{[Eqn. 4.11]}$$

$$\begin{aligned} &\frac{\partial \alpha_a \rho_a \vec{u}_a}{\partial t} + \vec{\nabla} \cdot \left(\alpha_a \rho_a \vec{u}_a \vec{u}_a\right) - \vec{\nabla} \cdot \left(\alpha_a \left(\vec{\vec{\Re}}_a^{mol} + \vec{\vec{\Re}}_a^{turb}\right)\right) = \\ &-\vec{\nabla}\left(\alpha_a p_a\right) + \alpha_a \rho_a \vec{g} + \vec{\mathrm{M}}_a \end{aligned} . \qquad \textit{[Eqn. 4.12]}$$

The viscous and turbulent stress terms are given by $\vec{\vec{\Re}}^{mol}$ and $\vec{\vec{\Re}}^{turb}$, respectively. $\vec{g}$ is the gravitational acceleration. $\vec{\mathrm{M}}$ represents a term that accounts for the inter-phase momentum transfer. p is the static pressure.

As in the derivation of the mixture continuity equation, Eqns. 4.11 and 4.12 are added together and simplified using the mixture density, effective viscosity and mass velocity.

$$\frac{\partial \rho_{mix}\vec{V}_{mix}}{\partial t}+\vec{\nabla}\cdot\left(\rho_{mix}\vec{V}_{mix}\vec{V}_{mix}\right)-\vec{\nabla}\cdot\left(\left(\mu_{eff,mix}\right)\vec{\nabla}\vec{V}_{mix}\right)=$$
$$-\vec{\nabla}p_{d,mix}+\vec{\nabla}\left(\mu_{eff,mix}\right)\cdot\left(\vec{\nabla}\vec{V}_{mix}\right)-\vec{g}\cdot\vec{x}\left(\vec{\nabla}\rho_{mix}\right)+\int_{S(t)}\sigma K'\vec{n}'\delta(\vec{x}-\vec{x}')dS \quad \textit{[Eqn. 4.13]}$$

In the above equation, the mixture static pressure has been replaced by the mixture reduced pressure defined by

$$p_{d,mix}=p_{mix}-\rho_{mix}\vec{g}\cdot\vec{x}\,. \qquad \textit{[Eqn. 4.14]}$$

This substitution is made in OpenFOAM-1.5 to simplify the imposition of boundary conditions, as setting a constant reduced pressure on a boundary is equivalent to having a static pressure profile corresponding to a hydrostatic balance. The first term in Eqn. 4.13 is the unsteady term. The second and third terms will be called the implicit convection and implicit diffusion terms. The "implicit" qualification is added to emphasize that those terms are discretized implicitly in rasInterFoam. The four terms on the RHS are, respectively, the reduced pressure term, the explicit diffusion source term, the explicit buoyancy source term, and the explicit surface tension source term arising from the force that acts at the interface between the water and the air phases. The last three terms are discretized explicitly and treated as source terms, while the reduced pressure term is dealt with in the PISO algorithm for pressure-velocity coupling (Section 4.4). In the surface tension term, σ is the (constant) surface tension coefficient, K is the free-surface curvature, $\vec{n}$ is the normal vector of the interface, and $\delta(\vec{x}-\vec{x}')$ is the Dirac delta function. The prime notation denotes the interface and $S(t)$ is the surface of the interface. In interface-capturing methods, the surface integral of the surface tension force term is not performed directly since no interface is reconstructed at any time step (Rusche 2002). Therefore, the continuum surface force (CSF) model of Brackbill *et al.* (1992) is used to model the surface tension as a volumetric force acting within the interface region:

$$\int_{S(t)}\sigma K'\vec{n}'\delta(\vec{x}-\vec{x}')dS \approx \sigma K\vec{\nabla}\gamma\,. \qquad \textit{[Eqn. 4.15]}$$

The interface curvature can be computed from the volume fraction field as

$$K = \vec{\nabla} \cdot \left(\frac{\vec{\nabla}\gamma}{\left|\vec{\nabla}\gamma\right|} \right). \qquad [Eqn.\ 4.16]$$

4.2.3. Volume Fraction Transport Equation

The volume fraction transport equation is (Bohorquez 2008):

$$\frac{\partial \gamma}{\partial t} + \vec{\nabla} \cdot (\gamma \vec{u}_{mix}) + \vec{\nabla} \cdot \left[\gamma(1-\gamma)\vec{u}_{r\gamma}\right] = 0\,. \qquad [Eqn.\ 4.17]$$

$\vec{u}_{mix}$ is the mixture volume velocity defined earlier in Eqn. 4.9. $\vec{u}_{r\gamma}$ $(= \vec{u}_w - \vec{u}_a)$ is the water/air phase relative velocity. It is related to the mass and volume velocities as follows:

$$\vec{V}_{mix} = \vec{u}_{mix} + \gamma(1-\gamma)\frac{\rho_w - \rho_a}{\rho_{mix}}\vec{u}_{r\gamma}\,. \qquad [Eqn.\ 4.18]$$

Note that the continuity equation (Eqn. 4.7) and the momentum equations (Eqn. 4.13) use the mixture *mass velocity,* whereas the volume fraction transport equation (Eqn. 4.17) uses the mixture *volume velocity*. For consistency between the velocity definition used in the latter three equations, it is common to neglect the influence of the phase relative velocity and to therefore substitute the mixture *volume velocity* in the volume fraction transport equation with the *mass velocity* (Bohorquez 2008). The volume fraction transport equation in OpenFOAM-1.5 is formulated using this substitution. An extra compression term is also added to its formulation to yield:

$$\frac{\partial \gamma}{\partial t} + \vec{\nabla} \cdot (\gamma \vec{V}_{mix}) + \vec{\nabla} \cdot \left[\gamma(1-\gamma)\vec{u}^{*}_{r\gamma}\right] = 0\,. \qquad [Eqn.\ 4.19]$$

Here, $\vec{u}^{*}_{r\gamma}$ is a compression velocity for which the formulation will be given in the next section.

4.3. Solution Procedure for Solving the Volume Fraction Equation

As stated before, the difficulty in solving the phase volume fraction transport equation is to advect the interface without diffusing, dispersing or wrinkling it. The method implemented in OpenFOAM-1.5 for solving the γ equation uses a limiter for the explicit volume fraction fluxes, developed by Henry Weller and called the Multidimensional Universal Limiter for Explicit Solution (MULES). The MULES limits the explicit fluxes in a convective-only transport equation to keep the solution bounded. The writer believes that no publication describing the MULES method was ever published by its creator. Rusche (2002) presented in his work a method similar to the MULES and more recently, Bohorquez (2008) made use of the MULES explicit solver with only a limited explanation of the method. An attempt will be made here to describe more thoroughly the algorithm implemented in rasInterFoam for solving the γ equation, including the MULES explicit solver.

In the scheme developed by Weller, the interface compression is achieved by the third term of the γ transport equation, Eqn. 4.19. This is an artificial compression term using a compression velocity, $\vec{u}^*_{r\gamma}$, which seems to be selected from many possible choices rather than being formally derived. The choice of the compression velocity will be highlighted later in this section. For now, note that the artificial compression term is only active in the interface region due to the $\gamma(1-\gamma)$ term, and that the arbitrary compression velocity will have no effect outside this region, where either γ or $1-\gamma$ tends to zero.

The solution procedure starts with a discretization of the γ equation (Eqn. 4.19):

$$\frac{\gamma_P^n - \gamma_P^0}{\Delta t} V_P + \sum_f \left[\gamma_f^0 \left(\vec{V}_f^0 \cdot \vec{S}_f\right)\right] +$$
$$\sum_f \left[\gamma_f^0 \left(1-\gamma_f^0\right) \min\left(C_\gamma \frac{\vec{V}_f^0 \cdot \vec{S}_f}{\left|\vec{S}_f\right|}, \max\left(\frac{\vec{V}_f^0 \cdot \vec{S}_f}{\left|\vec{S}_f\right|}\right)\right)\left(\vec{S}_f \cdot \frac{\left(\vec{\nabla}\gamma\right)_f^0}{\left|\vec{\nabla}\gamma\right|_f^0 + Stabiliser}\right)\right] = 0 \text{ .[Eqn. 4.20]}$$

In Eqn. 4.20, the unsteady term is discretized using an implicit Euler scheme. The two advection terms are discretized explicitly. The superscripts "0" and "n" represent the previous and current time steps, while the subscripts "P" and "f" refer to values defined at the cell and face centres, respectively. V_P is the cell volume. $\vec{S}_f$ is the vector which magnitude equals the area of the cell face "f" and which direction is perpendicular to the face. "$Stabilizer$" is a small number added to avoid numerical division by zero. The volume fraction values at the cells faces of the second (γ_f^0) and third ($\gamma_f^0\left(1-\gamma_f^0\right)$) terms are obtained from user-defined convection schemes which were set to van Leer and Gauss Interface Compression in this study (see the OpenFOAM-1.5 source code for details). $\vec{V}_f^0 \cdot \vec{S}_f$ is the volume flux obtained from the previous time step. The compression volume flux is given by the $\left(1-\gamma_f^0\right)$ term, a compression coefficient C_γ (set to 1 in this study), the velocity normal to the CV face $\frac{\vec{V}_f^0 \cdot \vec{S}_f}{\left|\vec{S}_f\right|}$ obtained from the previous time step, and the cell face area vector projection on the unit normal vector of the interface $\vec{S}_f \cdot \frac{\left(\vec{\nabla}\gamma\right)_f^0}{\left|\vec{\nabla}\gamma\right|_f^0 + Stabiliser}$, also obtained from the previous volume fraction field.

The explicit volume fraction fluxes at each CV face are first computed from the second and third terms in Eqn. 4.20. This flux will be referred to as $(Q\gamma)^0_{f,Comp}$, where Q is the volume flow rate and the subscript "$Comp$" means that the fluxes of γ at CV faces are obtained with the artificial compression term at the interface. Note that $Q\gamma$ physically represents water volume flow rate. While the fluxes $(Q\gamma)^0_{f,Comp}$ will produce a sharp interface, they may also produce undesired oscillatory solutions. The MULES method of Weller comes into play at this point, limiting the compressive fluxes and bounding the solution. The MULES method redefines new fluxes for each CV face, satisfying the "multidimensional universal limiter" condition that bounds the newly computed γ^n_P values for each cell between the maximum and minimum previous time step values of its neighbours,

$$\min\left(\gamma^0_{nb}\right) \le \gamma^n_P \le \max\left(\gamma^0_{nb}\right). \qquad \textit{[Eqn. 4.21]}$$

To achieve that, it is required to compute the explicit fluxes of the γ transport equation without artificial compression (no third term in Eqn. 4.20) and using the bounded but diffusive Upwind Differencing (UD) scheme. This flux will be referred to as $(Q\gamma)^0_{f,UD}$. A correction flux is then defined, which is the difference between the compressive but unbounded flux and the bounded but diffusive flux:

$$(Q\gamma)^0_{f,Corr} = (Q\gamma)^0_{f,Comp} - (Q\gamma)^0_{f,UD}. \qquad \textit{[Eqn. 4.22]}$$

Finally, the explicit limited fluxes that will be used at CV faces for solving Eqn. 4.20 are given by the UD fluxes and a limited amount of correction fluxes:

$$(Q\gamma)^0_{f,Limited} = (Q\gamma)^0_{f,UD} + \lambda_f \cdot (Q\gamma)^0_{f,Corr}. \qquad \textit{[Eqn. 4.23]}$$

Here, λ_f is a limiting factor defined at each CV face to ensure the satisfaction of the multidimensional universal limiter condition given in Eqn. 4.21. Finding the faces' limiting factors λ_f is done iteratively, as will be seen shortly. However, the condition of Eqn. 4.21 needs to be first recast in terms of fluxes. The volume fraction field of the previous time step is used to find the cells' maximum and minimum possible volume fraction values for the new time step, $\gamma^n_{P,\max}$ and $\gamma^n_{P,\min}$, respectively. The maximum net cells' inflow and outflow fluxes are computed from the latter two and the γ field of the previous time step as:

$$(Q\gamma)_{P,\max IN} = \frac{\gamma^n_{P,\max} - \gamma^0_P}{\Delta t} V_P \, , \qquad \textit{[Eqn. 4.24]}$$

$$(Q\gamma)_{P,\max OUT} = \frac{\gamma^0_P - \gamma^n_{P,\min}}{\Delta t} V_P \, . \qquad \textit{[Eqn. 4.25]}$$

It should be emphasized here that fluxes limited by Eqn. 4.24 and Eqn. 4.25 will produce a γ field satisfying Eqn. 4.21. The next step is to compute, for each cell, the sum of the faces' inflow and outflow correction fluxes:

$$(Q\gamma)^0_{P,Corr,IN} = \sum_{f,\inf low} (Q\gamma)^0_{f,Corr} \, , \qquad \textit{[Eqn. 4.26]}$$

$$(Q\gamma)^0_{P,Corr,OUT} = \sum_{f,outflow} (Q\gamma)^0_{f,Corr} \, . \qquad \textit{[Eqn. 4.27]}$$

Then, the limiter factor λ_f of Eqn. 4.23 can be found iteratively for every CV face. The general procedure is outlined below:

1- Initiate the limiter factor λ_f to 1 for every face.

2- Define a new limiter factor for the cell *inflow* correction fluxes, $\lambda_{P,IN}$, for every CV. The limiter factor $\lambda_{P,IN}$ of a given cell acts on each face of the cell having inflow correction fluxes. It is used to adjust the cell net inflow correction fluxes such that when added to the net UD fluxes and the previously face-limited outflow correction fluxes, it does not exceed the maximum cell inflow fluxes defined in Eqn. 4.24. The cell limiter factor $\lambda_{P,IN}$ is calculated from

$$(Q\gamma)_{P,\max IN} = \lambda_{P,IN} \cdot (Q\gamma)^{0}_{P,Corr,IN} - \sum_{f,outflow} \lambda_f \cdot (Q\gamma)^{0}_{f,Corr} + \sum_{f} (Q\gamma)^{0}_{P,UD} \,. \quad \textit{[Eqn. 4.28]}$$

3- Bound the above calculated inflow cell limiter factors $\lambda_{P,IN}$ between 0 and 1.

4- Repeat steps 2 and 3, but for a cell limiter factor for the net cell *outflow* correction fluxes, $\lambda_{P,OUT}$. The equation for the maximum outflow fluxes is

$$(Q\gamma)_{P,\max OUT} = \lambda_{P,OUT} \cdot (Q\gamma)^{0}_{P,Corr,OUT} - \sum_{f,\inf low} \lambda_f \cdot (Q\gamma)^{0}_{f,Corr} - \sum_{f} (Q\gamma)^{0}_{P,UD} \,. \textit{[Eqn. 4.29]}$$

5- Steps 2, 3 and 4 were used to compute limiter factors for inflow ($\lambda_{P,IN}$) and outflow ($\lambda_{P,OUT}$) correction fluxes at every cell. To transpose those limiter factors from the cells to the faces, choose, for each CV face, the smallest of the three following choices: i) the limiter factor of the first cell adjacent to the CV face, ii) the limiter factor of the second cell adjacent to the CV face, or iii) the limiter factor for that face from the previous iteration. Update the limiter factors λ_f for all faces.

6- Repeat from step 2 for as many iterations as desired. In this study, 3 iterations were used.

Once the limiter factors λ_f are computed for every CV face, the values are substituted into Eqn. 4.23 and the limited fluxes are used to solve the new γ field. The rasInterFoam solver allows the possibility of using sub time steps to advance the volume fraction solution with a smaller time step than the rest of the solution. In this study, four sub-cycles were used.

4.4. PISO Implementation

When solving the continuity (Eqn. 4.7) and momentum (Eqn. 4.13) equations, two important aspects require attention: the non-linearity of the advection term in the momentum equations and the pressure-velocity coupling. The rasInterFoam solver linearises the advection term using the previous time step flow rates at the CV faces to advect the current time step velocity. Since the time steps used in this study are small, the lagged non-linearity effects should not be an issue. The pressure-velocity coupling is done using the PISO procedure proposed by Issa (1985). Its implementation in the rasInterFoam solver is described below.

The PISO algorithm is a segregated approach that solves the pressure and velocity equations in sequence. The equations to be solved in a PISO loop are the flux predictor, the pressure equation and the flux corrector. Iterations are required for the inter-equation coupling of the pressure-velocity system. In the current problem, two approaches can be followed to derive the flux predictor, pressure and flux corrector equations. One approach is to combine the momentum equation (Eqn. 4.13) with the mixture continuity equation based on the *mass* mixture velocity definition (Eqn. 4.7). In the latter approach, the mixture density appears in the unsteady term of the continuity equation and the PISO equations are derived for a compressible fluid with an extra equation for the unknown density. Alternatively, the momentum equation (Eqn. 4.13) can be combined with the continuity equation based on the *volumetric* velocity (Eqn. 4.10). In this way, the density is no longer an unknown. This is the approach implemented in the rasInterFoam solver.

To derive the PISO equations, it is convenient to write the mixture momentum equation (Eqn. 4.13) into a semi-discretized form,

$$\mathbf{A}_D \vec{\mathbf{V}}_{mix} = \mathbf{A}_H - \vec{\nabla} p_d - \vec{g} \cdot \vec{x} \vec{\nabla} \rho_{mix} + \sigma K \vec{\nabla} \gamma , \qquad \textit{[Eqn. 4.30]}$$

where the pressure gradient, buoyancy and surface tension terms are not yet discretized (Bohorquez, 2008). $\mathbf{A}$ denotes the system of linear algebraic equations yielded from the discretization of the momentum equation. For further details on the discretization techniques, please refer to the PhD thesis of Jasak (1996). Note that $\mathbf{A}$ does not include the three terms left undiscretized in Eqn. 4.30. $\mathbf{A}_D$ is the matrix containing the diagonal components of $\mathbf{A}$. $\mathbf{A}_H$ accounts for the matrix of coefficients for all neighbours (a_{nb}) multiplied by their corresponding velocities ($\vec{\mathbf{V}}_{nb}$), the unsteady source ($\frac{\vec{\mathbf{V}}_P^0}{\Delta t}$), and the explicit diffusion source term ($\mathbf{H}_{explicit\_diffusion}$):

$$\mathbf{A}_H = -\sum_{nb} a_{nb}\vec{\mathbf{V}}_{nb} + \frac{\vec{\mathbf{V}}_P^0}{\Delta t} + \mathbf{H}_{explicit\_diffusion}. \qquad \text{[Eqn. 4.31]}$$

From Eqn. 4.30, a volumetric flux prediction, ϕ^*, can be expressed by neglecting the pressure contribution:

$$\phi^* = \left(\frac{\mathbf{A}_H}{\mathbf{A}_D}\right)_f \cdot \vec{S}_f + \left(\frac{1}{\mathbf{A}_D}\right)_f \left[-(\rho_{mix})_f \left(\vec{g}\cdot\vec{S}_f\right) + (\sigma K)_f \left|\vec{S}_f\right| \vec{\nabla}_f^{\perp}\gamma\right]. \qquad \text{[Eqn. 4.32]}$$

In the rasInterFoam solver, the matrix of coefficients, $\mathbf{A}$, is computed using the velocities from the previous time step, while the neighbours' velocities, $\vec{\mathbf{V}}_{nb}$, come from the last PISO loop velocity solution. For the first PISO loop, no momentum predictor is used in this study and the neighbours' velocities, $\vec{\mathbf{V}}_{nb}$, are taken from the previous time step solution. In Eqn. 4.32, the cells' velocities from $\frac{\mathbf{A}_H}{\mathbf{A}_D}$ are interpolated to the CV faces and multiplied with the corresponding faces' area vectors. The flux contribution from the second term of the RHS of Eqn. 4.32 comes from the buoyancy and free-surface tension terms. Those terms are directly evaluated at the CV faces and multiplied by the inverse of the diagonal coefficient matrix interpolated at the CV faces' centres to obtain volume fluxes.

The flux corrector, ϕ, is obtained by adding the pressure contribution to the flux predictor:

$$\phi = \phi^{*} - \left(\frac{1}{\mathbf{A}_D}\right)_f \left|\vec{S}_f\right| \vec{\nabla}_f^{\perp} p_{d,mix} . \qquad \textit{[Eqn. 4.33]}$$

The pressure equation is developed from the continuity equation (Eqn. 4.10). Combining the latter with Eqn. 4.18 that relates the mass velocity with the volume velocity and phase relative velocity, we obtain:

$$\vec{\nabla} \cdot \vec{V}_{mix} = \vec{\nabla} \cdot \left[\gamma(1-\gamma) \frac{\rho_w - \rho_a}{\rho_{mix}} \vec{u}_{r\gamma} \right]. \qquad \textit{[Eqn. 4.34]}$$

Upon volume integration of Eqn. 4.34, the flux from the LHS term is replaced by the flux corrector (Eqn. 4.33) and the divergence of the resulting equation is taken, resulting in:

$$\vec{\nabla} \cdot \left[\left(\frac{1}{\mathbf{A}_D}\right)_f \left|\vec{S}_f\right| \vec{\nabla}_f^{\perp} p_{d,mix} \right] = \vec{\nabla} \cdot \phi^{*} - \vec{\nabla} \cdot \left[\left(\gamma(1-\gamma) \frac{\rho_w - \rho_a}{\rho_{mix}} \vec{u}_{r\gamma} \right)_f \cdot \vec{S}_f \right] . \qquad \textit{[Eqn. 4.35]}$$

All three equations in the PISO procedure are now determined. Below is a summary of the PISO procedure:

1- Construct $\mathbf{A}$. The advection term of the momentum equations is linearized using the mass fluxes from the previous time step. The neighbours' velocities are taken from the previous PISO iteration, or from the old time step solution in the case of the first PISO iteration.

2- Predict the fluxes using Eqn. 4.32.

3- Construct and solve the pressure equation (Eqn. 4.35). Its last term involving the relative velocities of the phases is neglected in the rasInterFoam solver.

4- Correct the fluxes using Eqn. 4.33.

5- Reconstruct the velocities at the cells' centres.

4.5. Algorithm Summary

So far in this section, the VOF method has been described for a water/air two-phase mixture, the mixture governing equations have been briefly derived, the solution procedure of the γ transport equation has been outlined and the PISO procedure for pressure-velocity has been presented. The entire algorithm of the rasInterFoam solver will now be summarized. Note that the subscript "mix" has been dropped for simplicity.

1- For the first iteration, initiate the following fields: γ_P^0, $\vec{V}_P^0$, pd_P^0, κ_P^0, ε_P^0. From those fields, compute the volume flux at the CV faces, $\left(\vec{V}\cdot\vec{S}\right)_f^0$, the cell density, ρ_P^0, and the kinetic turbulent viscosity, $\nu_{Turb,P}^0$.

2- Compute the new time step based on the preset value of the maximum Courant number and/or the maximum time step.

3- Using γ_P^0 and $\left(\vec{V}\cdot\vec{S}\right)_f^0$, solve the γ transport equation (Eqn. 4.19) with the explicit γ fluxes limited by the MULES explicit solver (Section 4.3). The new volume fraction field, γ_P^n, and the mass fluxes at CV faces, $\left(\rho\vec{V}\cdot\vec{S}\right)_f^0$, are obtained.

4- From γ_P^n, compute the projections of the cells' faces area vector onto the unit normal vector of the interface and the new interface curvatures at the CV centres:

$$\left[\vec{S}_f\cdot\frac{\left(\vec{\nabla}\gamma\right)_f^n}{\left(\vec{\nabla}\gamma\right)_f^n+Stabilizer}\right] \text{ and } K_P^n=-\vec{\nabla}\cdot\left[\vec{S}_f\cdot\frac{\left(\vec{\nabla}\gamma\right)_f^n}{\left(\vec{\nabla}\gamma\right)_f^n+Stabilizer}\right]\text{, respectively.}$$

5- From γ_P^n and $\nu_{Turb,P}^0$, compute the new thermophysical properties of the mixture at the CV centres. The density is found from Eqn. 4.2 while the effective dynamic viscosity is found from Eqn. 4.3.

6- Use the PISO algorithm (Section 4.4) to solve for the new velocity field $\vec{V}_P^n$, reduced pressure field, pd_P^n, and volume fluxes $\left(\vec{V} \cdot \vec{S}\right)_f^n$.

7- Solve the κ-ε turbulence model equations and get the new turbulent viscosity of the mixture $\nu_{Turb,P}^n$.

8- Set the newly computed field as the old values and return to step 2.

4.6. Description of the Numerical Simulations

The numerical simulations were run at the Institut de Recherches d'Hydro-Québec's (IREQ) high-performance computing data centre, hosting a 1000-core cluster. This supercomputer uses 500 dual-core AMD Opteron processors and can deliver up to 4 Tflops of computing power with access to a total of 12 TB of RAM and 30 TB of storage capacity. The supercomputer is also well suited for hosting parallel applications, due to its low latency, high-speed Infiniband communication network.

The numerical simulations used the "rasInterFoam" solver within OpenFOAM-1.5. They solved the Unsteady Reynolds-Averaged Navier-Stokes (URANS) equations with the k-ε model and a wall function for the treatment of turbulence. Simulations were performed for all three possible permutations of inlet pipes under operation (P1; P2; P1 & P2). The sensitivity of the results to some of the code's input parameters was tested only for the case of pipe P2 under operation.

This section describes the numerical simulations in detail. The first part treats a simulation with P2 under operation which is referred to as the *base case*. The simplifications, grid, boundary conditions, discretization schemes, time control and levels of residuals are described in detail for the base case (see Appendix A for the OpenFOAM input dictionaries). The simulation parameters that were varied from those used in the base case are then presented. Finally, the tests performed for the two other configurations of inlet pipes under operation (P1; P1 & P2) are outlined.

4.6.1. Base Case for the Numerical Simulations: P2-Q45-H550

The numerical simulation referred to as the *base case* corresponds to the experimental Case #1 (see Table 3.1), in which pipe P2 is operated at 45 l/s and the downstream reservoir water level is set to 550 mm. The simulation parameters of the base case are described below.

The grid used in the base case contains $1.73*10^6$ hexahedral cells. The fluid domain was truncated 10 diameters upstream of the chamber in pipe P2, 8.5 diameters downstream of the chamber in pipe P3, and 1 m above the bottom wall in the surge chamber. A front view of the mesh is provided in Figure 4.1, depicting the distribution of the cells in the computational domain. As in Houde *et al.* (2007), the mesh on the floor of the surge chamber was artificially deformed by making a 10 mm circular groove under the axes of P2 and P3, overcoming the difficulty associated with meshing a circular pipe tangent to a wall. The quality of the mesh in this region was reduced since the elements are packed in the 10 mm height resulting in an abrupt change in spatial resolution. The effect of this simplification on the results was not studied in this project. The heights of the cells adjacent to the walls were adjusted to yield y^+ values between 30 and 100 wherever possible, as suggested by MARNET-CFD in "Best Practice Guidelines for Marine Applications of Computational Fluid Dynamics". The heights of the first cells in pipe P2 were fixed to 2.5 mm, yielding values of y^+ between 30 and 40. In pipe P3, the heights of the first cells were gradually increased from 2.5 mm close to the chamber to 3mm at the outlet end. This led a distribution of y^+ values between 20 and 60, with larger values close to the chamber and values falling below the recommended range of 30 to 100 near the end of the outlet. The heights of the first cells in the chamber were varied from 2 to 3 mm, so that most fell in the interval $10 < y^+ < 60$. The criteria of $y^+ > 30$ was satisfied in most parts where the flow was attached to the wall, but much lower values of y^+ occurred in the recirculation zones, where y^+ is not as clearly defined. The mesh was forced to be orthogonal in the anticipated region of the free-surface, between heights of 520 to 600 mm. This section could be refined in the vertical direction independently from the rest of the mesh. The base case used a uniform cell height of 1.5 mm in this region.

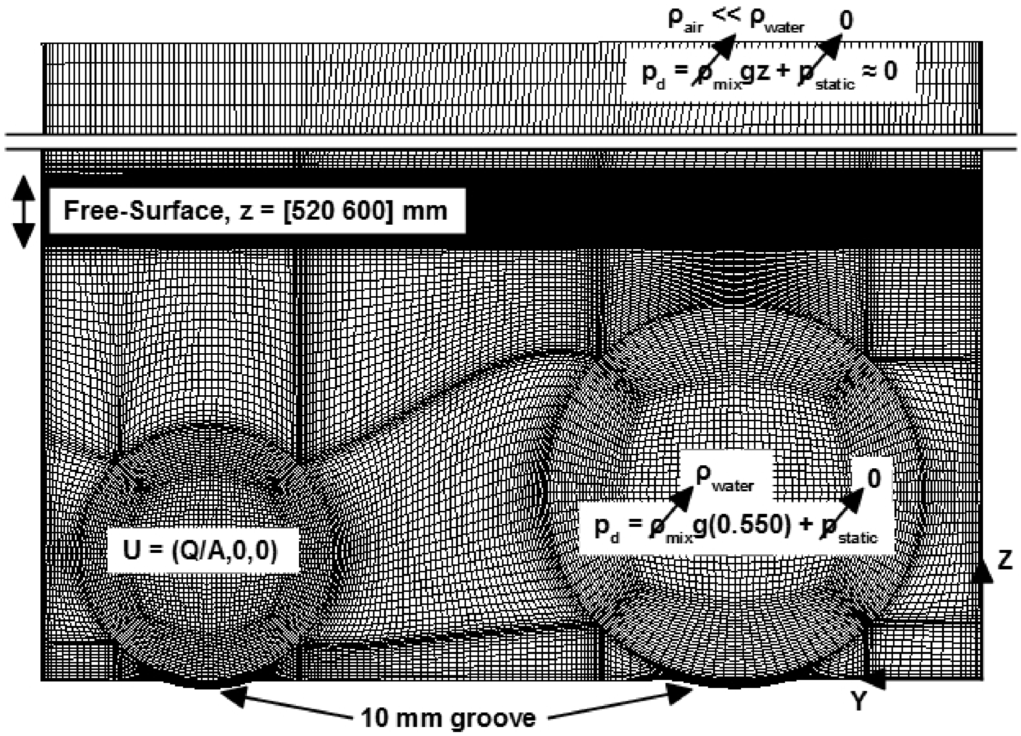

Figure 4.1*: Front view (looking downstream) of the grid used in the base case. $1.73*10^6$ hexahedra.*

The imposed boundary conditions were selected so as to simulate, as closely as possible, those of the test bed of the experiments. Because the head losses between the upstream reservoir and the surge chamber model are large compared to the surge chamber water level fluctuations, the input flow rate was assumed to be constant in time, as discussed in Section 2.2. A uniform velocity profile yielding the desired flow rate was then imposed at the inlet. The velocity conditions imposed on the other boundaries were no slip at the walls, and zero velocity gradient at the outlet and at the top of the chamber, which was open to the atmosphere. The volume fraction at the inlet was set to 1 (water), while zero volume fraction gradient was imposed on the other boundaries. As "rasInterFoam" within OpenFOAM-1.5 is solving for the reduced pressure instead of the static pressure, a uniform value was imposed at the outlet of the domain, representing a combination of the atmospheric pressure and the water height in the downstream reservoir (550 mm). The other reduced pressure boundary conditions were set to zero gradient everywhere, except at the top of the chamber. At this boundary, the reduced pressure was set to the static pressure of the atmosphere, which value should be equal to that used in the computation of the outlet reduced pressure. Because the absolute pressure has no explicit influence in this flow, the atmospheric pressure was then set to 0 (refer to Figure 4.1). The boundary conditions for the turbulent kinetic energy, k, and its dissipation rate, ε, were set to zero gradient everywhere except at the inlet where uniform values were derived from an intensity of turbulent kinetic energy of 5% and a ratio of turbulent to molecular viscosity of 10.

The terms of the governing equations (Eqns. 4.7, 4.13 and 4.19) were discretized after applying the generalized form of Gauss's theorem. The unsteady terms were discretized by an implicit Euler scheme. The gradient terms use linear interpolations of the transported quantity from the centres to the faces of the cells. The Laplacian terms use linear interpolation for their coefficients, and use explicit corrections (for the non-orthogonality of the grid) for their surface normal gradients. The divergence terms in the k and ε equations were discretized with an Upwind Difference (UD) scheme. The first divergence term of the volume fraction transport equation (Eqn. 4.19) was discretized with the Total Variation Diminishing vanLeer scheme, while the second divergence term, representing artificial compression, was discretized by the scheme called interfaceCompression in OpenFOAM-1.5. The divergence term of the momentum equations (Eqn. 4.13) was discretized with the Gamma scheme, which is a bounded scheme based on the Normalized Variable Approach of Leonard (1991) and the Convective Boundedness Criterion (CBC) of Gaskell *et al.* (1988). In this scheme, the original formulation of normalized variables was modified to be applied to arbitrarily unstructured meshes. The Gamma scheme can be interpreted as a bounded version of the Central Difference (CD) scheme. It switches smoothly from CD to UD wherever numerical diffusion is required to guarantee boundedness of the solution. The switching is based on the CBC and controlled by a user-defined coefficient, β_m, defining the extent of the transition region using a blend of UD and CD. The recommended range of β_m is between 0.1 to 0.5. A high value introduces too much numerical diffusion, while a value lower than 0.1 does not allow a smooth transition between UD and CD, introducing switching instabilities in the solution. In the base case, β_m was set to 0.1. The reader can consult Jasak (1996) and Jasak *et al.* (1999) for a more complete description of the Gamma scheme.

The levels of the residuals were set to 10^{-7} for the reduced pressure, 10^{-6} for the velocity components, and 10^{-8} for the turbulent kinetic energy and its dissipation rate. The PISO procedure used three correction loops without any momentum predictor. Four subcycles were used to solve for the gamma variable at each time step. The time steps were adjusted to a maximum Courant number of 0.8.

The quantities recorded in the experiments were also obtained in the numerical simulations. Time-averaged free-surface profiles were obtained from the time-averaged volume fraction field. Since the free-surface is not resolved in the numerical algorithm, it was found during post-processing by computing the isosurface at a volume fraction of 0.5. The velocities at the 14 experimental points were obtained from the time-averaged velocity field, while the reduced pressure profiles at the downstream wall and the averaged losses were computed from the time-averaged reduced pressure field. The oscillations of the free-surface at the same 40 x-y locations of the experiments were recorded by a custom "functionObject" (a small piece of code that is executed at every time step without explicitly being linked to the solver) in OpenFOAM-1.5. The latter can compute the free-surface height at any x-y location during the simulation, by interpolating linearly the value of the z coordinate where the volume fraction is equal to 0.5. The results can be written to a file at any time step, avoiding the need to save many complete time step solutions to the disk. Means of the free-surface heights time-series were compared to the free-surface profiles obtained from the averaged volume fraction field. No significant differences between the two methods were observed. Another custom functionObject was created to record the instantaneous heads at the measurement sections, by performing mass-flow-rate-weighted integrals of the dynamic and reduced pressure heads. Strict form of the 1st law of thermodynamics (Eqn. 2.10) could then be used to computed the average power losses in the surge chamber. A comparison of the rigorous and simplified methods for obtaining the losses in the surge chamber will be undertaken in Chapter 5.

The numerical simulations were run long enough to remove the effects of the initial conditions before starting data collection. The periodic stabilization of the flow was judged from the instantaneous heads and free-surface heights, and by monitoring the output flow rate, the inlet reduced pressure and the velocities at some locations inside the chamber. Data were collected for 200 s of simulation, which was found to be sufficient for the convergence of the analyzed quantities, and for adequate resolution of the dominant frequencies of the flow oscillations.

4.6.2. Tested Parameters of the Base Case

In addition to the base case described above, eight other numerical simulations were run for pipe P2 under operation at 45 l/s with a downstream reservoir level of 550 mm. Five different parameters of the numerical simulations were varied: i) the refinement of the mesh in the entire computational domain, ii) the refinement of the mesh in the neighbourhood of the free-surface, iii) the levels of the residuals, iv) the maximum Courant number, and v) the coefficient β_m controlling the switch between CD and UD in the Gamma convection scheme used in the momentum equations.

i) Refinement of the Mesh in the Entire Computational Domain

The base case ($1.73*10^6$ hexahedra) was also run on coarser and finer grids, containing $0.97*10^6$ and $4.20*10^6$ hexahedra, respectively. The height of the cells in the anticipated free-surface region, located between z = 520 and z = 600 mm, was kept at 1.5 mm for all three runs.

ii) Refinement of the Mesh in the Neighbourhood of the Free-Surface

The height of the cells near the free-surface for the base case was varied (from 1.5) to 3 and 0.75 mm. The resulting total number of hexahedra consequently varied (from $1.73*10^6$) to $1.49*10^6$ and $2.18*10^6$, respectively.

iii) Levels of the Residuals & iv) Maximum Courant Number

The levels of the residuals used in the base case were each lowered by two orders of magnitude to test whether or not they were adequate. The maximum Courant number was also reduced from 0.8 to 0.2, to observe the effect of a smaller time step on the unsteady behaviour of the simulated flow.

v) β_m Coefficient

In the base case, β_m was set to 0.1. Tests were run with values of 0.3 and 0.5, which were found to have an important effect on the periodic fluctuations of the flow.

The effects of these five numerical parameters will be presented with the results in Chapter 5.

4.6.3. Numerical Simulations: Cases of P1, and P1 & P2

The validation of some code input parameters was done for the case of pipe P2 under operation. Cases of pipes P1, and P1 & P2 under operation were run using the same parameters as the base case to provide additional data for comparison with the experimental results.

The simulations of pipe P1 under operation were run on a 1.14×10^6 hexahedral cells mesh. 11 different flow rates were tested, ranging from 30 to 80 l/s. For each of the 11 simulations, time-series of the velocities in the jet shear layer and the free-surface heights in the x plane in the middle of the surge chamber were recorded.

Only one simulation was run for the configuration of the two input pipes (P1 & P2) under operation, corresponding to the experimental Case #3 (45 l/s per pipe). The mesh used contains 1.92×10^6 hexahedra and the same quantities that were described in the base case were recorded in this simulation.

5. Results and Discussions

In this chapter, the experimental and numerical results are presented and discussed i) to develop a better understanding of the flow in the surge chamber simplified model, and ii) to assess the ability of the code to accurately predict the measured quantities. Firstly, the principal structures of the flow are revisited in Section 5.1, using averaged velocities obtained for Case #1. Further insight on a specific region of the flow (the impingement of the jet from pipe P2) is provided in Section 5.2, by studying the reduced pressures on the downstream wall of the chamber. The topology of the free-surface is described in Section 5.3. The unsteady behaviour of the flow is addressed in Section 5.4 (by examining the case of the aligned inlet pipe under operation) to relate the observed periodic fluctuations of the flow to the self-induced sloshing phenomenon. In Section 5.5, it is shown that another component of the periodic oscillations of the flow appears to be related to the oscillating mass phenomenon. The global losses in the surge chamber model are presented in Section 5.6. Finally, the effects of the simulations input parameters that were tested in this study are described in Section 5.7.

Note that the validation of the parameters used in the numerical simulations is only presented at the end of the current chapter. The reader should at that point be familiar with the key quantities that were analyzed, facilitating the discussion.

5.1. Averaged Velocities

The 14 time-averaged velocity vectors of the experimental Case #1 (red arrows) are plotted in Figure 5.1 against the numerical results of the base case (blue arrows), previously described in Section 4.6. The planar projections of the 3D velocity vectors are presented on the six horizontal planes on which they were measured. Three additional side views of the chamber also show their projections onto vertical planes. The planar streamlines and velocity magnitudes obtained from the base case of the numerical simulations are also shown on each of the six horizontal planes to help visualize the flow topology.

The majority of the comparisons show good agreement between the numerical results and the experiments, while some show significant discrepancies. Perfect agreement was not *a priori* expected for such a flow because of its nature (large mean velocity gradients, many

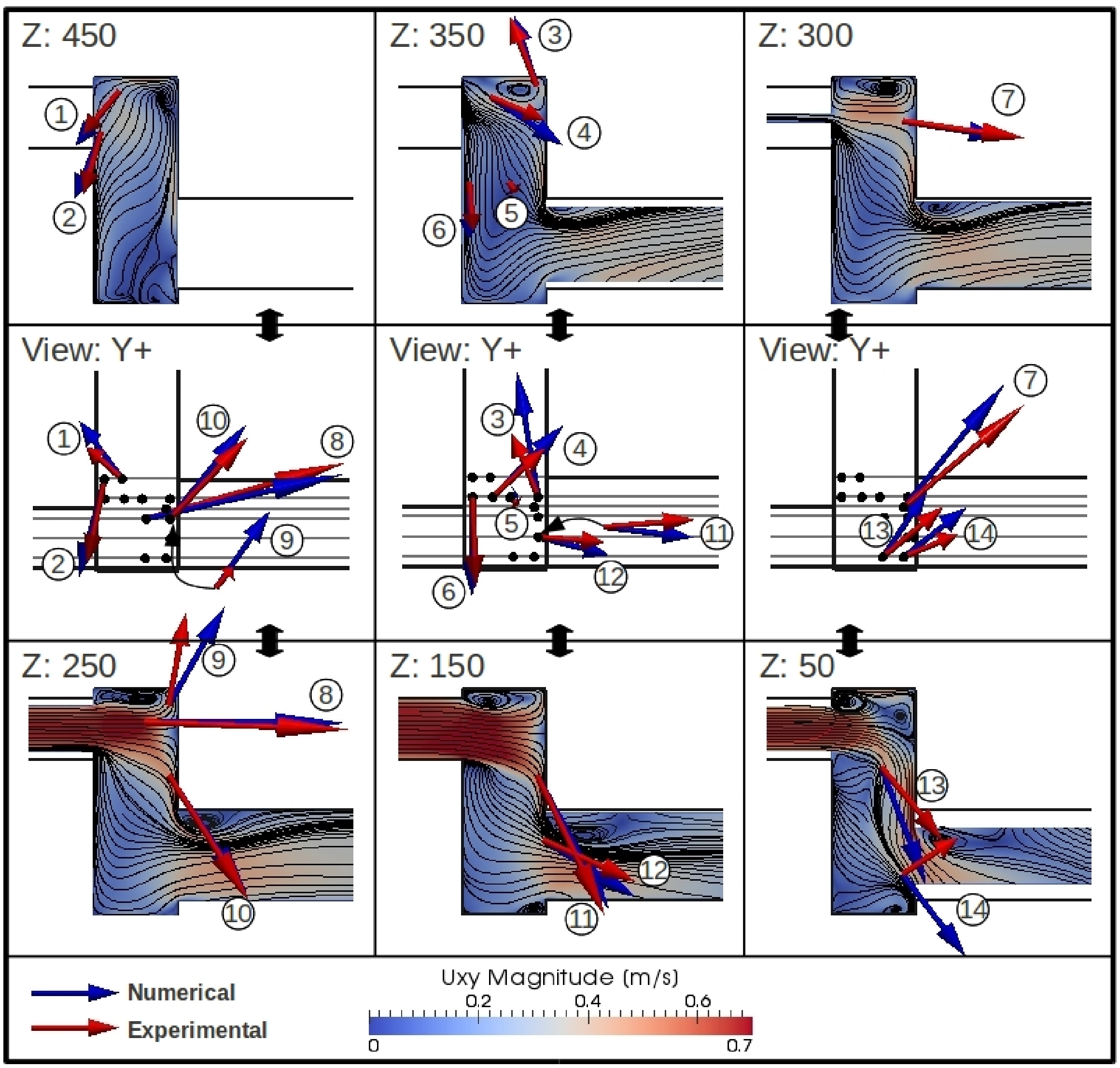

Figure 5.1: *Velocity vectors from the experimental Case #1 (red arrows) and the base case of the numerical simulations (blue arrows). The case corresponds to P2 in operation at 45 l/s and with a water level of 550 mm. The projections on six horizontal planes and the corresponding side views are shown. The planar streamlines and velocity magnitudes of the numerical simulation are also shown on the horizontal planes.*

flow separations and recirculation zones, etc.), which has always been difficult to accurately simulate. However, the global topology of the simulated flow agrees well with that of the experiments.

In particular, the impingement of the jet on the downstream wall, and its deflection upward and sideway toward P3, are shown by vectors 7, 8 and 10. Close agreement is observed between the numerical results and the experiments for these three vectors. The discrepancies of the numerical results from the experiments are below 3% for the velocity magnitudes and below 11° for the vector orientations.

Vectors 11 and 12, measured on the horizontal plane passing through the axis of P2, illustrate that the part of the jet that is closest to the output pipe (P3) flows directly through the latter. They also demonstrate that the flow cannot follow the sharp angle between the downstream wall and P3, which leads to the recirculation bubble in the outlet pipe. The orientations of the simulated vectors 11 and 12 differ from the experiments by 6° and 13°, respectively, while their magnitudes are within 5% of each other.

Like vectors 11 and 12, vectors 13 and 14 show how the flow approaches the output pipe, but on a plane close to the bottom wall. Larger discrepancies in magnitudes and orientations were observed for vectors 13 and 14 (23%-17°, and 38%-78°, respectively). These differences may be due in part to the two circular grooves that were artificially added in the simulations to the bottom wall of the chamber (for mesh generation), which should have more significant effects on the flow in their vicinities. It should be further noted that the orientation of the simulated velocity vector 14 is completely different than that of the experiments. Vector 14 is located close to the corner of the chamber around which the velocities are low. The flow stagnates in this region after having followed the principal vortex. The code might have difficulty accurately simulating this phenomenon.

The part of the jet entering the chamber close to the side wall was also characterized by the ADV measurements. The flow in this region, represented by vectors 3, 4 and 9, is deflected upward, toward the free-surface, in a swirling motion. The swirling motion, combined with the upward deflection, have been well simulated by the code, but the differences in velocity magnitudes with respect to the experiments is approximately 30%.

The flow at the free-surface is directed upstream. As it approaches the upstream wall, it is deflected downward, and might entrain air bubbles, depending on the input flow rate in the experiment. The air entrainment in the flow was minor for Case #1 (45 l/s), but significant for Case #2 (55 l/s). Vectors 1, 2 and 6 represent this part of the flow. The simulated orientations of the velocity vectors do not deviate more than 11° from the experiments. The differences in their magnitudes are 29% (vector 1), 13% (vector 2) and 11% (vector 6).

Finally, a velocity measurement was taken in the centre of the principal vortex (vector 5). The velocities recorded in the experiments and computed in the numerical base case both exhibit low magnitudes.

The 14 velocity measurements are summarized in Table 5.1.

		Vector #													
		1	**2**	**3**	**4**	**5**	**6**	**7**	**8**	**9**	**10**	**11**	**12**	**13**	**14**
Velocity	**Expt [cm/s]**	22.7	37.6	34.5	26.6	5.6	35.7	56.0	73.7	34.2	59.1	54.4	35.3	37.7	24.7
	Num [cm/s]	32.0	43.3	51.5	39.4	4.4	40.4	56.2	71.3	48.0	59.3	53.4	37.3	48.9	40.0
	Diff [%]	29	13	33	32	28	11	0	3	29	0	2	5	23	38
Direction	**Diff [°]**	10	4	20	7	47	0	11	5	30	6	6	13	17	78

Table 5.1: *Velocities from the experimental Case #1 and the base case of the numerical simulations. P2 in operation at 45 l/s and with a water level of 550 mm.*

5.2. Reduced Pressure Profiles Along the Downstream Wall

The previous section discussing the averaged velocity field characterized the principal structures of the flow inside the surge chamber model. Additional insight on the impingement of the jet from the input pipe P2 is provided in this section, by looking at the reduced pressures on the downstream wall of the chamber. The horizontal (a) and vertical (b) reduced pressure profiles passing through the axis of P2 are shown in Figure 5.2, for the experimental Cases #1 (P2 in operation, blue dots) and #3 (P1 & P2 in operation, red squares). The error bars of the experimental data points correspond to ±1 standard deviation in their sets of ten readings (see Section 3.5). Therefore, large error bars correspond to large variations in reduced pressures over long periods of time. They are mostly associated with points located in regions of high reduced pressure gradients, where a slight change in the topology of the flow might lead to large pressure variations. The results of the numerical simulations corresponding to the two experimental cases are also shown in Figure 5.2. The solid line refers to the numerical base case of P2 under operation, while the dashed line refers to the simulation that was run with both P1 and P2

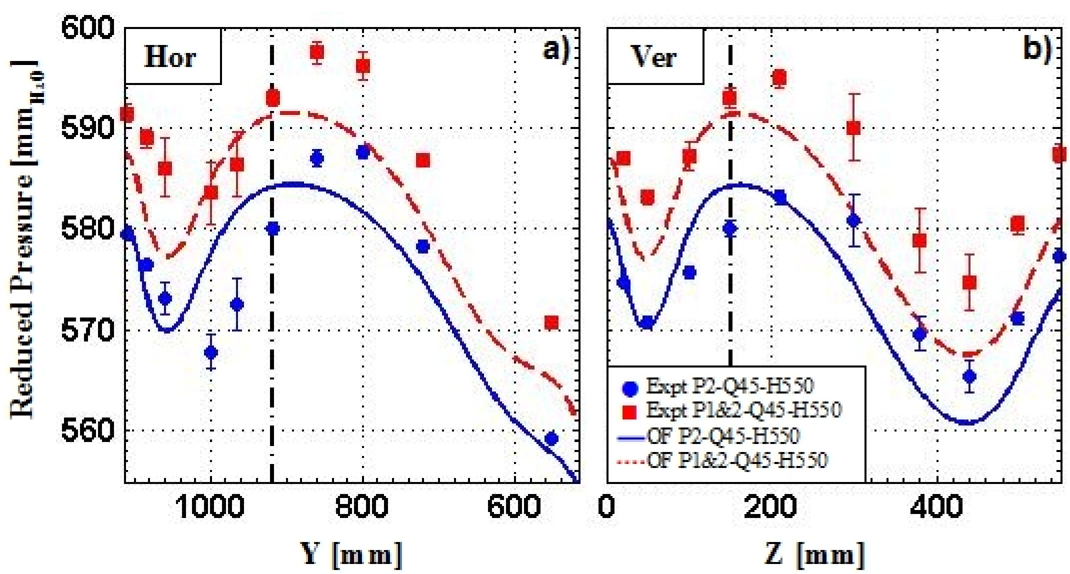

***Figure 5.2**: (a) Horizontal (z = 151 mm) and (b) vertical (y = 917 mm) reduced pressure profiles on the downstream wall of the surge chamber model for the cases of P2, and P1 & P2 in operation with a flow rate of 45 l/s per pipe (Q45) and a downstream reservoir water level of 550 mm (H550). Experiments (Expt) are represented by symbols and OpenFOAM numerical simulations (OF) by lines.*

in operation. Vertical dash-dot lines were added to Figure 5.2 to show the location of the axis of pipe P2 (at y = 917 and z = 151 mm).

P2 in Operation

The simulated shapes of the horizontal and vertical reduced pressure profiles for P2 in operation are globally similar to those measured in experimental Case #1. For both the experimental and numerical profiles, there is a local maximum near the axis of P2, corresponding to the jet impingement point. The reduced pressure decreases on both sides of the impingement point, where the flow accelerates. It then reaches a local minimum before increasing again with the decelerating flow that is directed toward the side wall (increasing y), the floor of the chamber (decreasing z) and the free-surface (increasing z). The reader can refer to Figure 3.7 for positioning of the reduced pressure taps with respect to the chamber boundaries.

A closer inspection of the reduced pressure profiles reveals local discrepancies between the simulated location of the impingement point of the jet and that obtained from the experiments. The peak in reduced pressure is horizontally shifted from the axis of P2 toward the output pipe P3 by 24 mm in the numerical simulation and by 92 mm in the experiments. Vertically, the peak in reduced pressure is shifted toward the free-surface by 11 mm in the simulation and by 88 mm in the experiments. Slight geometric differences between the physical and numerical models may, in part, cause this discrepancy (*e.g.*, the input pipe P2 might not be perfectly perpendicular to the upstream wall; the addition of the circular grooves to the floor of the chamber in the numerical simulations). Apart from the slight differences in geometry, possible discrepancies in the input conditions between the experimental test bed and the numerical simulations may also be responsible. An additional numerical simulation, not described in Section 4.6, was run using a non-uniform velocity profile at the inlet of P2, that is inclined toward P3 and the free-surface, instead of the uniform velocity profile applied in all other simulations. The simulated stagnation point of this supplemental simulation was closer to that of the experiments than was that of the base case. This observation stimulated further experiments to i) characterize the uniformity of the jet entering the chamber by pipe P2, and ii) validate or invalidate the use of a uniform velocity profile at the inlet of P2. Vertical and horizontal velocity profiles were obtained (with the ADV) across the jet at its entry in the chamber. The tests were performed with and without honeycombs/screens in the input pipe. The honeycombs/screens had a negligible impact on the measured velocity profiles and were then removed from the input pipe because they were prone to the accumulation of dirt. However, these tests demonstrated that the 20D length of input pipe in the experimental test bed yielded a sufficiently fully-developed velocity profile, and did not justify the imposition of a non-uniform velocity profile at the inlet of pipe P2 in the numerical simulations.

In general, it was also observed that the values of reduced pressure obtained numerically were lower than those obtained experimentally. This is associated with a slightly lower water level in the surge chamber due to lower simulated head losses (see Section 5.6).

P1 & P2 in Operation

The horizontal and vertical reduced pressure profiles obtained from the experiments and the numerical simulation for the case of both input pipes (P1 & P2) under operation also agree in their global shapes. Again, the simulated stagnation point is not as deflected toward P3 and the free-surface than in the experiments. The flow from pipe P1 does not seem to significantly modify the jet coming from P2. The mean water level in the chamber is slightly higher than for P2 operating alone, resulting in higher values of reduced pressures.

5.3. Averaged Free-Surface Profiles

The time-averaged free-surface profiles on 5 vertical planes are shown in Figure 5.3(a). The latter shows the results from three experimental cases, Cases #1, #2 and #3, represented by the blue dots, green triangles and red squares, respectively. The error bars of the experimental data represent ±1 standard deviations of the sets of ten measurements.

The numerical results of the base case (blue solid line), which correspond to the experimental Case #1, and those of the only numerical simulation corresponding to Case #3 (red dashed line) are also presented to compare with the experiments. Note that analogous simulations were not performed for the Case #2 experiments (green triangles). In addition to the 2D free-surface profiles, a contour plot of the free-surface height of the numerical base case (Case #1) is also presented in Figure 5.3(b), showing the global topology of the free-surface. The locations of the five vertical planes are denoted in this plot by red lines.

From Figure 5.3(b) (and Figure 2.1), it is observed that upon impingement of the jet coming from pipe P2 on the downstream wall, part of the flow is deflected upward, creating a bump in the free-surface. The height of the the free-surface decreases away from the bump, then increases again where the flow impinges on the upstream wall and at the side wall closest to the output pipe.

The two input pipes are operated at 45 l/s each in Case #3, while only P2 is under operation for Case #1, also at 45 l/s. The free-surface profiles associated with these two cases have similar shapes; the profiles of Case #3 being almost identical to those of Case #1, only shifted upward because of a higher mean water level in the surge chamber (due to higher losses). It can then be concluded that most of the free-surface perturbations are due to the flow from pipe P2, while the flow from P1 does not have much effect on the mean free-surface profiles. If Case #1 (45 l/s) is now compared to Case #2 (55 l/s), it is seen that an increase in the kinetic energy of the jet leads to a higher bump and to steeper profiles. It also leads to significantly larger amounts of air entrained into the flow where the latter, following the principal vortex at the free-surface, hits the walls of the chamber resulting in the free-surface folding on itself.

There is close agreement between the experimental and numerical results for the mean free-surface profiles, especially at the y = 800 mm plane. At the other planes, there are local discrepancies in the profiles, but the global shapes remain well-simulated. It is important to note that, in some regions, the free-surface may be less well-defined, resulting in ambiguous comparisons between the experiments and the numerical simulations. This is the case in the corner of the chamber defined by the intersection of the upstream wall and the side wall closest to the output pipe, where the free-surface was observed in the experiments to fold on itself. In this region, some air bubbles are mixed into the water for Case #1. The results of the numerical simulation of Case #1 were consistent with these experimental observations. The free-surface is sharp for most of its

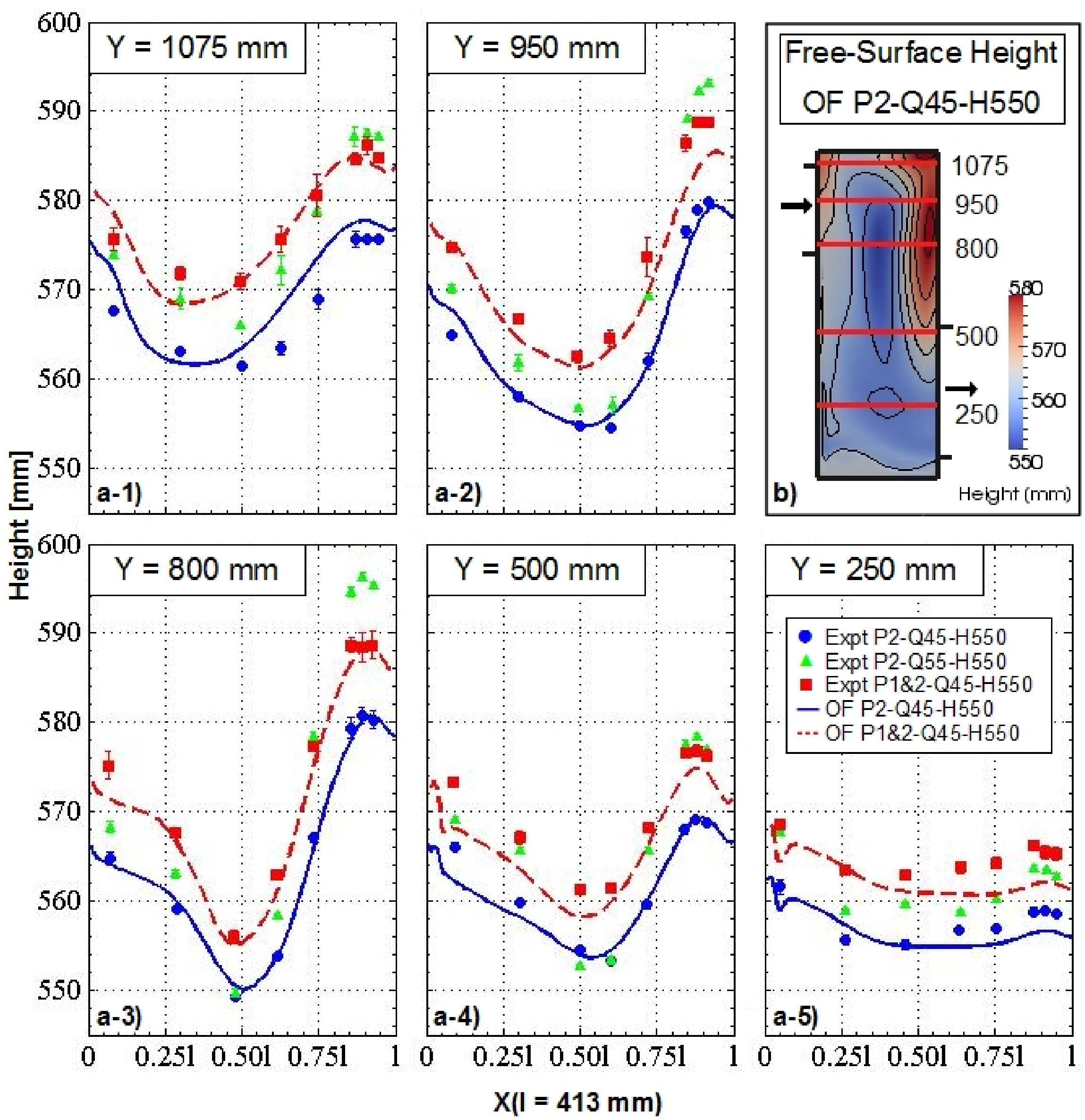

Figure 5.3: *(a) Time-averaged free-surface profiles on five vertical planes for the experimental Cases #1 (dots), #2 (triangles) and #3 (squares), and for the numerical simulations of Cases #1 (solid line) and #3 (dashed line). (b) Contour plot of the free-surface height for the numerical base case (Case #1).*

parts, except along the upstream wall and the side wall closest to the output pipe, where it is diffused vertically over many cells. This is shown in the instantaneous result of the numerical base case presented in Figure 5.4(a), in which only the cells having a volume fraction between 0.1 and 0.9 are depicted. The level of diffusion of the free-surface is further illustrated in Figure 5.4(b), which is a contour plot of the time-averaged heights of the cells having a volume fraction value between 0.1 and 0.9. The large levels of diffusion of the free-surface in some regions is believed to be related to the nature of the flow, rather than to unwanted numerical diffusion.

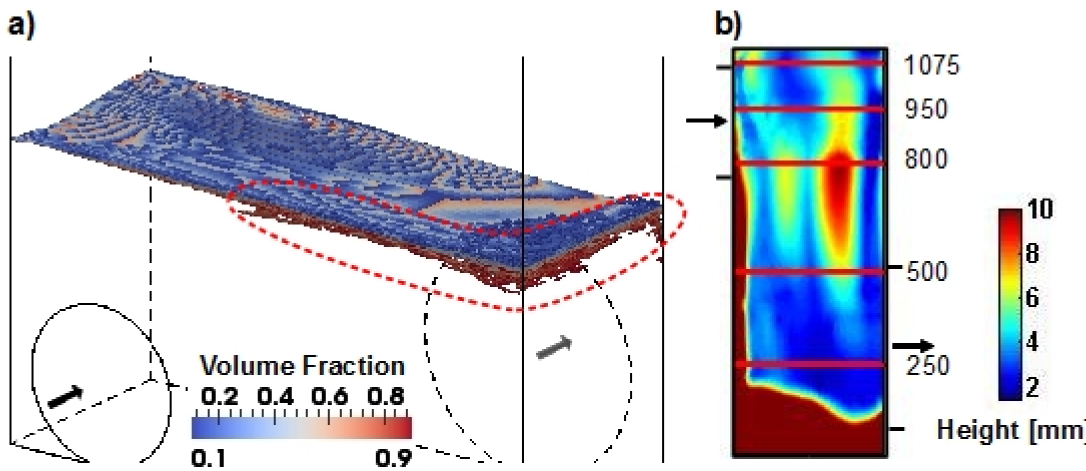

Figure 5.4: *Numerical results of the base case. (a) Instantaneous screenshot of the cells having a volume fraction between 0.1 and 0.9. (b) Contour plot of the time-averaged heights of the cells with a volume fraction between 0.1 and 0.9.*

5.4. Self-Induced Sloshing: Case #4

In Case #4, in which pipe P1 is the only pipe under operation, the free-surface was observed to oscillate at the first sloshing mode of the chamber for a range of flow rates. This section is devoted to the analysis of the free-surface oscillations, measured in the experiments and computed in the numerical simulations. The results that were obtained will first be presented. An explanation of the physical phenomenon behind the oscillations will be proposed in the remainder of the section.

The amplitudes and frequencies of the free-surface oscillations are presented in Figure 5.5 for the wide range of flow rates that were tested. Figure 5.5(b) plots the effect of the flow rate on the amplitude of the free-surface oscillations at a point located at x = 0.5*l and y = 30 mm (see Figure 3.6). According to Figure 5.5(b), the free-surface does not oscillate for low flow rates. The free-surface starts oscillating when the flow rate reaches approximately 40 l/s and the amplitude of the oscillations grows with the flow rate until it reaches a maximum. Subsequent increase in flow rate leads to a decrease in the amplitude of the oscillations. The numerical computations appear to simulate the same physical phenomenon observed in the experiments, but predict the start and peak of the oscillations to occur at slightly lower flow rates. Furthermore, the peak in amplitude of oscillations is about 34% lower than that measured in the experiments. The range of flow rates tested in the simulations was wide enough to capture the end of the oscillations occurring at high flow rates, while the maximum flow rate in the experimental test bed was limited to 68 l/s, which was found to be insufficient to yield a flat free-surface.

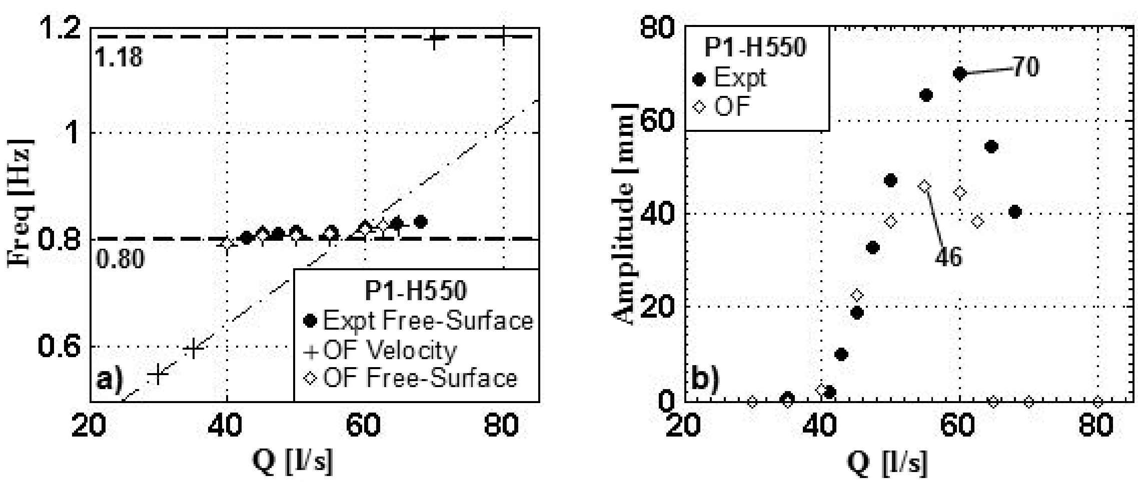

Figure 5.5*: (a) Oscillations frequencies and (b) amplitudes of the flow in the surge chamber model operated with pipe P1 in use at multiples flow rates and with a fixed downstream reservoir water level of 550 mm.*

While Figure 5.5(b) shows the numerical and experimental oscillation amplitudes of the free-surface at only one point on the x = 0.5*l plane (Figure 3.6) for multiple flow rates, Figure 5.6 shows the entire profiles on the same plane for a fixed input flow rate of 45 l/s. The data, fitted with sinusoids, reveal that the free-surface in both the experiments and the simulations is indeed oscillating in its first mode. At the flow rate of 45 l/s, the numerical simulation predicts an amplitude of oscillations 21% higher than what is obtained experimentally.

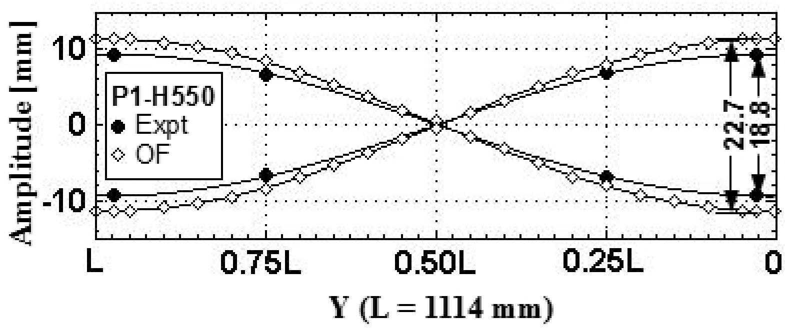

***Figure 5.6**: Comparison of the free-surface profiles obtained in the experiments and with OpenFOAM for pipe P1 in use with a flow rate of 45 l/s and a downstream reservoir water height of 550 mm (looking downstream). The profiles are located on the x = 0.5*l plane (l = 413 mm).*

According to the definition given by Saeki *et al.* (2001), the flow of Case #4 is believed to undergo self-induced sloshing since the free-surface presents sustained natural oscillations without any external force acting on it. Self-induced sloshing and other "self-induced free-surface oscillations" phenomena were studied by Chua *et al.* (1999, 2006a, 2006b, 2008) among others. Chua *et al.* investigated two different feedback mechanisms characterizing this type of flow: the fluid-dynamic feedback and the fluid-resonant feedback (see Section 2.4 for a summary of their experiments). *Fluid-dynamic feedback*, also referred to as direct feedback, is a process that leads to a redistribution of the turbulent kinetic energy to a dominant frequency. In the presence of an obstacle that can provide an impingement point for the vortices (such as the downstream wall of the surge chamber model), the jet free shear layer can show large coherent vortex structures. These vortex structures are self-sustained by a feedback loop between i) the pressure fluctuations created by their impingement on the downstream wall, and ii) the amplification of vortices of a given frequency caused by the pressure disturbances fed back to the shear layer sensitive region, close to the inlet of the jet. *Fluid-resonant feedback*, also referred to as indirect feedback, is a mechanism that can occur when a resonator is present in the fluid system. In the current experiments, the resonator role is fulfilled by the free-surface and the resonance frequencies correspond to natural modes of oscillation of the free-surface. When the jet shear layer oscillating frequency approaches one of the natural frequencies of the resonator (upon variation of the flow rate), the indirect feedback mode becomes effective and the free-surface oscillates.

The dominance of either two feedback mechanisms in the flow of Case #4 is illustrated by Figure 5.5(a). In this graph, the frequency of the free-surface oscillations obtained in the experiments and by CFD is plotted for the range of flow rates that was tested. In addition to the frequency of the free-surface oscillations, the frequency of the jet shear layer oscillations was also obtained numerically by probing the velocity during the simulations at a few locations in the jet, and by transforming the velocity time-series obtained therein into the frequency domain. The numerical results did not reveal any free-surface oscillation at the two lower flow rates, 30 and 35 l/s. A dominant frequency in the shear layer was found for these flow rates and fluid-dynamic feedback is believed to be the dominant mechanism. The frequency of the shear layer oscillations increases with the flow rate for these two flow rates, as in Chua *et al.* (1999). The latter found the frequency under a fluid-dynamic feedback mode to be linearly related to the flow rate. A linear, dash-dotted line was then traced in Figure 5.5(a) through the points at 30 and 35 l/s, to visualize what the shear layer frequency would have been without the influence of the resonator. For the next flow rate tested in the simulations, the free-surface starts to slightly oscillate and the frequency of the shear layer oscillations sharply increases to 0.80 Hz, the frequency corresponding to the first natural sloshing mode of the chamber. The free-surface and jet oscillations are "locked in" at the natural sloshing frequency of the chamber, *i.e.* the resonance mode becomes the controlling mechanism for the shear layer oscillations. The jet oscillations remain locked in at approximately 0.80 Hz until 65 l/s with very little change in frequency with increasing in flow rate. Beyond 65 l/s, the jet oscillations become locked again, but at a frequency of 1.18 Hz, corresponding to the second sloshing mode of the chamber. Although no velocity measurements were performed in these experiments, the free-surface oscillations frequencies predicted by the simulations show good agreement with those measured on the test bed.

The above unsteady phenomenon is further illustrated in Figure 5.7, for the numerical simulation run with a flow rate of 45 l/s, for which the free-surface profile was presented in Figure 5.6. Figure 5.7 shows the evolution of the vortices over one period (T = 1.24 s). Instantaneous frames were taken at each quarter of period, *i.e.* at 0T, 0.25T, 0.50T and 0.75T. For each time step, a schematic of the free-surface profile is presented along with the planar velocity magnitudes and streamlines on vertical and horizontal planes passing through the axis of pipe P1. The results are presented in 2D for ease of visualization, but the phenomenon is 3D and vortices are in fact vortex rings. In Figure 5.7, it becomes clear that when a vortex impinges on the downstream wall, a new one is created near the inlet of the jet, which will be advected by the flow toward the downstream wall. It can also be observed that the vortices are shed at a frequency corresponding to the first mode of free-surface sloshing.

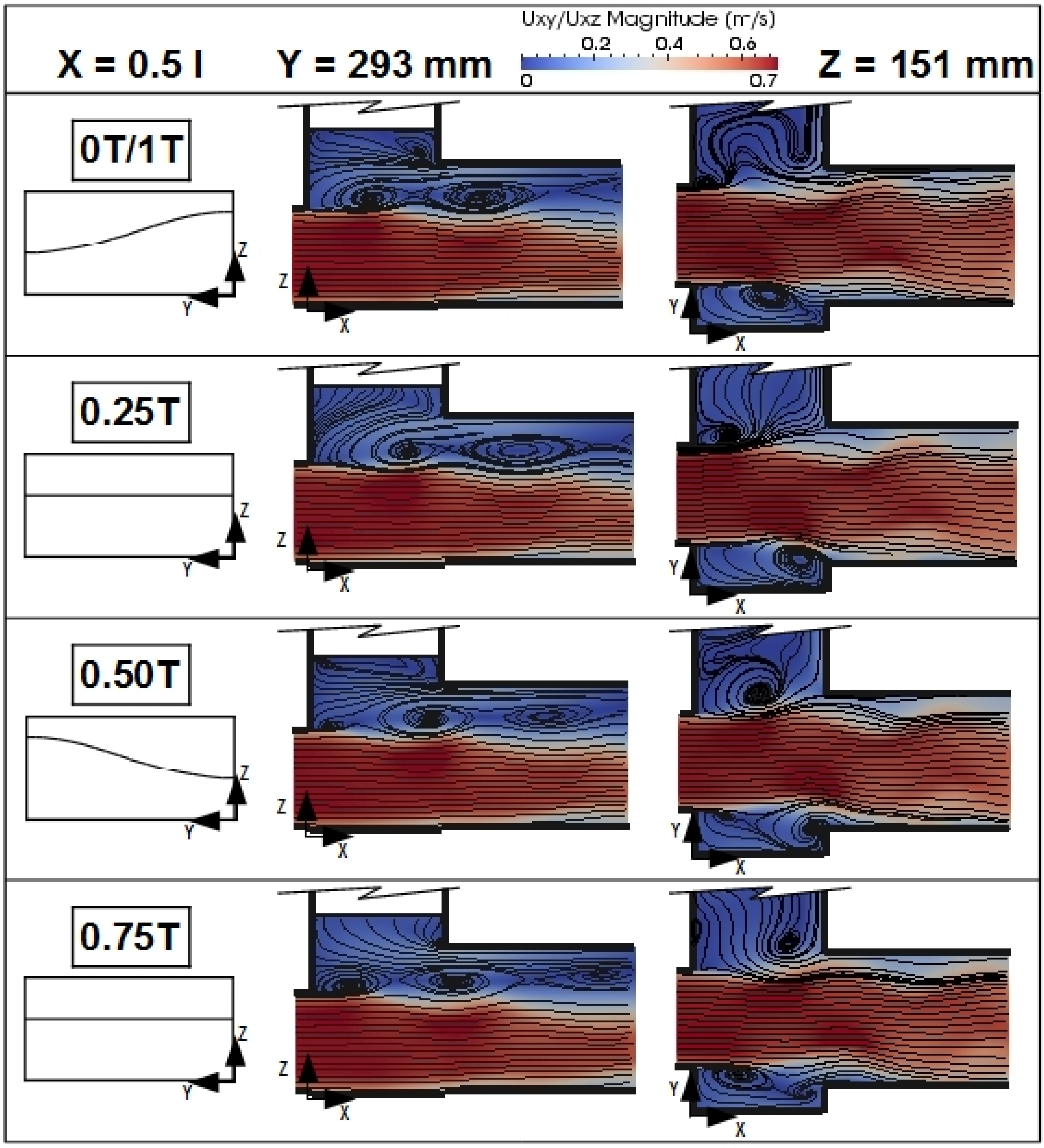

***Figure 5.7**: 2D velocity magnitudes and streamlines on vertical and horizontal planes passing through the axis of pipe P1. Instantaneous results shown at intervals of ¼ of a sloshing period. Results obtained with OpenFOAM for an input flow rate of 45 l/s and a downstream reservoir water height of 550 mm.*

5.5. Flow Characteristic Frequencies

The periodic fluctuations of the instantaneous head losses, observed by Houde *et al.* (2007) in their numerical simulations of the simplified model of a surge chamber, stimulated the investigation of the unsteady behaviour of the surge chamber flow when either P2, or P1 & P2 are under operation. In the current project, all flow quantities in the numerical simulations of these configurations were observed to undergo periodic fluctuations for the surge chamber operated at constant input flow rate. These fluctuations were studied by recording time-series of the free-surface heights at five different locations in both the experiments and the numerical simulations. The time-series signals were then Fourier transformed into the frequency domain in which the dominant frequencies of the signals were determined. Figure 5.8 shows the average energy spectra of the free-surface at five different y locations for the offset pipe P2 under operation at 45 l/s (Case #1). The experimental results are shown in red, while the numerical results of the base case are shown in blue. The two analytical frequencies derived in Chapter 2, corresponding to the oscillating mass phenomenon (0.149 Hz) and to the first sloshing mode of the free-surface (0.800 Hz), are represented by the vertical dotted lines.

In Figure 5.8, the spikes in the energy spectra reveal the existence of dominant frequencies. In the experiments, there are two dominant frequencies that seem to be associated with i) the oscillating mass phenomenon, and ii) the sloshing of the free-surface in its first mode. The measured frequencies agree to within 1% of their analytical predictions. The energy corresponding to the sloshing of the free-surface at the point located at y = 500 mm is very small since the point is located close to the node of the first mode shape. In the energy spectra obtained from the experiments, it is also possible to note that there is some energy associated with all frequencies up to 2.5 Hz (not shown). A large amount of energy is sometimes observed at frequencies close to 0 Hz, due to the long-term fluctuations of the test bed that were not completely removed. Note, however, that these frequencies do not corrupt the present analysis.

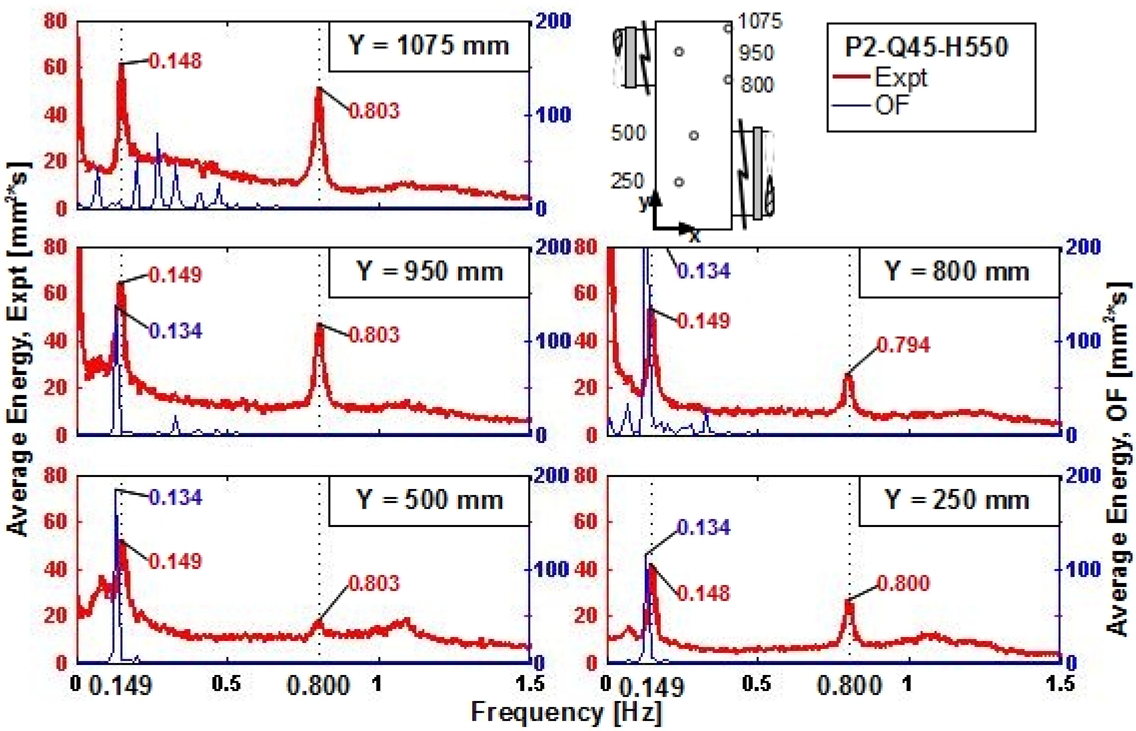

Figure 5.8: *Energy spectra of the free-surface at five different locations for the case of P2 in operation at 45 l/s with a downstream reservoir water level of 550 mm. The experimental Case #1 is shown in red and the numerical base case in blue.*

The spikes in the energy spectra of the numerical base case reveal the existence of only one dominant frequency. This dominant frequency has a value of 0.134 Hz, which is 10% lower than the analytical frequency related to the oscillating mass phenomenon. It is suspected that the observed periodic fluctuations of the simulated flow in the surge chamber are also related to this same phenomenon. As will be seen in a later section, the dominant frequency in the numerical simulations is sensitive to some of the simulation input parameters. To ensure that the oscillations are physical and related to the oscillating mass phenomenon, a numerical simulation could have been run with an output pipe length shortened by one half. For this geometry, the simplified analysis of the surge chamber predicts an increase in frequency by a factor of $\sqrt{2}$. It should be further noted that the numerical spectra only consist of spikes, *i.e.* no energy is associated with a continuous distribution of frequencies as was observed in the experiments. Also, the spectrum for the point located at y = 1075 mm does not suggest any unique dominant frequency, and a particularly high energy is associated with the dominant frequency for the point taken at y = 800 mm, on the free-surface bump.

Similar results were obtained for the spectra of experimental Cases #2 and #3 (not shown). Two dominant frequencies were obtained, and both were close in value to the analytical frequencies of either the oscillating mass phenomenon or the sloshing of the free-surface. The numerical simulation corresponding to Case #3 (not shown) also showed a unique dominant frequency with a value close to that associated with the oscillating mass phenomenon. Based on the knowledge acquired from Case #4 (P1 under operation), it is suspected that there exist (for the cases of P2, or P1 & P2 under operation) structures in the flow having frequencies close to those associated with the oscillating mass phenomenon and with the sloshing of the free-surface, and that the flow is dominated by these two fluid-resonant feedback mechanisms. However, the above remains a hypothesis as the analysis for the cases of P2, or P1 & P2 under operation was not as extensive as that for P1 under operation.

5.6. Head Loss Coefficients

Head loss coefficients (total head loss divided by the input pipe dynamic head) were obtained in the experiments for different permutations of input pipes under operation (P1; P2; P1 & P2), flow rates, and mean water levels of the downstream reservoir. The losses were measured as discussed in Section 2.5. The dynamic pressure heads were computed from the flow rate measurements, and by assuming a uniform velocity profile at the pipes measurement sections. The reduced pressure heads were found from the reduced pressures of the cavities at the measurement sections. Results are presented in Figure 5.9 for P1 (a) and P2 (b) under operation, and in Figure 5.10 for both P1 and P2 under operation simultaneously.

For the case of P1 under operation (Figure 5.9a), the head loss coefficients were obtained for ten different flow rates with the downstream reservoir water level set to 550 mm. A least-square fit of the ten values yielded a head loss coefficient of 0.422, represented by the horizontal dashed line. The maximum discrepancy from the fit is 0.028 (7%) and occurs for a flow rate of 55 l/s. For a flow rate of 45 l/s, the head loss coefficients were also obtained for two different downstream reservoir water levels: 725 and 900 mm. The losses were observed to decrease with an increase of the downstream reservoir water level. The head loss coefficient for the downstream reservoir level of 900 mm differs from the least-square fit by 0.041 (10%). A head loss coefficient was also obtained from a numerical simulation run with an input flow rate of 45 l/s and a water level of 550 mm. The head loss coefficient was also obtained from the flow rate and from the circumferential average pressures at the measurement sections obtained from the time-averaged reduced pressure field. Its difference with the least-square fit is of 0.016 (4%).

A similar analysis was performed for the case of pipe P2 under operation (Figure 5.9b). Seven different flow rates were tested and the least-square fit to the head loss coefficients gave a value of 1.536. The largest difference to this fit occurs for a flow rate of 25 l/s and is of 0.067 (5%). Water levels of 725 and 900 mm were also tested at 45 l/s. No relationship between the water level and the head loss coefficient was observed in this case. An extra test was also performed with a water level of 900 mm and a flow rate of 55 l/s. No significant difference in head loss coefficient was found between this test and that with a lower flow rate of 45 l/s using the same water level (of 900 mm). The head loss

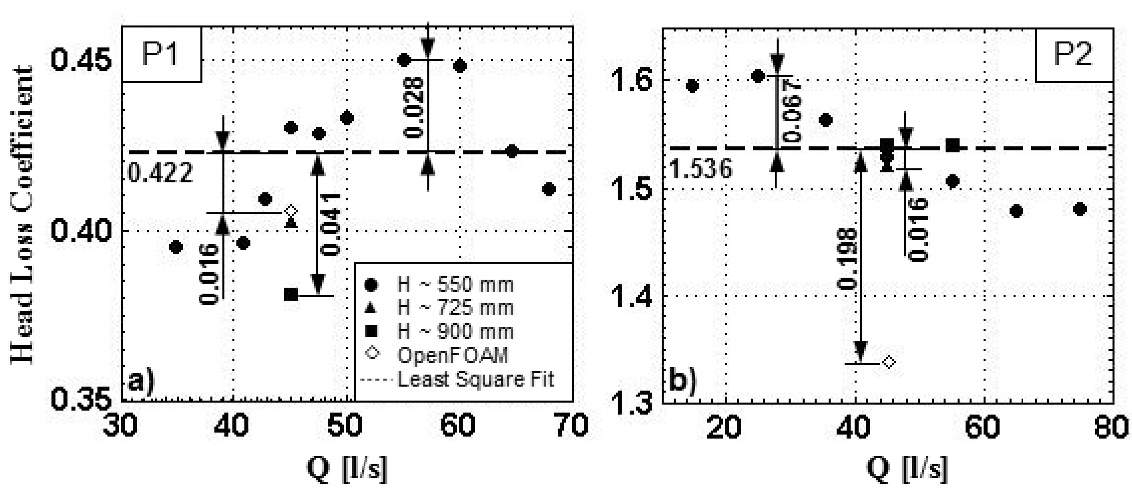

Figure 5.9*: Head loss coefficients for pipes P1 (a), and P2 (b) under operation. The experiments include different flow rates and water levels of the downstream reservoir. The numerical simulations are limited to a flow rate of 45 l/s and a water level of 550 mm.*

coefficient obtained in the base case of the numerical simulations is also shown in Figure 5.9(b). The discrepancy with the least-square fit is of 0.198 (13%).

Furthermore, it can be concluded from Figure 5.9 that the head loss coefficients for a fixed water level of 550 mm exhibit some dependence on the flow rate. Two scenarios are possible. One is that for different flow rates, the topology of the flow in the surge chamber changes in such a way that the head losses are no longer proportional to the square of the flow rate. The other is that the simplifications made in the estimation of the head losses introduce errors which are themselves dependent on the flow rate. While the two scenarios may simultaneously affect the head loss coefficients, the former is suspected to be dominant. As can be seen in Figure 5.9(a) (P1 under operation), the peak in head loss coefficients occurs at a flow rate corresponding to the maximum amplitude of the free-surface oscillations (see Figure 5.5b). This suggests that a larger fraction of the jet kinetic energy is required to sustain the larger oscillations. It can also be observed that higher water levels in the downstream reservoir lead to smaller oscillations of the free-surface, and also to smaller head loss coefficients. From Figure 5.9(b) (P2 under operation), the head loss coefficient peaks at approximately 25 l/s. If the peak of the head loss coefficients is due to resonance, as in the case of P1 under operation, then the resonance frequency is suspected to be lower than that associated to the 1st sloshing mode of the free-surface, because of the lower velocities involved. This reinforces the hypothesis of the existence of a flow structure that oscillates at a frequency associated with the oscillating mass phenomenon.

The head loss coefficients associated with pipes P1 and P2, when both of them are under operation simultaneously, are presented in Figure 5.10. Results are plotted as a function of the ratio of the flow rate in P2 to the total flow rate in P3 (a ratio of 0.5 corresponds to equal flow rates in P1 and P2). Figure 5.10(a) shows the full range of flow rates ratios that were tested in the experiments. The white dots are associated with P1, while the black dots are associated with P2. For each of these experiments, the water level of the downstream reservoir was set to 550 mm, and the flow rate in one of the two input pipes was set to 45 l/s while that in the other pipe was decreased to yield to desired ratio of flow rates. Ratios equal to 0 and 1 correspond, respectively, to only pipe P1 or only pipe P2 in operation. The coefficients obtained by the least-square fits discussed above are substituted at these ratios.

For low ratios of flow rates, the head loss coefficient of P2 is negative, meaning that the energy of the flow from P2 is increased upon mixing with the jet from P1. The head loss coefficient of P2 becomes positive at a flow rates ratio greater than 0.32. The two curves of the head loss coefficients cross each other at flow rates ratios of 0.40 and 0.55, between which the head loss coefficients of P2 are higher than those of P1.

Figure 5.10(b) zooms in on the flow rates ratio around 0.5. At this ratio, different flow rates (48.5, 35, 25 l/s) and water levels (725, 900 mm) were also tested and their results are presented. Note that the data points were artificially offset from the flow rates ratio of 0.5 for better readability. The experimental tests with higher water levels resulted in slightly lower losses in P1 and slightly higher losses for P2. Also, lower head loss coefficients were associated with higher flow rates in both input pipes. The maximum difference between the coefficients of any of these tests and those obtained with an input flow rate of 45 l/s in each pipe and a water level of 550 mm is 0.104 (9%) for pipe P1 and 0.063 (5%) for pipe P2. The head loss coefficients obtained from the numerical

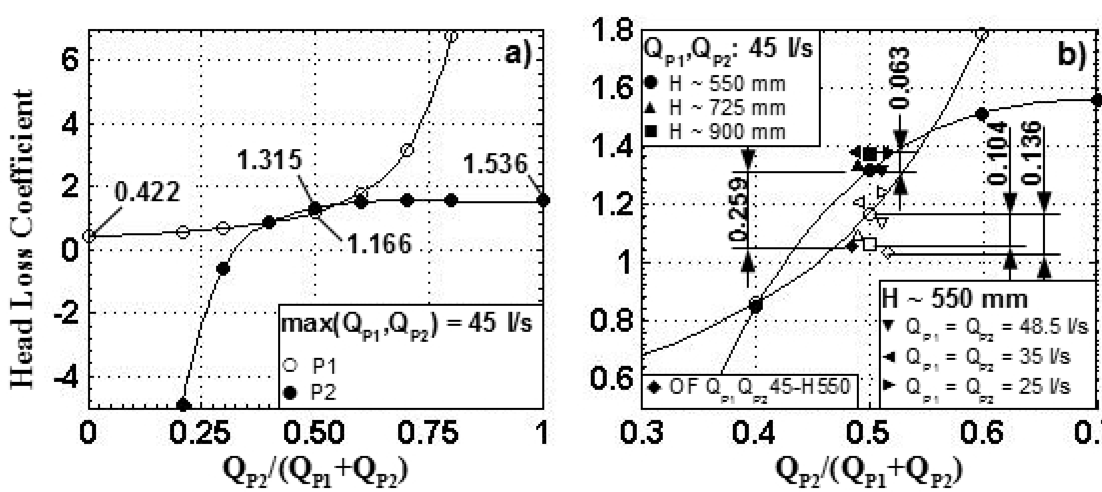

Figure 5.10: *Head loss coefficients in each of the two input pipes when they are under operation simultaneously. The experimental results are presented for many ratios of flow rates, flow rates, and water levels. (b) is the same plot as (a), but with an amplified scale.*

simulation corresponding to the experimental Case #3 are also shown in Figure 5.10(b). They are 0.136 (12%) and 0.259 (20%) lower for P1 and P2, respectively.

The head loss coefficients presented so far were all obtained from the simplified conservation of energy expression, applied to a control volume surrounding the surge chamber (Eqn. 2.10). Unlike the experiments, it was possible to directly evaluate Eqn. 2.10 in the numerical simulations, without any simplification. The differences between the head loss coefficients computed from the rigorous and the simplified forms of the conservation of energy were very small in the simulations — 0.033 (2%) for the base case. This low discrepancy between the two methods was expected since the measurement planes were located in regions of relatively fully-developed flow (as determined from preliminary simulations). However, there is no guarantee that the discrepancies between the two methods will be as low in the experiments.

The level of uniformity of the reduced pressure profiles at the measurement sections was investigated by recording the individual pressures at eight equally-spaced holes around the circumference of each pipe. The tests were done for Cases #1, #3 and #4. While the numerical simulations predict uniform reduced pressure profiles at the measurement sections, the experiments show important variations of reduced pressures around the pipes' circumferences. The measured variations in reduced pressure across the circumference of a given pipe can represent as much as 20% of the head losses of that pipe. The shapes of the circumferential reduced pressure profiles are consistent between different experimental cases for a given pipe, which might suggest that additional factors might need to be taken into account in the numerical simulations.

5.7. Validation of the Parameters Used in the Base Case

The parameters of the simulations that were tested in this study include the refinement of the mesh in the entire computational domain, its refinement in the neighbourhood of the free-surface only, the variation of the maximum Courant number, the levels of the residuals and the β_m coefficient that was used in the Gamma convection scheme. In general, these parameters showed greater influences on the unsteady behaviour of the simulated flow than on the time-averaged quantities that were studied. The most important variations in the results that were observed are shown in Figures 5.11 (free-surface profiles), 5.12 (reduced pressure vertical profile) and 5.13 (dominant period of the flow oscillations with respect to β_m). Note that some data points were slightly offset from β_m = 0.1 in Figure 5.13 for improved readability. Also note that a comparison of the velocity fields obtained in the different numerical simulations is not included in the present analysis.

Refinement of the Mesh in the Entire Computational Domain

Figure 5.11(a) and Figure 5.12 show, respectively, the effect of the mesh refinement in the entire computational domain on i) the free-surface profile at y = 250 mm, and ii) the vertical reduced pressure profile at the downstream wall of the surge chamber. In these figures, important differences can be observed between the results obtained on the coarser grid and those obtained on the two other grids. The results seem to have converged on the medium-size grid ($1.73*10^6$ cells), since no significant difference is obtained by increasing the grid size to $4.20*10^6$ cells. The average head losses computed on the three grids were equivalent, but the dominant frequency of the simulated flow was greatly influenced by the size of the mesh. As shown in Figure 5.13, by varying the size of the mesh from $0.97*10^6$ to $1.73*10^6$ and $4.20*10^6$ cells, the dominant period of the oscillations varied from 5.1 to 7.5 and 7.7 s, respectively.

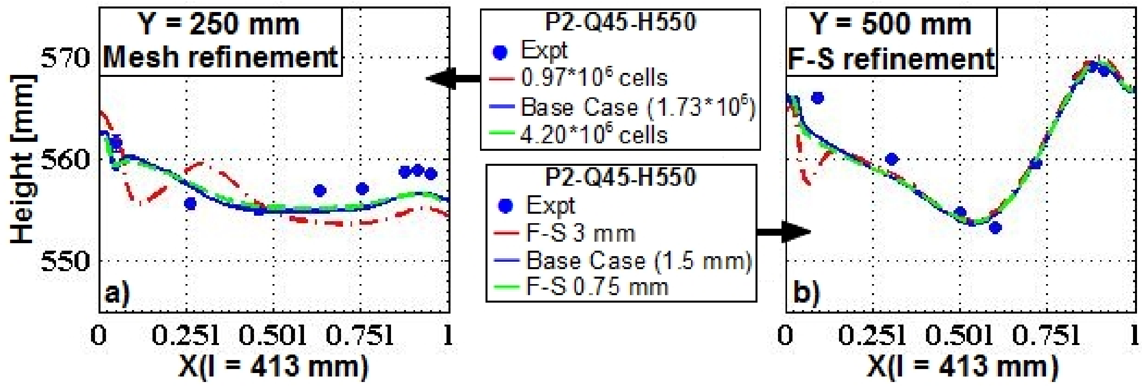

Figure 5.11: *Effect of the mesh refinement in the entire computational domain (a) or in the neighbourhood of the free-surface only (b) on the free-surface profiles located at y = 250 and y = 500 mm, respectively.*

Refinement of the Mesh in the Neighbourhood of the Free-Surface

The height of the cells in the neighbourhood of the free-surface did not influence significantly either of the reduced pressure profiles, the global losses in the surge chamber and the dominant period of the flow oscillations (Figure 5.13). The most significant variations in the results were found in the free-surface profiles at y = 250 and 500 mm, the latter of which is shown in Figure 5.11(b). While variations are important for the coarser cells' height (3 mm), no major difference is noted between the other two cells' heights of 1.5 (base case) and 0.75 mm.

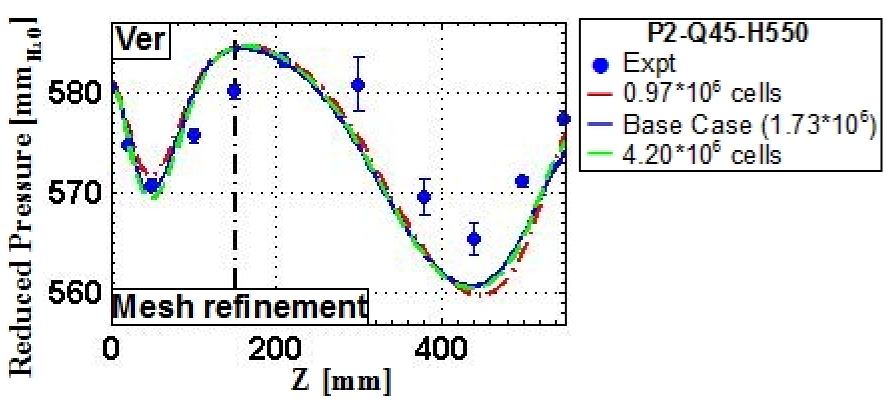

Figure 5.12: *Effect of the mesh refinement in the entire computational domain on the vertical reduced pressure profile at the downstream wall of the chamber.*

Courant Number, Levels of Residuals and βm Coefficient

Neither of the tested maximum Courant numbers (0.8 and 0.2), levels of residuals (those of the base case described in Section 4.6, and the latter reduced by a factor of 10^2) and β_m coefficients (0.1, 0.3, 0.5) influenced significantly the time-averaged free-surface profiles, reduced pressure profiles and global losses. While the levels of residuals that were tested did not affect the period of oscillations of the simulated flow, important variations were observed by changing the values of the maximum Courant number and the β_m coefficient. In Figure 5.13, reducing the maximum Courant number by a factor of 4 results in a decrease of the dominant period of flow oscillations from 7.5 to 7.3 s, approaching the analytical value corresponding to the oscillating mass phenomenon (6.7 s). Larger variations of the simulated period of flow oscillations were observed by modifying the β_m coefficient used in the Gamma convection scheme for the discretization of the momentum equations. Coefficients of 0.1, 0.3 and 0.5 resulted in periods of 7.5, 6.9 and 5.8, respectively.

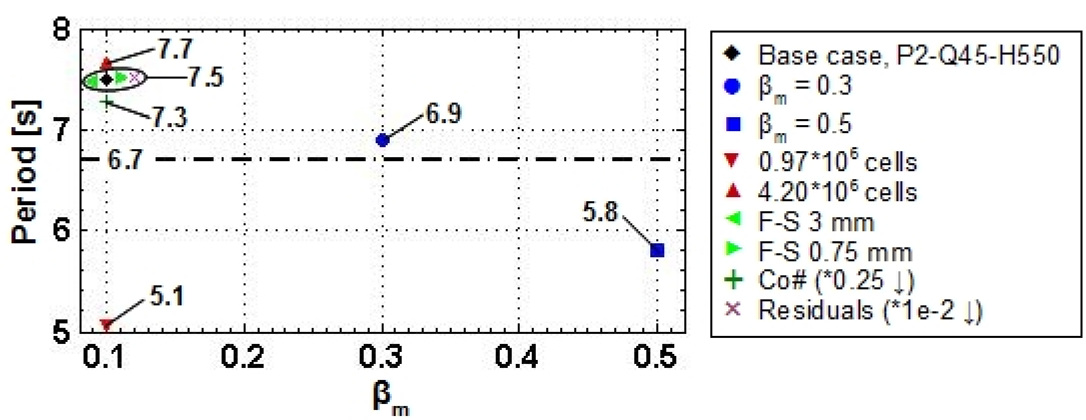

Figure 5.13*: Variation of the dominant period of oscillation of the flow with respect to the β_m coefficent, for the base case and the eight other numerical tests run with P2 in operation at 45 l/s and with a downstream reservoir water level of 550 mm. For the base case, β_m = 0.1; Mesh size = 1.73*10^6 cells; F-S = 1.5 mm; Co# = 0.8; Residuals = 10^{-7} (reduced pressure), 10^{-6} (velocity components), and 10^{-8} (k and ε).*

Based on the above analysis, the parameters used in the base case (P2 in operation) numerical simulation are believed to yield sufficiently converged time-averaged quantities. The same cannot be said for the periodic fluctuations. The numerical simulations of P1, or P1 & P2 in operation were not as extensively tested as those of P2 in operation. However, the knowledge gained in this analysis was used to make informed selections for their parameters.

6. Conclusions and Recommendations

This research has been performed with the intent of i) better understanding the flow in the simplified model of a hydraulic turbine surge chamber, and ii) validating the rasInterFoam solver within OpenFOAM-1.5 used in simulating such a flow. The principal structures of the flow inside the surge chamber simplified model, along with its periodic oscillations, were identified and characterized with the aid of experimental measurements and numerical simulations. Keeping in mind that both methods have their own limitations and neither of them provide perfect answers, the ability of the rasInterFoam solver to accurately simulate such a flow was assessed by comparisons of key measured and predicted quantities. Because of the complexity of the flow, it is hoped that this work will not only serve in the simulations of actual hydraulic turbine surge chambers, but will also provide an extra test case for OpenFOAM, contributing to its acceptance by the CFD community.

This last chapter concludes the thesis by summarizing the main findings of this work (Section 6.1) and suggestions for future work (Section 6.2).

6.1. Conclusions

The results in this thesis have been extensively discussed and analyzed. In what follows, the most important conclusions are summarized.

- The major structures of the flow were identified and characterized. Comparisons between the ADV measurements at 14 points inside the chamber for the experimental Case #1 and the time-averaged velocity field of the corresponding numerical simulation showed that the topology of the flow is globally well-simulated by the code.
- The jet from pipe P2 is less deflected toward the output pipe and the free-surface in the numerical simulations than in the experiments. This results in simulated

reduced pressure profiles at the downstream wall peaking closer to the axis of P2 than in the corresponding experiments.

- The time-averaged perturbations of the free-surface are mostly due to the jet from pipe P2, as the operation of P1 does not significantly change the shapes of the profiles.
- The free-surface profiles obtained on five vertical planes in the experiments are well-reproduced by the numerical simulations.
- The simulated free-surface, in the region of the chamber defined by the intersection of the upstream wall and the side wall closest to the output pipe, is less well-defined than elsewhere. There, the interval of volume fraction between 0.1 and 0.9 is diffused vertically over many cells. Entrainment of air into the flow was observed in the experiments to occur in this region, because the free-surface was folding on itself. The diffusion of the simulated free-surface is therefore more likely to be related to the physical nature of the flow itself than to unwanted numerical diffusion of the volume fraction field.
- In the case of only P1 under operation, sloshing of the free-surface in its first mode was observed and characterized for a range of flow rates in both the experiments and the numerical simulations. At low flow rates, only the shear layer oscillates and the flow undergoes a fluid-dynamic feedback mechanism. When the frequency of the shear layer becomes close enough to that corresponding to the first sloshing mode of the free-surface upon an increase in flow rate, fluid-resonant feedback becomes the dominant mode, and the shear layer oscillations are locked at the sloshing frequency of the free-surface. The free-surface oscillates for a range of flow rates until further increase in flow rates can no longer sustain the sloshing. The simulated sloshing frequencies of the free-surface agree with those measured in the experiments. However, the predicted oscillations of the free-surface start, peak and finish at lower flow rates than what was

observed in the experiments. Furthermore, the peak in amplitude of the oscillations is around 34% lower in the simulations than in the experiments.

- In the cases of P2, or P1 & P2 under operation, the experiments reveal the existence of two dominant frequencies of oscillations in the flow. The values of those two dominant frequencies agree to within 1% of the analytical values associated with the oscillating mass phenomenon and the 1st sloshing mode of the free-surface. In the numerical simulations, only one dominant frequency is observed, for which the value is within 10% of the frequency associated with the oscillating mass phenomenon. Based on the knowledge acquired in the analysis of the case of P1 under operation, it is suspected that a resonant mechanism occurs for P2, or P1 & P2 under operation, due to some structures of the flow oscillating at frequencies close to those of the oscillating mass phenomenon and the 1st sloshing mode of the free-surface.

- The head loss coefficients obtained in the experiments with pipe P1 under operation were observed to peak between flow rates of 55 and 60 l/s, similar to the amplitude of the oscillations of the free-surface. This suggests that a larger proportion of the jet kinetic energy is required to sustain larger amplitude oscillations. It was also observed that higher water levels in the downstream reservoir lead to smaller oscillations of the free-surface, and to smaller head loss coefficients.

- The head loss coefficients obtained in the experiments with pipe P2 under operation were also observed to vary with the flow rate, peaking around 25 l/s. If the peak of the head loss coefficients is due to a resonant mechanism, as in the case of P1 under operation, then the resonance frequency is suspected to be lower than that associated with the 1st sloshing mode of the free-surface, because of the lower velocities involved. This reinforces the hypothesis of the existence of a flow structure oscillating close to the frequency associated with the oscillating mass phenomenon.

- The head loss coefficients were also obtained for the case of both P1 and P2 under simultaneous operation, for different flow rates ratios. For a low ratio of flow rates in P2, the head loss coefficient in the latter is negative, meaning that the flow gains energy by mixing with the jet from P1 in the output pipe. Furthermore, the head loss coefficients are lower in P2 than in P1 for any flow rates ratios, except between values of 0.40 and 0.55.

- The head loss coefficients predicted by the numerical simulations for the cases of P1, and P2 individually under operation are 4% and 13% lower than the least-square fits to the experimental results, respectively. In the case of P1 and P2 simultaneously under operation, the predicted head loss coefficients at a flow rates ratio of 0.5 are 12% and 20% lower than those measured in the experiments in pipes P1 and P2, respectively.

- The head loss coefficients computed from the rigorous and simplified forms of the conservation of energy equation applied to a control volume surrounding the surge chamber did not yield significant differences in the numerical simulations. However, this cannot be guaranteed to be the case in the experiments. For example, the reduced pressure was uniform at the measurement sections in the numerical simulations, while significant variations were recorded along the circumferences of the pipes in the experiments.

- Convergence of the time-averaged quantities was observed for a mesh containing $1.73*10^6$ cells, and having a uniform cells height of 1.5 mm in the neighbourhood of the free-surface (base case).

- The simulated dominant period of oscillations of the flow was principally affected by the size of the mesh and the value of the β_m coefficient of the Gamma convection scheme used to discretize the divergence terms in the momentum equations.

6.2. Suggestions for Future Work

The combination of both experimental and numerical methods has proven to be a good strategy to follow in the study of the complex flow in the simplified model of a hydraulic turbine surge chamber. Although much more remains to be achieved in the experiments, the author believes that the project has matured to a stage where more numerical tests are required. The suggestions herein therefore relate to possible studies that could be undertaken in future numerical simulations.

- Although the simulated head loss coefficients do not agree perfectly with the experiments, a deeper understanding could be obtained by running more simulations with different flow rates and water levels to determine if the same tendencies observed in the experiments are predicted by rasInterFoam.
- To validate the hypothesis that the dominant period of oscillations computed in the simulations is related to the oscillating mass phenomenon (and not to some numerical instabilities), a simulation could be run with half the actual length of output pipe. If the dominant period of oscillations changes according to Eqn. 2.4, then the oscillations are most probably related to the latter effect.
- Addressing the discrepancies between the experiments and the numerical simulations with respect to i) the degree of jet deflection and ii) the level of uniformity of the reduced pressures along the circumferences of the pipes at the measurement sections might contribute to more realistic simulations.
- Other parameters of the rasInterFoam solver should be tested, as important variations in the dominant period of the flow oscillations were observed.
- Highly swirling flows are generally poorly predicted by the k-ε turbulence model due to the complex strain field. Gains in accuracy might result from using another turbulence model such a Reynolds Stress model.
- Finally, another numerical method for solving two-phase flows could be tested.

Appendix A: Input Dictionaries of the Base Case of the Numerical Simulations

constant\environmentalProperties	
g	g [0 1 -2 0 0 0 0] (0 0 -9.81);

constant\RASProperties	
RASModel	kEpsilon;
turbulence	on;
kEpsilonCoeffs	
{	
Cmu	0.09;
C1	1.44;
C2	1.92;
alphaEps	0.76923;
}	
wallFunctionCoeffs	
{	
kappa	0.4187;
E	9;
}	

constant\transportProperties	
twoPhase	
{	
transportModel	twoPhase;
phase1	phase1;
phase2	phase2;
}	
phase1	
{	
transportModel	Newtonian;
nu	nu [0 2 -1 0 0 0 0] 1.12e-06;
rho	rho [1 -3 0 0 0 0 0] 999;
}	

```
phase2
{
   transportModel        Newtonian;
   nu                    nu [0 2 -1 0 0 0 0] 1.46e-05;
   rho                   rho [1 -3 0 0 0 0 0] 1.23;
}
sigma                    sigma [1 0 -2 0 0 0 0] 0.0734;
```

system\controlDict

```
application              rasInterFoam;
startFrom                startTime;
startTime                0;
stopAt                   endTime;
endTime                  200;
deltaT                   0.001;
writeControl             adjustableRunTime;
writeInterval            1;
purgeWrite               0;
writeFormat              ascii;
writePrecision           8;
writeCompression         compressed;
timeFormat               general;
timePrecision            8;
runTimeModifiable        yes;
adjustTimeStep           on;
maxCo                    0.8;
maxDeltaT                1;
```

system\fvSchemes

```
ddtSchemes
{
   default               Euler;
}
gradSchemes
{
   default               Gauss linear;
}
```

```
divSchemes
{
   div(rho*phi,U)          Gauss GammaV 0.2;
   div(phi,gamma)          Gauss vanLeer;
   div(phirb,gamma)        Gauss interfaceCompression;
   div(phi,k)              Gauss upwind;
   div(phi,epsilon)        Gauss upwind;
}
laplacianSchemes
{
   default                 Gauss linear corrected;
}
interpolationSchemes
{
   default                 linear;
   interpolate(HbyA)       linear;
}
snGradSchemes
{
   default                 corrected;
}
fluxRequired
{
   default                 no;
   pd;
   pcorr;
   gamma;
}
```

system\fvSolution

```
solvers
{
   pd PCG
   {
      preconditioner       DIC;
      tolerance            1e-7;
      relTol               0.05;
   };
```

```
    pdFinal PCG
    {
        preconditioner      DIC;
        tolerance           1e-7;
        relTol              0;
    };
    U PBiCG
    {
        preconditioner      DILU;
        tolerance           1e-06;
        relTol              0;
    };
    k PBiCG
    {
        preconditioner      DILU;
        tolerance           1e-08;
        relTol              0;
    };
    epsilon PBiCG
    {
        preconditioner      DILU;
        tolerance           1e-08;
        relTol              0;
    };
}
PISO
{
    momentumPredictor   no;
    nCorrectors         3;
    nNonOrthogonalCorrectors    0;
    nGammaCorr          1;
    nGammaSubCycles     4;
    cGamma              1;
}
```

References

Berberovic E, Hinsberg NP, Jakirlic S, Roisman IV, Tropea C. 2009 Drop Impact Onto a Liquid Layer of Finite Thickness: Dynamics of the Cavity Evolution. *Physical Review E*. **79(3)**, 1-15.

Bohorquez P. 2008 Study and Numerical Simulation of Sediment Transport in Free-Surface Flow. PhD Thesis, University of Malaga.

Bonnefous O, Pesqué P. 1986 Time Domain Formulation of Pulse-Doppler Ultrasound and Blood Velocity Estimation by Cross Correlation. *Ultrasonic Imaging*. **8**, 73-85.

Brackbill JU, Kothe DB, Zemach C. 1992 A Continuum Method for Modelling Surface Tension. *Journal of Computational Physics*. **100**, 335-354.

Brumley BH, Cabrera RG, Deines KL, Terray EA. 1991 Performance of a Broad-Band Acoustic Doppler Current. *IEEE Journal of Oceanic Engineering*. **16(4)**, 402-407.

Cabrera R, Deines K, Brumley B, Terray E. 1987 Development of a Practical Coherent Acoustic Doppler Current Profiler. *Proc. Oceans*. **19**, 93-97.

Cea L, Puertas J, Pena L. 2007 Velocity Measurements on Highly Turbulent Free Surface Flow Using ADV. *Experiments in Fluids*. **42(3)**, 333-348.

Chanson H. 2008 Acoustic Doppler Velocimetry (ADV) in the Field and in Laboratory: Practical Experiences. In *International Meeting on Measurements and Hydraulics of Sewers*, pp. 49-66.

Chua HC, Shuy EB. 1999 Fluid-Dynamic Feed-Back in Shear Layer Oscillation below a Submerged Sluice Gate. *Journal of Hydraulic Research*. **37(1)**, 107-120.

Chua HC, Shuy EB. 2006a Coupling of U-Tube and Shear Layer Oscillations in an Interconnected Flow Compartment. *Journal of Engineering Mechanics*. **132(7)**, 764-770.

Chua HC, Shuy EB. 2006b Mixing Layer Oscillations for a Submerged Horizontal Wall-Jet. *Journal of Hydraulic Research*. **44(1)**, 115-123.

Chua HC, Shuy EB. 2008 Laboratory Studies on the Coupled Oscillations between an Internal Density Interface and a Shear Layer. *Journal of Engineering Mechanics*. **134(4)**, 348-352.

Crowe CT et al.. 2006 *Multiphase Flow Handbook*. CRC Press Taylor & Francis Group, NW.

Darwish M, Moukalled F. 2006 Convective Schemes for Capturing Interfaces of Free-Surface Flows on Unstructured Grids. *Numerical Heat Tranfer*. **49**, 19–42.

Drew DA, Passman SL. 1998 *Theory of Multicomponent Fluids*. Springer-Verlag, New York.

Faltinsen OM, Timokha AN. 2009 *Sloshing*. Cambridge University Press, New York.

Gaskell PH, Lau AKC. 1988 Curvature-Compensated Convective Transport: SMART, a New Boundedness-Preserving Transport Algorithm. *International Journal for Numerical Methods in Fluids*. **8**, 617-641.

Gopala VR, van Wachem BGM. 2008 Volume of Fluid Methods for Immiscible-Fluid and Free-Surface Flows. *Chemical Engineering Journal*. **141**, 204-221.

Goring DG, Nikora VI. 2002 Despiking Acoustic Doppler Velocimeter Data. *Journal of Hydraulic Engineering*. **128(1)**, 117-126.

Harlow FH, Welch JE. 1965 Numerical Calculation of Time-Dependent Viscous Incompressible Flow of Fluid with Free Surface. *Physics of Fluids*. **8(12)**, 2182-2189.

Henderson FM. 1966 *Open Channel Flow*. Macmillan, New York.

Hirt CW, Nichols BD. 1981 Volume of Fluid (VOF) Method for the Dynamics of Free Boundaries. *Journal of Computational Physics*. **39**, 201-225.

Houde S. 2007 *Simulation de l'Écoulement dans une Chambre d'Équilibre Modèle et Comparaisons avec des Mesures Expérimentales*. Rapport IREQ-2007-0118 (diffusion Hydro-Québec), Varennes (Québec).

Houde S, Page M, Mainville E. 2007 Numerical Investigation of the Dynamic Behavior of Surge Chamber Under Normal Operating Conditions. In *2nd IAHR International Meeting of the WorkGroup on Cavitation and Dynamic Problems in Hydraulic Machinery and Systems*, pp. 1-15.

Ibrahim RA. 2005 *Liquid Sloshing Dynamics*. Cambridge University Press, New York.

Ishii M, Hibiki T. 2006 *Thermo-Fluid Dynamics of Two-Phase Flow*. Springer, New York.

Issa RI. 1985 Solution of the Implicit Discretised Fluid Flow Equations by Operator-Splitting. *Journal of Computational Physics*. **62**, 40-65.

Jasak H. 1996 Error Analysis and Estimation for the Finite Volume Method with Applications to Fluid Flows. PhD Thesis, University of London.

Jasak H, Weller HG, Gosman AD . 1999 High Resolution NVD Differencing Scheme for Arbitrarily Unstructured Meshes . *International Journal for Numerical Methods in Fluids*. **31**, 431-449.

Karandeev KB, Grinevich FB, Novik AI. 1961 Construction of Capacitive Level Gauges. *Measurement Techniques*. **4(10)**, 52-55.

Kraus NC, Lohrmann A, Cabrera R. 1994 New Acoustic Meter for Measuring 3D Laboratory Flows. *Journal of Hydraulic Engineering*. **120(3)**, 406-412.

Lane SN, Biron PM, Bradbrook KF, Butler JB, Chandler JH, Crowell MD, McLelland SJ, Richards KS, Roy AG. 1998 Three-Dimensional Measurement of River Channel Flow Processes Using Acoustic Doppler Velocimetry. *Earth Surface Processes and Landforms*. **23**, 1247-1267.

Leonard BP. 1991 The ULTIMATE Conservative Difference Scheme Applied to Unsteady One-Dimensional Advection. *Computer Methods in Applied Mechanics and Engineering*. **88**, 17-74.

Lhermitte R, Lemmin U. 1994 Open-Channel Flow and Turbulence Measurement by High-Resolution Doppler Sonar. *Journal of Atmospheric and Oceanic Technology*. **11**, 1295-1308.

Lohrmann A, Cabrera R, Gelfenbaum G, Haines J. 1995 Direct Measurements of Reynolds Stress with an Acoustic Doppler Velocimeter. In *Proceedings of the IEEE Fifth Working Conference on Current Measurement*, pp. 205-210.

Lohrmann A, Cabrera R, Kraus NC. 1994 Acoustic Doppler Velocimeter (ADV) for Laboratory Use. In *Proceedings Symp. on Fundamentals and Advancements in Hydraulic Measurements and Experimentation*, pp. 351-365.

McLelland SJ, Nicholas AP. 2000 A New Method for Evaluating Errors in High-Frequency ADV Measurements. *Hydrological Processes*. **14**, 351-366.

Mori N, Suzuki T, Kakuno S. 2007 Noise of Acoustic Doppler Velocimeter Data in Bubbly Flows. *Journal of Engineering Mechanics*. **133(1)**, 122-125.

Nikora VI, Goring DG. 2000 Flow Turbulence over Fixed and Weakly Mobile Gravel Beds. *Journal of Hydraulic Engineering*. **126(9)**, 679-690.

Noh WF, WoodWard P. 1976 SLIC (Simple Line Interface Calculation). *Lecture Notes in Physics*. **59**, 330–340.

Okamoto K, Madarame H. 1991 Self-Induced Oscillation of Free Surface in a Tank with Circulating Flow. *Proceeding 5th International Conference on Flow Induced Vibrations*. **6**, 539-545.

OpenCFD Ltd. 2010 OpenFOAM, The Open Source CFD Toolbox, User Guide.

Osher S, Sethian JA. 1988 Fronts Propagating with Curvature-Dependent Speed: Algorithms Based on Hamilton-Jacobi Formulations. *Journal of Computational Physics*. **79**, 12-49.

Press WH, Teukolsky SA, Vetterling WT, Flannery BP. 2002 *Numerical Recipes in C++: The Art of Scientific Computing*. Cambridge University Press, New York.

Prosperetti A, Tryggvason G et al.. 2007 *Computational Methods for Multiphase Flow*. Cambridge University Press, New York.

Reverter F, Li X, Meijer GCM. 2007 Liquid-Level Measurement System Based on a Remote Grounded Capacitive Sensor. *Sensors and Actuators A: Physical*. **138**, 1-8.

Ross PJ. 1983 A Water-Level Sensor Using a Capacitance to Frequency Converter. *Journal of Physics E: Scientific Instruments*. **16**, 827-828.

Rusche H. 2002 Computational Fluid Dynamics of Dispersed Two-Phase Flows at High Phase Fractions. PhD Thesis, University of London.

Saeki S, Madarame H, Okamoto K. 2001 Self-Induced Sloshing Excited by a Horizontally Injected Plane Jet. *Journal of Fluid Mechanics*. **448**, 81-114.

Ubbink O. 1997 Numerical Prediction of Two Fluid Systems with Sharp Interfaces. PhD Thesis, University of London.

Ubbink O, Issa RI. 1999 A Method for Capturing Sharp Fluid Interfaces on Arbitrary Meshes. *Journal of Computational Physics*. **153**, 26-50.

Unverdi SO, Tryggvason G. 1992 A Front-Tracking Method for Viscous, Incompressible Multi-Fluid Flows. *Journal of Computational Physics*. **100**, 25-37.

Voulgaris G, Trowbridge JH. 1998 Evaluation of the Acoustic Doppler Velocimeter (ADV) for Turbulence Measurements. *Journal of Atmospheric and Oceanic Technology*. **15(1)**, 272-289.

Vournas CD, Papaioannou G. 1995 Modeling and Stability of a Hydro Plant with Two Surge Tanks. *IEEE Transactions on Energy Conversion*. **10(2)**, 368-375.

Wahl TL. 2003 Discussion of "Despiking Acoustic Doppler Velocimeter Data". *Journal of Hydraulic Engineering*. **129(6)**, 484-488.

Weller HG, Tabor G, Jasak H, Fureby C. 1998 A Tensorial Approach to Computational Continuum Mechanics Using Object-Oriented Techniques. *Computers in Physics*. **12(6)**, 620-631.

Wheeler AJ, Ganji AR. 2004 *Introduction to Engineering Experimentation, second edition*. PEARSON Prentice Hall, New Jersey.

Wong GSK, Zhu S. 1995 Speed of Sound in Seawater as a Function of Salinity, Temperature and Pressure. *J. Acoust. Soc. Am.*. **97(3)**, 1732-1736.

Zedel L. 2008 Modeling Pulse-to-Pulse Coherent Doppler Sonar. *Journal of Atmospheric and Oceanic Technology*. **25**, 1834-1844.

Zedel L, Hay AE, Cabrera R, Lohrmann A. 1996 Performance of a Single-Beam Pulse-to-Pulse Coherent Doppler Profiler. *IEEE Journal of Oceanic Engineering*. **21(3)**, 290-297.